Graphene Chemical and Biological Sensors: Modeling, Systems, and Applications

by

Charles Mackin

B.S., University of Arizona (2012)
S.M., Massachusetts Institute of Technology (2015)

Submitted to the Department of Electrical Engineering and Computer Science

in partial fulfillment of the requirements for the degree of

DOCTOR OF PHILOSOPHY

at the

MASSACHUSETTS INSTITUTE OF TECHNOLOGY

June 2018

Signature of Author: Signature redacted

Department of Electrical Engineering & Computer Science
May 23, 2018

Certified by: Signature redacted

Tomás Palacios
Professor of Electrical Engineering and Computer Science
Thesis Supervisor

Accepted by: Signature redacted

Leslie A. Kolodziejski
Professor of Electrical Engineering and Computer Science
Chair, Departmental Committee on Graduate Students

Graphene Chemical and Biological Sensors: Modeling, Systems, and Applications

by

Charles Mackin

Submitted to the Department of Electrical Engineering & Computer Science
on May 23, 2018, in Partial Fulfillment of the
requirements for the Degree of
Doctor of Philosophy

Abstract

Graphene exhibits a unique combination of properties making it particularly promising for sensing applications. This thesis builds new graphene chemical and biological sensing technologies from the ground up by developing device models, systems, and applications. On the modeling side, this thesis develops a DC model for graphene electrolyte-gated field-effect transistors (EGFETs). It also presents a novel frequency-dependent (AC) small-signal model for graphene EGFETs and demonstrates the ability of these devices to operate as functional amplifiers for the first time.

Graphene sensors are transitioned to the system level by developing a new sensor array architecture in conjunction with a compact and easy-to-use custom data acquisition system. The system allows for simultaneous characterization of hundreds of sensors and provides insight into graphene EGFET performance variations. The system is adapted to develop solution-phase ionized calcium sensors using a graphene EGFET array that has been functionalized using a polyvinyl chloride (PVC) membrane containing a neutral calcium ionophore. Sensors are shown to accurately quantify ionized calcium over several orders of magnitude while exhibiting excellent selectivity, reversibility, response time, and a virtually ideal Nernstian response of 30.1 mV/decade. A new variation-insensitive distribution matching technique is also developed to enable faster readout.

Finally, the sensor system is employed to develop gas-phase chemiresistive ammonia sensors that have been functionalized using cobalt porphyrin. Sensors provide enhanced sensitivity over pristine graphene while providing selectivity over interfering compounds such as water and common organic solvents. Sensor responses exhibit high correlation coefficients indicating consistent sensor response and reproducibility of the cobalt porphyrin functionalization. Variations in sensitivity follow a Gaussian distribution and are shown to stem from variations in the underlying sensor source-drain currents. A detailed kinetic model is developed describing sensor response profiles that incorporates two ammonia adsorption mechanisms—one reversible and one irreversible.

Thesis Supervisor: Tomás Palacios
Title: Professor

Graphene Chemical and Biological Sensors: Modeling, Systems, and Applications

List of Figures

Chapter 1: Introduction

1.1 Graphene Introduction

Graphene consists of an atomically-thin planar sheet of sp^2-hybridized carbon atoms arranged in a hexagonal lattice [1]–[5]. It represents the two-dimensional building block for graphite and possesses strong in-plane carbon bonds and weak van der Waals forces between layers. Graphene has been studied theoretically since the 1940s, but was presumed unstable and not to exist in its free-standing form [6], [7]. It was isolated and studied experimentally for the first time in 2004 [8]. Graphene is the last member to be isolated in the family of low-dimensional carbon allotropes depicted in **Figure 1.1.** The other two forms are zero-dimensional buckminsterfullerene and one-dimensional carbon nanotubes.

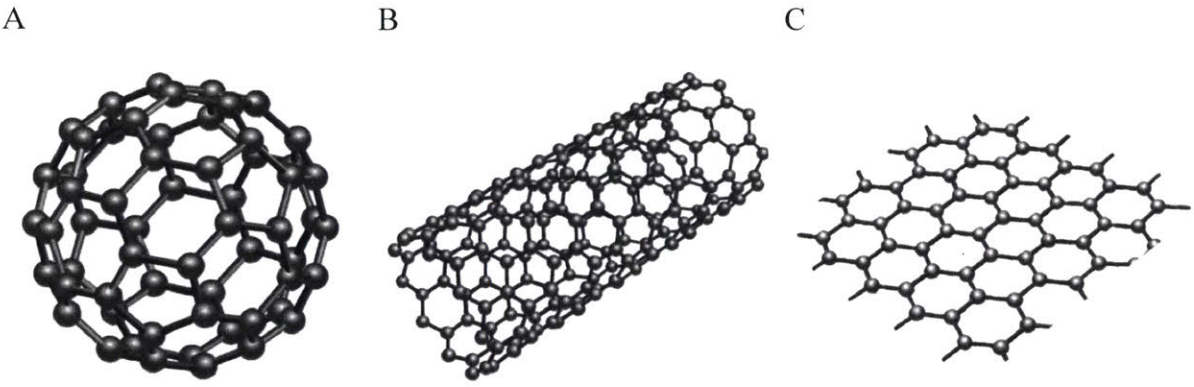

Figure 1.1: Low-dimensional carbon allotropes A) spherical Buckminster fullerene B) 1D carbon nanotube C) 2D graphene [9].

Graphene has an atomic density of 3.82×10^{15} atoms/cm^{-2} with a carbon-carbon bond length of 1.42 Å [10], [11]. Each carbon atom in graphene possesses four valence electrons. Three electrons undergo sp^2 hybridization to form in-plane covalent bonds

with the three nearest neighbors. These are termed sigma bonds (σ-bond). The remaining valence electron is oriented perpendicular to the plane in a p_z orbital and forms a pi-bond (π-bond). Electrons in the π-bonds are delocalized enabling charge transport in graphene. **Figure 1.2** illustrates sp^2 hybridization and the formation of σ-bonds and π-bonds in graphene.

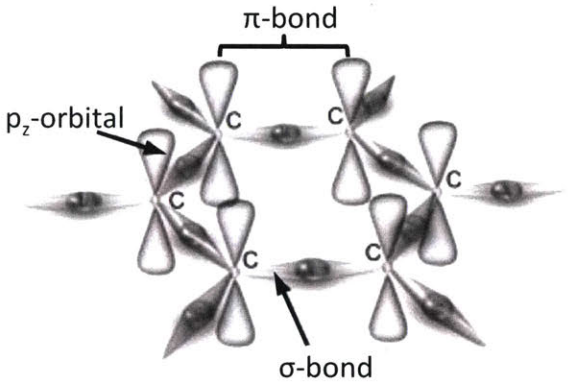

Figure 1.2: Graphene sp^2 hybridization, σ-bonds, and π-bonds [12].

The low-energy band structure of graphene is unique in that the conduction band and valence band meet at a single point, called the Dirac point. For this reason, graphene is termed a semimetal or a zero bandgap semiconductor. The linear dispersion of graphene's cone-shaped band structure is reminiscent of photons and gives rise to massless relativistic particles called Dirac fermions [13]–[16]. This allows carriers in graphene to move at an effective speed of light called the Fermi velocity, v_F, which is defined by the slope of the energy-momentum dispersion [17]–[19]. The Fermi velocity

in graphene is $c/300$, where c is the speed of light. The band structure for graphene is depicted in **Figure 1.3.**

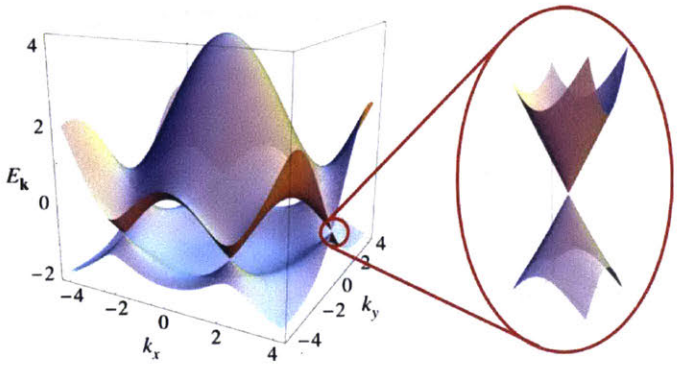

Figure 1.3: Graphene band structure as reproduced from [3].

Graphene's band structure in combination with its density of states gives rise to its unique ambipolar transport properties and V-shaped *I-V* characteristic. Depending on the location of the Fermi level, graphene is intrinsic, n-doped, or p-doped. When the Fermi level is located precisely at the Dirac point, charged carrier concentration is minimized and the graphene is said to be intrinsic. It is important to note that carrier concentration does not vanish at the Dirac point because of imperfections such as charged impurities and electron-hole "puddles" [20]–[22]. When the Fermi level is located above the Dirac point, graphene is n-doped and electrons represent the primary means of conduction. Alternatively, when the Fermi level is below the Dirac point, the graphene is p-doped and "holes" (i.e. the absence of electrons) represent the primary means for conduction. **Figure 1.4** depicts the different Fermi level locations in graphene along with the resulting *I-V* characteristic.

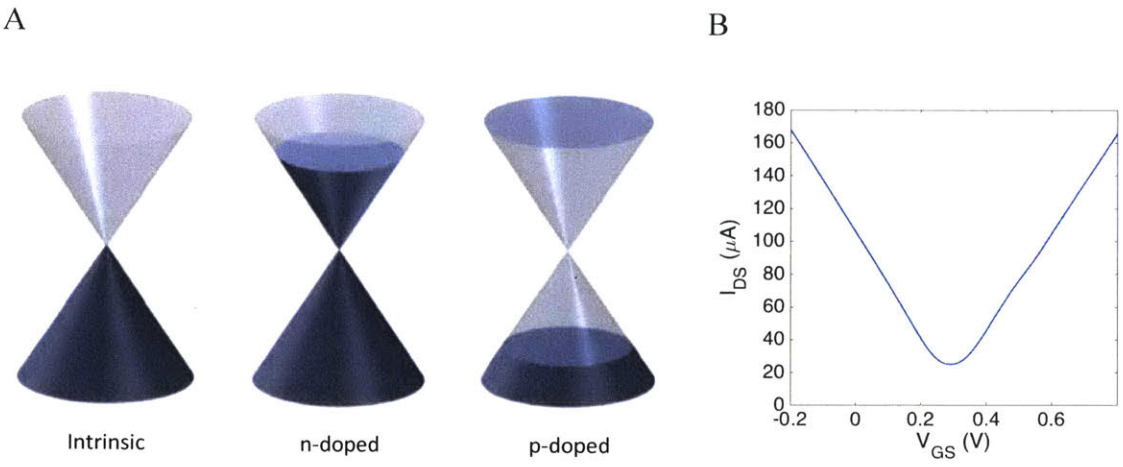

Figure 1.4: A) Fermi level location in intrinsic, n-doped, and p-doped graphene [23]. B) Graphene *I-V* characteristic.

Graphene may be synthesized using a number of methods. Monolayer and few layer graphene may be isolated by repeated mechanical exfoliation of highly oriented pyrolytic graphite (HOPG) [24]–[26]. Graphene may also be grown epitaxially by thermal decomposition of silicon carbide [27]–[29]. In this process, silicon carbide is annealed at high temperature—typically above 1000°C—in an inert gas. This causes desorption of silicon and subsequent bonding of carbon to form epitaxial graphene. Lower quality and multilayered graphene films are also commonly synthesized through the reduction of graphene oxide [30]–[33]. Finally, graphene may be synthesized using chemical vapor deposition (CVD). In this process, methane is flowed over a metal foil—usually nickel or copper—at high temperature resulting in graphene formation atop the metal surface. CVD is the most practical synthesis method as it is capable of producing large sheets with uniform material properties at relatively low cost [34].

CVD graphene synthesis may be achieved by flowing methane over a number of transition metals including cobalt, ruthenium, nickel, and copper [35]–[38]. In this

process, the metal substrate serves as a catalyst for methane decomposition as given by the chemical reaction (1.1).

$$CH_4 \rightarrow C + 2H_2 \tag{1.1}$$

The transition metal substrate provides nucleation sites for graphene growth [39]. Copper is the most common substrate because graphene synthesis self-terminates after the formation of a monolayer. This is attributed to low carbon solubility in copper, which prevents additional layers of graphene from forming via the out diffusion of carbon from the copper substrate. **Figure 1.5** illustrates the CVD synthesis process for graphene along with the resulting relatively large-are and uniform graphene film. Graphene may be transferred onto arbitrary substrates using polymethyl methacrylate (PMMA) or some other polymer to provide mechanical support [40]–[43].

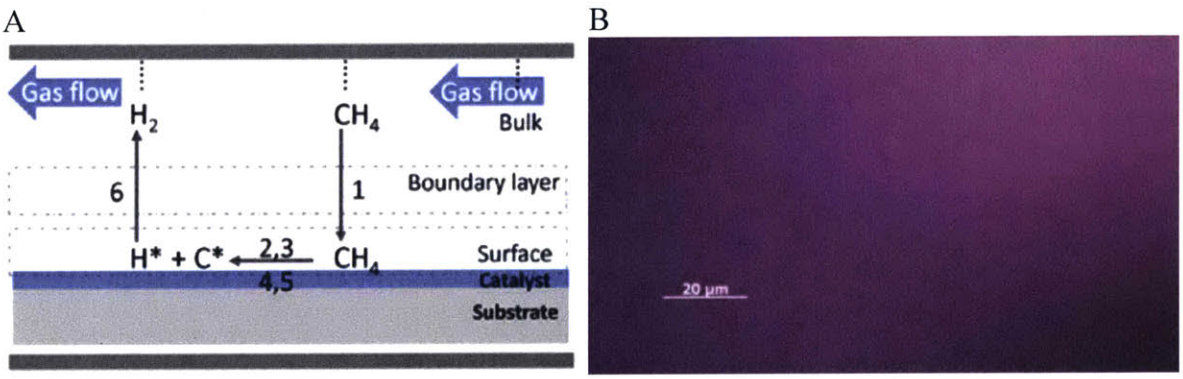

Figure 1.5: A) CVD graphene synthesis depicting formation from methane decomposition and carbon nucleation at the copper substrate—reproduced from [39]. B) Optical microscope image of a large-area intact and clean CVD graphene (after transfer onto a Si/SiO_2 wafer substrate).

Commercial-grade graphene is now available from a number of suppliers. ACS Material and Graphenea Inc., for instance, both provide "easy transfer" graphene in which the graphene-PMMA film comes with the copper foil already removed. Some suppliers now also provide large-area graphene synthesis and transfer services. This enables wafer-scale manufacturing using graphene, eliminates inconsistencies associated with manual transfer, and provides enhanced quality. A unique and convenient feature of graphene transfer is that failed transfers are easily removed using oxygen plasma. This allows graphene to be re-transferred repeatedly until certain quality and yield requirements are met.

1.2 Graphene Sensing

To fully motivate graphene's use as a sensor material, it is useful to provide context around graphene's discovery and the evolution of graphene research in other domains. The timing of graphene's discovery coincided with a time in which silicon-based digital electronics were reaching their physical limits. Graphene's exceptional electric properties led many to believe it could potentially revolutionize modern electronics and usher a next phase in Moore's Law. Moore's Law, named after Gordon Moore, a co-founder of Fairchild Semiconductor and Intel Corporation, is the observation that the number of transistors per unit area doubles approximately every 18 months [44]. This has been a guiding principle in the semiconductor industry since the 1970s and represents an exponential rate of technological advancement that, in many ways, society has grown accustomed to. With a plateau in sight, it was—and is—natural to look for alternatives such as graphene as a means to continue this trend.

Although graphene possesses exceptional electrical properties, early pioneering researchers—many of them physicists—did not recognize the important role of a bandgap in modern silicon-based digital electronics [17], [33], [45]–[47]. A bandgap enables switching between conducting and non-conducting in digital electronics (i.e. on and off states). This, coupled with their complementary nature, allows digital electronics to dissipate power only during active switching or active computation. This enables very low static power consumption and low heat dissipation (neglecting gate leakage). These features allow digital electronics to be miniaturized and packed more densely producing exponential increases in compute power per unit area over the last 50 years. Because graphene lacks a bandgap, however, a great deal of research focused on bandgap engineering through chemical and geometric modifications. This includes band gap engineering through doping and functionalization, nanoribbon patterning, and voltage biasing in bilayer graphene [48]–[53]. To date, however, no solutions exist enabling graphene's application to digital electronics.

The chief motivation for this thesis is to pivot from forcing graphene into the domain of digital electronics. The objective is to take graphene's properties, as is, and attempt to identify alternative devices and applications for which it may be more innately suited. Graphene's unique combination of electrical, chemical, mechanical, and optical properties, make it particularly promising for chemical and biological sensing applications. Like digital electronics, sensing applications represent a large markets and areas of high impact. In addition, as one of the main interfaces between digital electronics and the world, much of the data being processed in fact originates from sensors. This is becoming even more true in an increasingly connected and data-driven

world and with the advent of technologies such as the internet of things (IoT). This is the context and motivation for the exploration of graphene as a sensing material.

The nature of charge carrier transport in graphene makes it a promising sensing material. While much of graphene's mechanical stability results from in-plane σ-bonds, carrier transport in graphene arises from the π-bonds that exist above and below the lattice of carbon nuclei. These π-bonds, which given rise to graphene's electrical properties, are readily influenced by environmental changes. This makes graphene a promising material for transduction, the process by which chemical signals may be transformed to electrical ones. The exposed π-bonds provide graphene with innate sensitivity to environmental changes [54]. As an all-surface material, graphene has also been shown capable of extreme sensitivity capable of single molecule detection [55].

Graphene's other electrical, chemical, mechanical, and optical properties also add to its promise as a material for chemical and biological sensing applications. From an electrical standpoint, graphene has bee shown to possess room temperature mobilities in excess of 50,000 cm^2/Vs, which translates into high speed and high transconductance sensors [56]–[58]. Graphene field-effect transistors (FETs) have also been shown capable of voltage gains making them suitable for signal amplification in biological applications such as electrophysiology [59]. Graphene's chemical stability enables it to directly interface with the electrolytic environments found in many chemical and biological sensing applications and to take advantage of the ultrahigh capacitance due to the electric double layer phenomenon [60]–[65]. Graphene also exhibits a wide electrochemical potential window of approximately 2.5 V in in many electrolytes including solutions mimicking physiological conditions such as phosphate buffered saline

[66]. Mechanically, graphene possesses a high Young's modulus of 1 TPa, a breaking strength of 42 N/m, and mechanical flexibility making it potentially useful for flexible and smart skin sensing applications [67]–[70]. Extreme thinness also allows minimal light absorption in the visible spectrum making graphene suitable for transparent sensing applications [71]–[73]. Graphene's atomically thin carbon composition also makes it potentially very low cost with chemical vapor deposition synthesis enabling large-area and uniform synthesis [37], [38]. Graphene is unique with regards to many other sensing materials in that it can be transferred to arbitrary substrates such as transparent substrates, flexible polymers, and silicon wafers for traditional semiconductor manufacturing [74].

A number of graphene-based chemical and biological sensing devices have been developed in recent years. The vast majority of these sensors fall into one of three categories: optical, electrochemical (electrode-based), or FET-based. Optical graphene sensors typically offer the benefit of detection without adversely affecting the chemical environment [75]. Optical sensing approaches, however, often require an arrangement of light sources, mirrors, and filters making miniaturization and low-cost solutions difficult. Electrode-based graphene sensors offer simple construction and have been show to detect a range of analytes [76]–[83]. They are extremely limited, however, in terms of scalability and the ability to sense multiple analytes simultaneously [84]–[86]. Graphene FET-based sensing approaches offer a number of advantages. They provide the ability to detect a range of analytes similar to their electrode-based counterparts [34]. They also offer the benefits of miniaturization and scalability into large arrays [87]. Lastly, graphene FET-based sensing approaches allow for tuning of graphene's electrical properties for optimized sensitivity and signal amplification [88]–[90].

1.3 Graphene Electrolyte-Gated Field-Effect Transistor and Chemiresistive Sensors

This thesis focuses on two types of graphene sensors that are closely related: chemiresistive and electrolyte-gated field-effect transistors (EGFET). Graphene EGFETs are a particular type of graphene FET that can be gated through an electrolytic medium making it useful for many chemical and biological applications. Graphene EGFETs consist of a graphene channel between two conductive source-drain contacts. Some portion of the graphene channel is exposed to the sensing environment either directly or via some form of functionalization. This allows environmental changes to alter the doping in the graphene channel, and hence conductivity of the graphene EGFET. These devices are used in conjunction with some form of readout circuitry to measure the electrical signals and quantify environmental changes. No material constraints are imposed on the graphene EGFET substrate, which can range from glass and silicon to flexible polymers. **Figure 1.6A** depicts a typical layout for a graphene EGFET. Chemiresistive graphene sensors are virtually identical as shown in **Figure 1.6B**, but do not allow for gating of the graphene channel. Chemiresistive sensors can be applied to solution and gas-phase sensing.

A

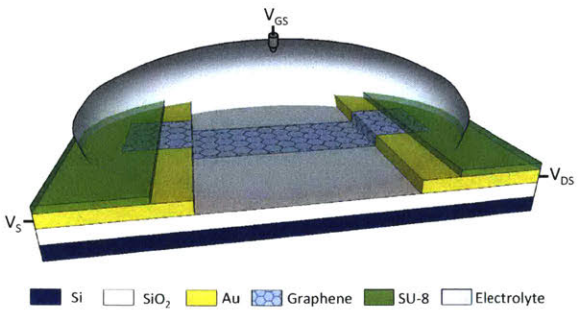

B

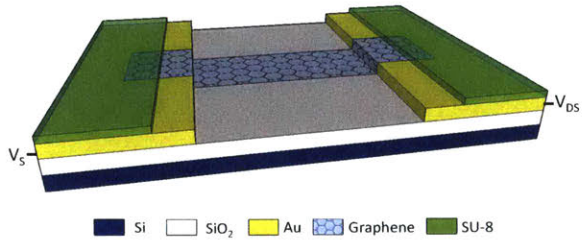

Figure 1.6: A) Graphene EGFET sensor with recessed passivation. B) Chemiresistive graphene sensor with recessed passivation. V_S, V_{DS}, and V_{GS} represent voltages applied to the source, drain, and gate, respectively.

Graphene chemiresistive and EGFET sensors can be thought of as relying on one of two operating mechanisms: shift in *I-V* characteristic or V_{GS} modulation. In *I-V* characteristic shifts, a change in the environment alters the graphene Fermi level making it either more n-type or p-type. This results in a lateral shift of the graphene *I-V* characteristic. In applications such as electrogenic cell sensing, graphene EGFETs can be thought of as operating based on V_{GS} modulation. For instance, when a neuron produces an action potential at the graphene surface, it alters the composition of ions found at the graphene surface. This can be thought of as an effective modulation in the gate-source voltage V_{GS}. The change in the effective V_{GS} then results in a detectable change in source-drain I_{DS} current. **Figure 1.7** depicts idealized versions of the *I-V* characteristic shift and V_{GS} modulation sensing mechanisms.

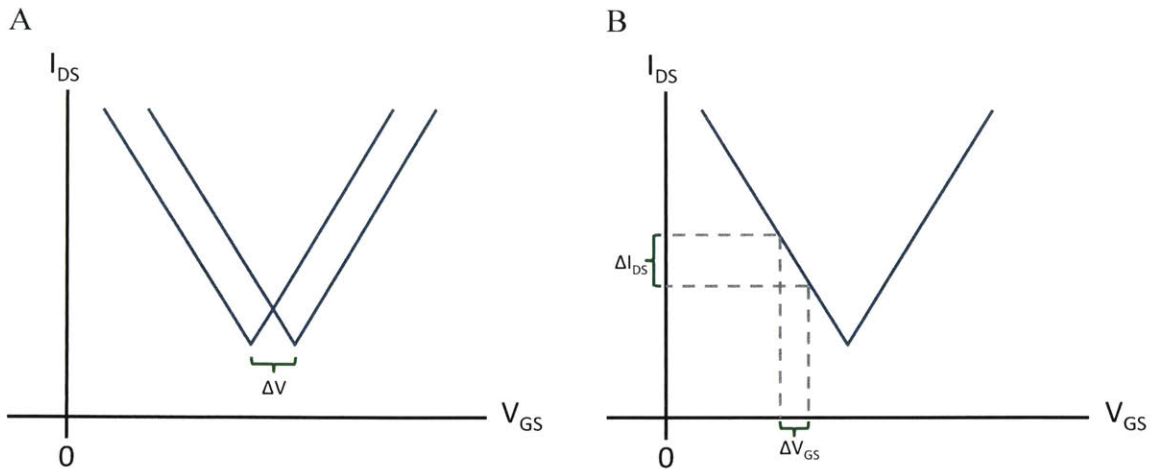

Figure 1.7: A) Change in electrolyte composition alters graphene doping and laterally shifts the *I-V* characteristic. B) Change in ionic composition near the graphene surface due modulates the effective source-gate voltage V_{GS}.

1.4 Relevant Principles in Electrochemistry

Use of graphene in chemical and biological sensors requires some basic familiarity with select concepts in electrochemistry. More specifically, graphene EGFETs take advantage of two principles in electrochemistry: electric double layer formation and electrochemical potential windows. Electric double layer formation occurs whenever a material is interfaced with an electrolyte of a different electrochemical potential. This causes either cations or anions within the electrolyte to preferentially migrate toward the surface. This charge separation typically occurs over a very short distance of a few nanometers with the bulk electrolyte remaining electroneutral. As a result, electric double layer capacitances can be quite large and range from a few $\mu F/cm^2$ to tens of $\mu F/cm^2$. Several models have been developed describing the electric double layer phenomenon. The most common models are the Helmholtz model, Gouy-Chapman model, and the Gouy-Chapman-Stern model.

Helmholtz is credited with discovery the electric double layers and assumed all ions were specifically adsorbed onto the material surface [91]. This led Helmholtz to model electric double layers as simple parallel plate capacitors. In some very limited scenarios, this may serve as an adequate approximation. The Helmholtz model, however, fails to capture the ability ions to form a concentration gradient near the surface due to thermodynamic diffusion. The Gouy-Chapman model captures this diffuse electric double layer behavior by balancing the fact that ions are subject to diffusive and electrostatic forces within the electrolyte [92], [93]. This model is also known as the Poisson-Boltzmann model, which can only be solved analytically for a handful of cases and also typically requires Debye-Hückel linearization to make progress [94]. The Gouy-Chapman-Stern model combines Helmholtz and Guoy-Chapman models to allow for specifically adsorbed ions as well as a diffuse region [95]. **Figure 1.8** depicts the three different models for electric double layers.

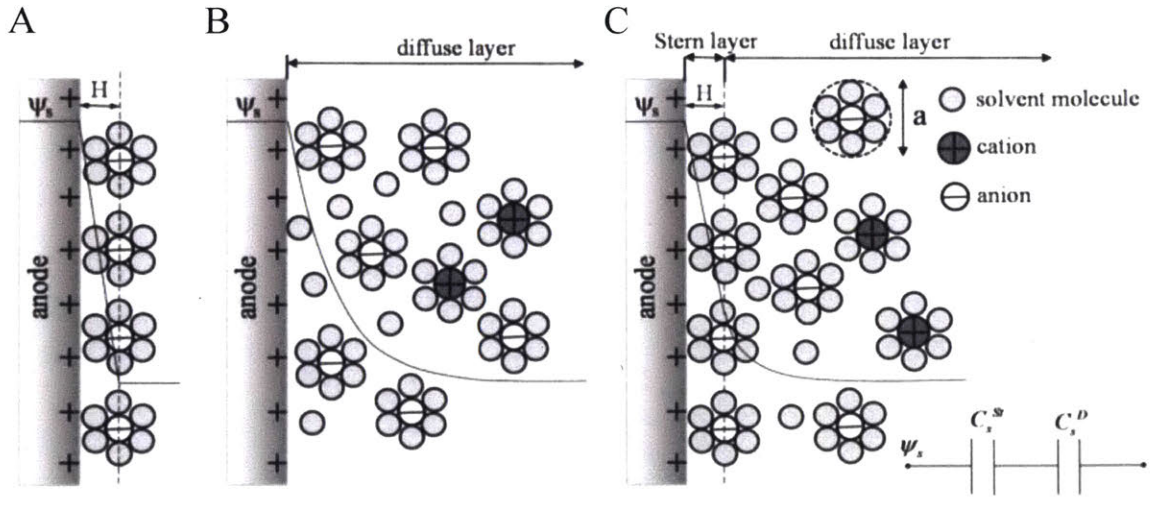

Figure 1.8: The three most common models used to describe electric double layers A) Helmholtz model B) Gouy-Chapman model C) Gouy-Chapman-Stern model [96].

One of the key drawbacks associated with these models is that they treat ions as point charges. This results unrealistically high ionic concentrations even for dilute electrolytes at low applied voltages (a few tenths of a volt). In actuality, ions occupy some volume and have limited packing density. Ions also carry hydration shells, which further increase their effective size. This led to the development of more sophisticated models such as the modified Poisson-Boltzmann (MPB), which accounts for steric effects and is described by (1.1). As the name suggests, the model combines the Poisson and Boltzmann equations and has been modified to take steric effects into consideration.

$$\nabla^2\psi = \frac{z\,q\,N_A\,c_o}{\epsilon}\frac{2\sinh\left(\frac{q\,z\,\psi}{k_BT}\right)}{1+2\,v\sinh\left(\frac{q\,z\,\psi}{k_BT}\right)^2} \tag{1.1}$$

Here ψ is the potential, c_o represents the ion species bulk concentration, z is the ion valency, N_A is Avogadro's number, k_B is the Boltzmann constant, ϵ is the permittivity, q is the elementary charge, and T is temperature [97]. Steric effects are included via the denominator term and are governed by the packing parameter v, which represents the maximum density to which ions may accumulate and is given by (1.2)

$$v = 2a^3c \tag{1.2}$$

where a is the effective diameter of the ion species and c_o represents the bulk ion concentration.

It is important to note that the electric double layer capacitance is an interface effect that typically occurs within nanometers of the surface. The bulk of the electrolyte remains electroneutral and is typically referenced as $\psi = 0$. Because of this, the thickness or volume of the electrolyte has no effect on the capacitance. This is counterintuitive and in stark contrast to conventional dielectric capacitors whose capacitance exhibits inverse dependence on dielectric thickness. Unlike dielectric capacitors, electric double layer capacitance is not constant and exhibits some form voltage dependence.

Modeling electric double layers is further complicated by the fact that high ionic concentrations affect the relative permittivity of the electrolyte. Because of this, electrolyte permittivity is not constant but exhibits some form of spatial dependence. Secondary effects such as these make accurate modeling of electric double layers difficult. Physics-based models, however, are useful tools nonetheless in building intuition and understanding general trends within electric double layers.

Solutions to the modified Poisson-Boltzmann are presented in **Figures 1.9** and **1.10** to show how electrolyte composition, permittivity, and effective ion size influence the capacitance of the electric double layer. Solutions to the modified Poisson-Boltzmann model are difficult or impossible to solve analytically in many scenarios. As a result, solution results are obtained through a custom numerical simulation. Simulations are for a symmetric aqueous electrolyte and include steric effects. The relative permittivity of water is 78.3.

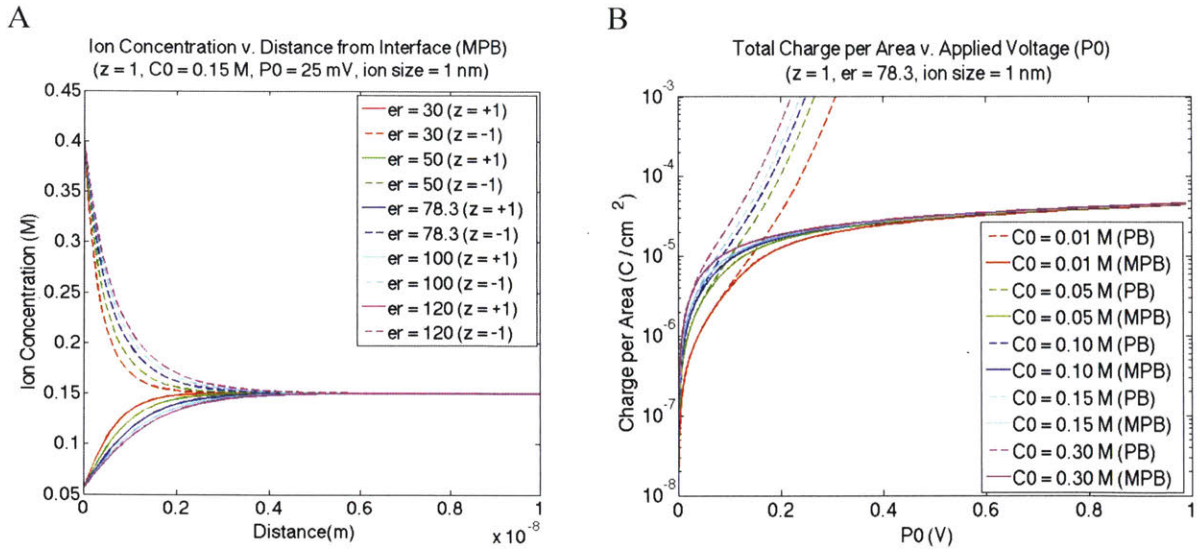

Figure 1.9: A) Cation and anion concentrations as a function of distance from the electrode surface for varying electrolyte permittivity. B) Electric double layer charge density as a function of electrode potential for various electrolyte concentrations. Solid lines represent are MPB solutions that include steric effects. Dashed lines are Poisson-Boltzmann solutions that neglect steric effects.

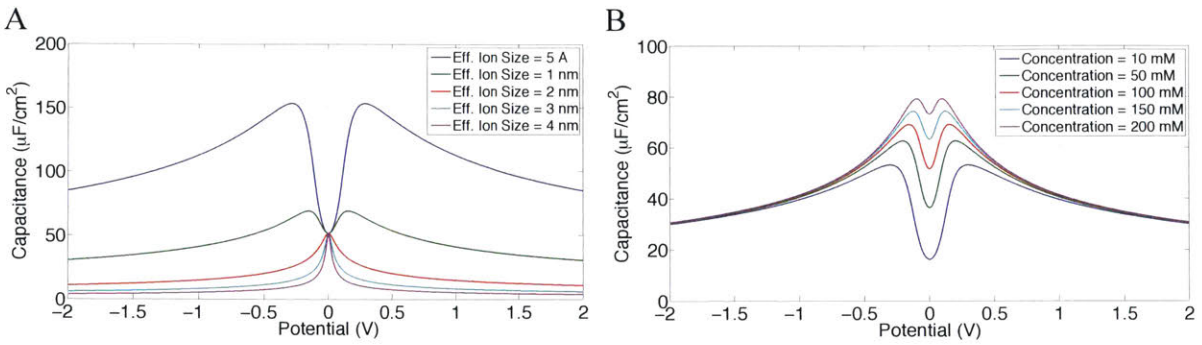

Figure 1.10: A) Electric double layer capacitance versus potential in 100 mM symmetric aqueous electrolyte for various effective ion sizes. B) Electric double layer capacitance versus applied potential with 1 nm effective ion size for various ion concentrations.

Another important concept in graphene EGFET operation is the electrochemical potential window. Although both graphene and electrolytes are conductive, application of a voltage across the graphene-electrolyte interface does not necessarily result in a

sustained (DC) current. This counterintuitive result stems from the fact that graphene possesses a wide electrochemical potential window in many electrolytic environments. This is not a new discovery as carbon-based electrodes have been commonplace in electrochemistry for years because of this feature, which enables the study of reactions that might otherwise be difficult to observe [98].

To sustain a DC current at the graphene-electrolyte interface, there must exist an accompanying reduction or oxidation (i.e. redox reaction) at the graphene surface involving one or more chemical species. For example, in the case of aqueous NaCl electrolyte, Na^+ must be reduced, Cl^- must be oxidized, or water must be split in order to create oxygen and hydrogen gases. Each of these reactions requires overcoming an activation barrier. These activation barriers are relatively high for many graphene-electrolyte interactions including aqueous NaCl and more complex electrolytes that mimic physiological conditions such as phosphate buffered saline (PBS). **Figure 1.11** depicts graphene's electrochemical potential window in 1 M aqueous NaCl as a reference.

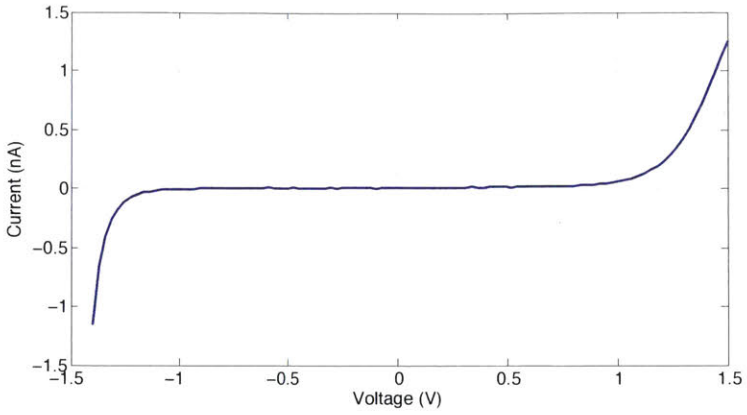

Figure 1.11: Graphene electrode current versus potential in 1 M aqueous NaCl using an Ag/AgCl reference electrode and 1 mm diameter platinum button counter electrode. The dimension of the graphene-electrolyte interface is 40 μm by 20 μm.

Currents due to redox reactions at the graphene-electrolyte interface can be described by the Butler-Volmer equation, which is given by (1.3)

$$j = j_o\left[e^{\alpha_a nF\eta/RT} - e^{-\alpha_c nF\eta/RT}\right] \tag{1.3}$$

where j is the current density, j_o is the exchange current density, α_a is the anodic charge transfer coefficient, α_c is the cathodic charge transfer coefficient, n is the number of electrons involved in the reaction, R is the universal gas constant, T is the absolute temperature, and η is the overpotential. The graphene-electrolyte interface possesses a low exchange current density. This results in a large potential range with negligible current flow at the graphene-electrolyte interface. Lack of DC current coupled with ion migration due to the imposed electric field means the interface is acting as a capacitor. A

wide potential window can potentially allow very high charge accumulation, which has spurred research into graphene-based supercapacitors [32], [99]–[101].

For graphene EGFET operation, a wide potential window enables gating over a wide range in various electrolytes without inducing redox currents. Absence of redox reactions limits potential damage to the graphene and its electrical properties. It also allows graphene EGFETs to operate without need for any protective coating or dielectric. This direct interface with the electrolyte enables graphene EGFETs to take full advantage of the high interface capacitances due to electric double layer formation.

Chapter 2: DC Modeling of Graphene EGFETs

2.1 Introduction

This chapter develops an accurate physics-based DC model for graphene EGFETs as a means to gain a comprehensive understanding of the underlying physics and operating mechanisms in this new class of device. Device models are critical in the development of any new technology. They accelerate exploration of the design space by freeing the user from needing to physically fabricate devices to explore every scenario of interest. In doing so, device models can be a particularly useful in identifying the strengths of a new technology and guiding its development into specific applications. Device models are also critical in the design of readout circuitry for any new technology that will inevitably be integrated within some larger system. Device models also enable application-specific performance optimization.

A number of DC models have been developed to study and predict the behavior of dielectric-gated graphene field-effect transistors (FETs) [102]–[107]. Little work, however, has been reported for graphene electrolyte-gated field-effect transistor (EGFET) models [108]. Graphene EGFET models represent an increase in complexity over graphene dielectric-gated FETs because the top-gate capacitance cannot be considered constant. The top-gate capacitance of graphene EGFETs, which is comprised of the electrical double layer capacitance and graphene quantum capacitance, varies as a function of ionic species, ionic concentration, and also spatially along the graphene channel [97], [109].

This work presents a model for graphene electrolyte-gated field-effect transistors (EGFETs) that incorporates the effects of the graphene-electrolyte interface and the

quantum capacitance of graphene [110]. The model is validated using experimental data collected from fabricated graphene EGFETs and is employed to extract device parameters such as mobility, minimum carrier concentration, interface capacitance, contact resistance, and effective charged impurity concentration. The proposed graphene EGFET model accurately determines a number of properties necessary for circuit design such as current-voltage characteristics, transconductance, output resistance, and intrinsic gain. The model can also be used to optimize the design of EGFETs. For example, simulated and experimental results show that avoiding the practice of partial channel passivation enhances the transconductance of graphene EGFETs.

2.2 Fabrication Process

Graphene EGFETs were fabricated and measured to evaluate the model's ability to fit experimental data. A clean 4-inch silicon wafer coated with 5 μm of spin-on polyimide (HD-8820) and annealed at 375 °C in 700 sccm argon to prevent outgassing in subsequent high-temperature steps. Source and drain Ti/Au/Pt (10/100/20 nm) contacts were patterned using liftoff photolithography. Monolayer graphene was then grown on copper foils using CVD and transferred over the entire substrate using polymethyl methacrylate (PMMA) [39]. The PMMA was removed using an acetone and isopropanol. The PMMA residue was further reduced by annealing at 350 °C in 400 sccm argon and 700 sccm hydrogen for 3 hours. The graphene channel regions were defined using MMA/OCG825 photoresist stacks and helium and oxygen plasma at 16 and 8 sccm, respectively. The MMA/OCG825 photoresist stacks were removed using acetone and isopropanol. The samples were annealed at 350 °C in 400 sccm argon and 700 sccm

hydrogen for 3 hours to further remove MMA residue. The entire wafer was passivated with 2.4 μm of SU-8 2002 and windows were photodefined to provide electrolyte access to the graphene EGFET channel regions. The SU-8 was then hard-baked at 150 °C for 5 minutes. An aqueous electrolyte droplet of 100-mM NaCl was pipetted over the graphene EGFET channel regions and a reference electrode was inserted into the droplet to gate the devices. Aqueous 100-mM NaCl was chosen because of its symmetry and similarity to physiological osmolarity. Similar devices were fabricated on 300-nm SiO_2 to facilitate better wire bonding, which was required for interface capacitance measurements.

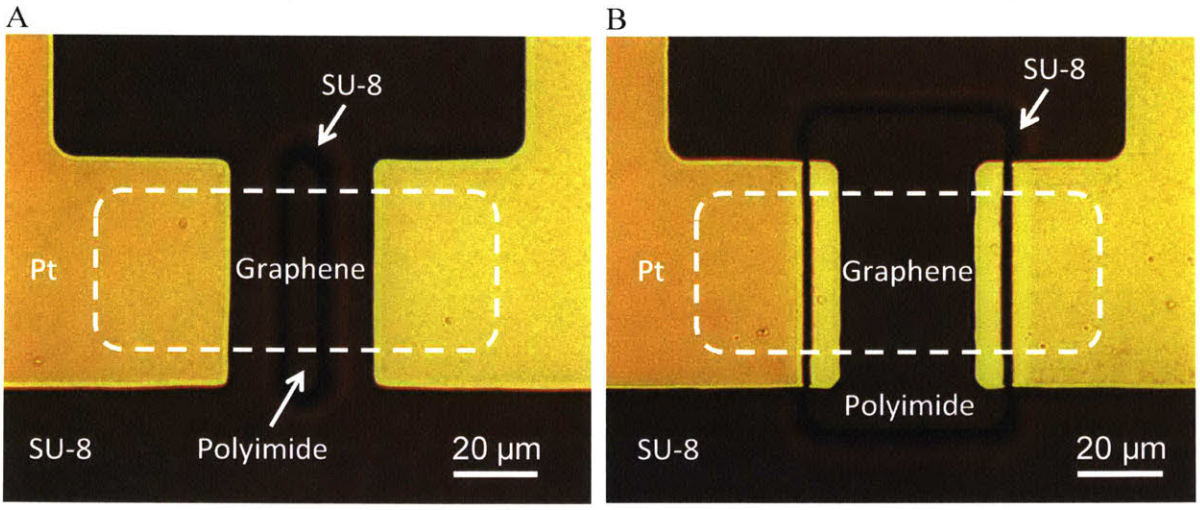

Figure 2.1: A) Optical microscope image of a graphene EGFET on a polyimide substrate with SU-8 passivation extending into the graphene channel region. B) Optical microscope image of a graphene EGFET with recessed SU-8 passivation leaving portions of the source drain contact metal exposed to the electrolyte.

2.3 Graphene Electrical Double Layer Capacitance

Immersion of graphene in an electrolyte results in the accumulation of ions at the graphene surface due to differences in electrochemical potentials. This phenomenon is termed an electric double layer. The capacitance of the electric double layer is large

enough that accurately modeling the graphene-electrolyte interface capacitance requires inclusion of the graphene quantum capacitance. Quantum capacitance is proportional to the density of states and is typically the limiting capacitive component for two-dimensional materials such as graphene. The graphene quantum capacitance is given by (2.1) and (2.2)

$$C_Q = \frac{2q^2}{\hbar v_F \sqrt{\pi}} (|n_G| + |n^*|)^{1/2} \tag{2.1}$$

$$n_G = \left(\frac{qV_{ch}}{\hbar v_F \sqrt{\pi}} \right)^2 \tag{2.2}$$

where $\hbar$ is the reduce Planck constant, v_F is the Fermi velocity, n_G is the carrier concentration induced by the gate voltage, n^* is the effective charged impurity concentration, and V_{ch} is the electric potential of the graphene channel [109].

Experimental data shows that the graphene-electrolyte interface capacitance, $C_{TOP,EXP}$, may be modeled using a parallel plate capacitor, $C_{EDL,EFF}$, in series with the graphene quantum capacitance, C_Q. As a hydrophobic material, graphene repels aqueous electrolytes resulting in what may be modeled as an angstrom-scale gap between the electrolyte and graphene surface. This forms a parallel plate capacitor, which reduces the complex voltage-dependence capacitance typical of electric double layers. This effect was previously measured and modeled and is reproduced for this work [57], [111], [112].

Experimental data also includes a parallel capacitive component due to device leads, C_O. The interface capacitance is measured at 100 Hz with an Ag/AgCl reference

electrode using a Gamry Reference 600 potentiostat. The measurement was taken in 1M aqueous NaCl. The measured data is fit to the capacitive model using the Levenberg-Marquardt algorithm from the MATLAB optimization toolbox (**Figure 2.2**). The data confirms the applicability of the interface capacitance model in the current-voltage graphene EGFET model.

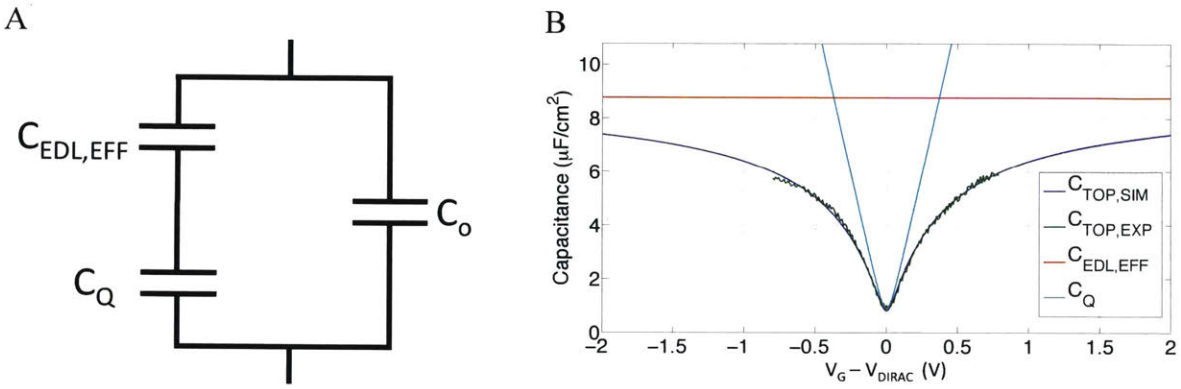

Figure 2.2: A) Capacitive components comprising the overall graphene-electrolyte interface capacitance. B) Simulated versus experimental top-gate capacitance for a graphene EGFET on SiO_2. The device has W/L = 40μm/40μm where the center 20μm is unpassivated. $C_{EDL,EFF}$ = 8.8 μF/cm^2, n* = 1.0×10^{11} /cm^2, C_O = 11.3μF/cm^2.

2.4 DC Graphene EGFET Model

The current at any given position along the channel is determined by the product of the carrier concentration and the carrier drift velocity, which is scaled appropriately by the elementary charge and channel width. This principle combined with current continuity enables calculation of the graphene EGFET current and the corresponding channel potential profile. **Figure 2.3** depicts a typical layout for a graphene EGFET.

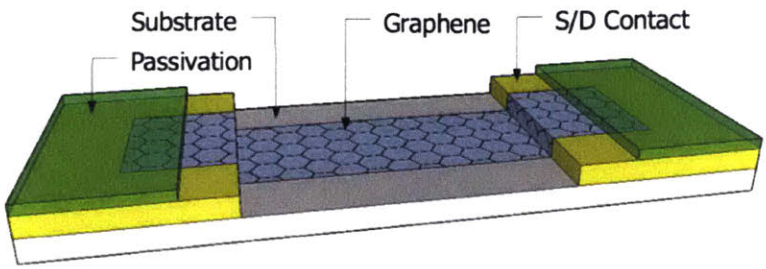

Figure 2.3: Graphene EGFET structure with mostly passivated source and drain regions.

The channel current is given by the equation (2.3)

$$I_{DS} = q\,W\,n\,v_{drift} \tag{2.3}$$

where q is the elementary charge, W is the channel width, n is the carrier concentration, and v_{drift} is the carrier drift velocity. The drift velocity may be rewritten as (2.4)

$$v_{drift} = -\mu\frac{dV}{dx} \tag{2.4}$$

where μ is the carrier mobility, and V is the channel potential which is a function of position. This model assumes carrier mobility is equal for holes and electrons and independent of the carrier concentration. The carrier concentration is a function of potential and is given by (2.5)

$$n(V) \approx \sqrt{n_o^2 + \left[C_{TOP}(V)\left[V_{GS,TOP} - V - V_o\right]/q\right]^2} \tag{2.5}$$

where n_o is the minimum carrier concentration [20], [22], C_{TOP} is the top-gate capacitance, $V_{GS,TOP}$ is the applied top gate voltage, and V is the potential along the channel. V_o represents the potential at the Dirac point given by (2.6)

$$V_o = V^0_{GS,TOP} + \frac{C_{BACK}}{C_{TOP}(V)}\left(V^0_{GS,BACK} - V_{GS,BACK}\right) \tag{2.6}$$

where $V^0_{GS,TOP}$ and $V^0_{GS,BACK}$ are the locations of the Dirac point as experimentally determined from top gating and back gating, respectively. C_{BACK} is the back-gate capacitance. The majority of graphene EGFETs – including the ones examined in this work – are fabricated on thick insulating substrates to provide structural support and ensure the measured source-drain current stems solely from the graphene channel. As a result, the back gate capacitance is far less the than top gate capacitance, which is typically several $\mu F/cm^2$. The equation for threshold voltage can then be simplified to (2.7).

$$V_o = V^0_{GS,TOP} \tag{2.7}$$

Including the effects of saturation velocity and contact resistance produces (2.8) describing the channel current. Contact resistances are assumed symmetric. It is also important to note that chemical and biological sensors employing graphene EGFETs are typically biased at low voltages to avoid the undesirable reduction of chemical species in

the solution. Because of this, carrier drift velocity is typically well below the saturation velocity. Saturation velocity is included nonetheless for completeness.

$$I_{DS} = \frac{q\mu \frac{W}{L} \int_{I_{DS}R_C}^{V_{DS}-I_{DS}R_C} \sqrt{n_o^2 + \left[C_{TOP}(V)\left[V_{GS,TOP} - V - V_o\right]/q\right]^2}\, dV}{1 + \left|\frac{\mu(V_{DS} - 2I_{DS}R_C)}{Lv_{sat}}\right|} \tag{2.8}$$

Because the top-gate capacitance is a function of potential, this equation cannot readily be integrated. As a result, a numerical equation (2.9) describing the channel potential profile is employed where *h* represents the step width.

$$V(x+h) = V(x) + \frac{h \cdot I_{DS}\left[1 + \left|\frac{\mu(V_{DS} - 2I_{DS}R_C)}{Lv_{sat}}\right|\right]}{q\mu W\sqrt{n_o^2 + \left[C_{TOP}(V_{GS,TOP} - V(x) - V_o)\left[V_{GS,TOP} - V(x) - V_o\right]/q\right]^2}} \quad 0 \le x \le L \tag{2.9}$$

The graphene EGFET channel current problem may be reformulated as a root finding problem and solved using the bisection method [113]–[118]. This is a robust method with guaranteed convergence provided that the initial bounds span the solution and that the solution is unique. The pseudocode in **Figure 2.4** describes the bisection method and its adaptation to the EGFET current and channel potential problem.

Bisection Method Pseudocode

$x_{LOW} < x_{ROOT} < x_{HIGH}$

$x_{MID} = 0.5\ (x_{LOW} + x_{HIGH})$

while$(f(x_{MID}) >$ Error Tolerance)

    if$(f(x_{LOW}) \cdot f(x_{MID}) < 0)$

        $x_{HIGH} = x_{MID}$

    if$(f(x_{MID}) \cdot f(x_{HIGH}) < 0)$

        $x_{LOW} = x_{MID}$

    $x_{MID} = 0.5\ (x_{LOW} + x_{HIGH})$

Graphene EGFET Problem Pseudocode

$I_{DS,LOW} < I_{DS} < I_{DS,HIGH}$

$I_{DS,MID} = 0.5\ (I_{DS,LOW} + I_{DS,HIGH})$

while$(V_{DS,ERROR}(I_{DS,MID}) >$ Error Tolerance)

    if$(V_{DS,ERROR}(I_{DS,LOW}) \cdot V_{DS,ERROR}(I_{DS,MID}) < 0)$

        $I_{DS,HIGH} = I_{DS,MID}$

    if$(V_{DS,ERROR}(I_{DS,MID}) \cdot V_{DS,ERROR}(I_{DS,HIGH}) < 0)$

        $I_{DS,LOW} = I_{DS,MID}$

    $I_{DS,MID} = 0.5\ (I_{DS,LOW} + I_{DS,HIGH})$

Figure 2.4: Illustration of the bisection method pseudocode along with adaptation to the graphene EGFET channel current problem.

$I_{DS,LOW}$ is initialized to zero. $I_{DS,HIGH}$ is initialized to the maximum possible channel current value. $I_{DS,MID}$ is then calculated and employed as the initial guess for I_{DS}. Based on the I_{DS} guess, the channel potential profile may be calculated. The first and last points of the profile are used to calculate V_{DS}. If the calculated V_{DS} is greater than the V_{DS} input parameter, the I_{DS} guess was too large and must be revised to a smaller value. Similarly, if the V_{DS} value is smaller than the V_{DS} input parameter, then the I_{DS} guess was too small and must be revised to a larger value.

Application of the bisection method algorithm causes the simulation to converge towards the unique solution where channel current I_{DS} and channel potential profile V(x) are in agreement. The solution obtained possesses some V_{DS} and I_{DS} error less than the user-specified maximum tolerable errors. The I_{DS} error tolerance exit condition is omitted from the pseudocode for simplicity and ease of illustration.

2.5 DC Graphene EGFET Model for Heterogeneous Top-Gate Capacitance

The ability to model heterogeneous top-gate capacitances is important for cases where source/drain region passivation extends into the channel region. This common practice is used to ensure complete passivation of the source/drain regions and minimize leakage current (**Figure. 2.5**).

The importance of modeling heterogeneous top-gate capacitances is not limited to the study of passivation schemes. This model also applies to the study of electrogenic cells, which due to their uncontrolled positioning may cover only a portion of the graphene channel. These cells act to modulate the top-gate capacitance over a limited region of the channel. From a modeling standpoint, this is equivalent to applying a thick layer of passivation in the regions unmodulated by the electrogenic cell.

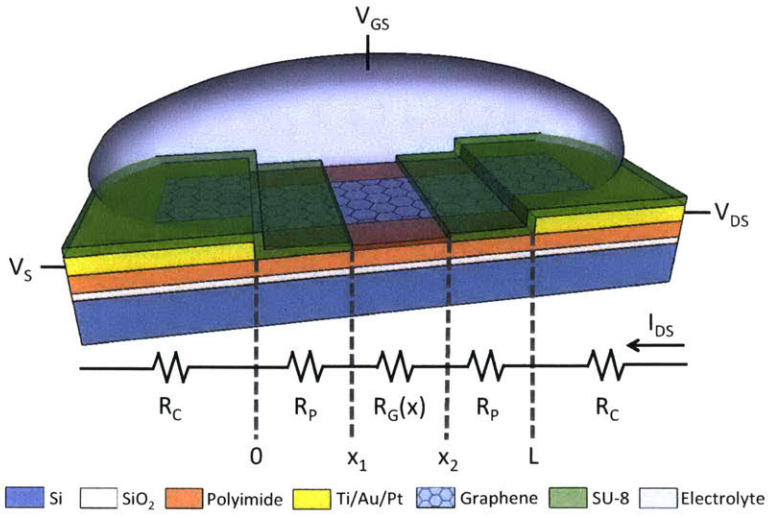

Figure 2.5: Graphene EGFET with heterogeneous top-gate capacitance due to non-self-aligned completely passivated source and drain regions.

Splitting the channel into regions corresponding to the different top-gate capacitances yields the piecewise numerical channel potential equation given by (2.10)

$$V(x+h)=\begin{cases} V(x)+\dfrac{h\cdot I_{DS}\left[1+\left|\frac{\mu_p(V_{DS}-2I_{DS}R_C)}{Lv_{sat,p}}\right|\right]}{q\mu_p W\sqrt{n_{o,p}^2+\left[C_{TOP,PASS}(V)\left[V_{GS,TOP}-V(x)-V_o\right]/q\right]^2}} & 0<x<x_1 \\ V(x)+\dfrac{h\cdot I_{DS}\left[1+\left|\frac{\mu(V_{DS}-2I_{DS}R_C)}{Lv_{sat}}\right|\right]}{q\mu W\sqrt{n_o^2+\left[C_{TOP}(V)\left[V_{GS,TOP}-V(x)-V_o\right]/q\right]^2}} & x_1\le x\le x_2 \\ V(x)+\dfrac{h\cdot I_{DS}\left[1+\left|\frac{\mu_p(V_{DS}-2I_{DS}R_C)}{Lv_{sat,p}}\right|\right]}{q\mu_p W\sqrt{n_{o,p}^2+\left[C_{TOP,PASS}(V)\left[V_{GS,TOP}-V(x)-V_o\right]/q\right]^2}} & x_2<x<L \end{cases} \tag{2.10}$$

where μ_p is the graphene mobility in the passivated regions, $n_{o,p}$ is the minimum carrier concentration in the passivated regions, and $C_{TOP,PASS}(V)$ is the top-gate capacitance in the passivated regions.

Alternatively, one can realize that the passivated graphene regions may be modeled as an additional series resistance described by (2.11).

$$R_P=\frac{1}{q\mu_p\sqrt{n_{o,p}^2+\left[C_{TOP,PASS}(V)\left[V_{GS,TOP}-V(x)-V_o\right]/q\right]^2}}\cdot\frac{L}{W} \tag{2.11}$$

For the typical case where the passivation regions possess a very small capacitance of nF/cm^2, the equation for the passivation series resistance can be simplified to a constant as shown by (2.12).

$$R_P \approx \frac{1}{q\,\mu_p\,n_{o,p}} \cdot \frac{L}{W} \tag{2.12}$$

This produces the revised form of the graphene EGFET channel current equation (2.13). It now becomes evident that introducing passivation into the graphene channel regions acts to increase the overall series resistance.

$$V(x+h) = V(x) + \frac{h \cdot I_{DS}\left[1 + \left|\frac{\mu\left(V_{DS} - 2I_{DS}(R_C + R_P)\right)}{Lv_{sat}}\right|\right]}{q\mu W\sqrt{n_o^2 + \left[C_{TOP}(V)\left[V_{GS,TOP} - V(x) - V_o\right]/q\right]^2}} \quad x_1 \le x \le x_2 \tag{2.13}$$

2.6 Minimum Conduction Point

The location of the minimum conduction point, also known as the Dirac point, is a key parameter in the current-voltage characteristic. It marks the transition from negative to positive transconductance and approximates $V^0_{GS,TOP}$, which provides a measure of graphene doping. With this in mind, it is important to develop an understanding of what value of V_{GS} produces the minimum value of I_{DS}. This particular value of V_{GS} is defined as V_{DIRAC}. To analytically arrive at an equation for V_{DIRAC} and gain an understanding of the parameters that determine the location of V_{DIRAC}, a simplified graphene EGFET equation (2.14) is employed where series resistance and velocity saturation are neglected.

$$I_{DS} = q\mu_o \frac{W}{L}\int_0^{V_{DS}} \sqrt{n_o^2 + \left[C_{TOP}(V)\left[V_{GS,TOP} - V - V_o\right]/q\right]^2}\,dV \tag{2.14}$$

The following derivation of V_{DIRAC} stems from the realization that the integral is minimized when the minimum of $n(V)$ falls precisely in the center of the integration bounds. In other words, I_{DS} is minimized when $\min(n(V)) = n(V_{DS}/2)$. This is depicted in **Figure 2.6**.

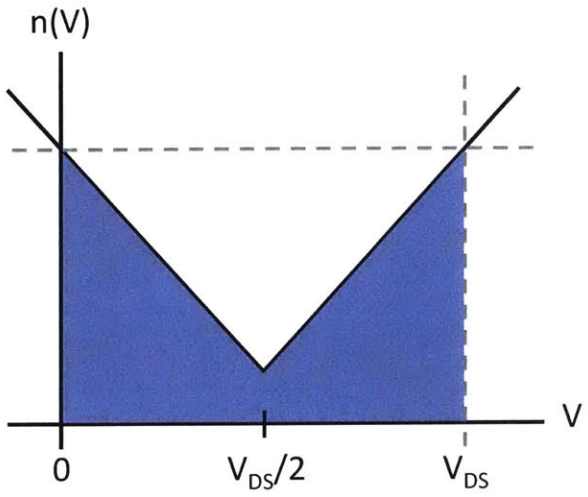

Figure 2.6: I_{DS} integral geometry to illustrate I_{DS} minimization when the n(V) minimum occurs at the center of the integration bounds.

The minimum of $n(V)$ occurs when $V = V_{GS,TOP} - V_o$. For the simplest case where V_{DS} is very small and $V_o = 0$, if $V = V_{GS,TOP}$ the graphene potential is equivalent to the applied potential $V_{GS,TOP}$. Thus no voltage bias is applied to the graphene and the total carrier concentration is equal to the minimum graphene carrier concentration. Alternatively, the location of the $n(V)$ minimum can be obtained by setting the derivative of $n(V)$ with respect to V equal to zero as shown in (2.15).

$$\frac{dn}{dV} = \frac{C_{TOP}(V_{DIRAC} - V - V_o)/q}{\sqrt{n_o^2 + [C_{TOP}(V_{DIRAC} - V - V_o)/q]^2}} = 0 \tag{2.15}$$

This leads to (2.16).

$$V_{DIRAC} - V - V_o = 0 \tag{2.16}$$

Recall that I_{DS} is minimized when the minimum of $n(V)$ is located in the center of the integration bounds. Thus $V = V_{DS}/2$, which leads to the final solution for the Dirac point given by (2.17).

$$V_{DIRAC} = V_o + \frac{V_{DS}}{2} \tag{2.17}$$

The slope between the V_{DIRAC} and V_{DS} should be roughly equal to 1/2. In addition, V_o may be extrapolated by tracing the minimum conduction point to $V_{DS} = 0$ V.

2.7 Model Evaluation

The graphene EGFET model is fit to experimental data obtained from a device with dimensions W/L = 40μm/30μm and recessed passivation. The device was measured using Pt wire pseudo-reference electrode. An aqueous electrolyte consisting of 100 mM NaCl was selected because of its symmetry and similarity to physiological osmolarity. The data is fit using bounded simulated annealing from MATLAB's optimization toolbox as shown in **Figure 2.7**. The extracted device parameters and sensitivity analysis are provided in Tables 2.1 and 2.2, respectively. The data is acquired by sweeping V_{GS} from

-0.2 to 1.2 V and V_{DS} from 10 mV to 300 mV. The experimental and simulation step size is 10 mV for both V_{GS} and V_{DS}. The V_{GS} step rate was 500 ms per 10 mV. In addition, a ten second hold time was allotted when resetting V_{GS} from 1.2 V to -0.2 V and incrementing V_{DS} by 10 mV. Further increasing the hold time and decreasing the sweep rate had little effect on the measured *I-V* characteristic meaning sufficient time was given for the ions to redistribute and for the electric double layer to reach steady state. The mean percent error for the entire data set is 2%. Simulated source-drain current, transconductance, output impedance, and intrinsic gain may be computed using finite differences and compared to experimental data as shown in **Figures 2.8-2.10**.

TABLE 2.1: SIMULATED ANNEALING EXTRACTED PARAMETERS

Parameters	Extracted	Reported	References
$\mathbf{V_{GS,TOP}^0}$	560 mV	N/A	--
$\mathbf{n_o}$	2.4×10^{12} /cm^2	2×10^{11} - 4×10^{12} /cm^2	[22], [102]
$\boldsymbol{\mu}$	451 cm^2/Vs	300 cm^2/V·s	[119]
$\mathbf{C_{EDL,EFF}}$	9.6 μF/cm^2	$\geq$ 3 μF/cm^2	[57], [64], [109]
$\mathbf{n^*}$	2.1×10^{12} /cm^2	2×10^{11} - 4×10^{12} /cm^2	[22], [102]
$\mathbf{R_C}$	11.5 kΩ μm	--	--

TABLE 2.2: SENSITIVITY ANALYSIS

Parameters	Extracted Values	Mean Error for 1.0*Parameter	Mean Error for 0.9*Parameter	Mean Error for 1.1*Parameter
$V_{GS,TOP}^0$	560 mV	1.22μA (2.06%)	10.1μA (12.3%)	9.84μA (13.6%)
n_o	2.4×10^{12} /cm^2	1.22μA (2.06%)	1.48μA (2.23%)	1.53μA (3.00%)
μ	451 cm^2/Vs	1.22μA (2.06%)	5.58μA (6.11%)	5.45μA (6.78%)
$C_{EDL,EFF}$	9.6 μF/cm^2	1.22μA (2.06%)	2.84μA (3.27%)	2.76μA (3.31%)
n^*	2.1×10^{12} /cm^2	1.22μA (2.06%)	1.26μA (2.12%)	1.21μA (2.07%)
R_C	11.5 kΩ μm	1.22μA (2.06%)	5.03μA (4.96%)	4.30μA (4.14%)

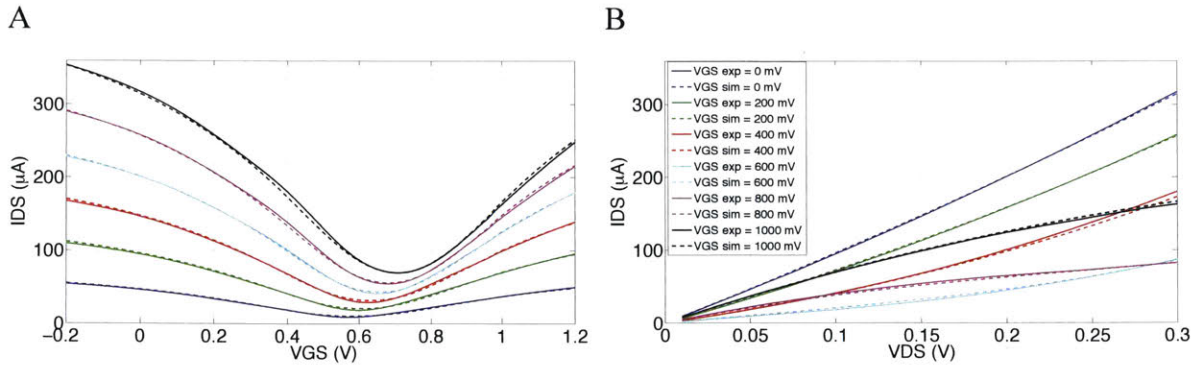

Figure 2.7: A) Experimental (solid) and simulated (dashed) current versus V_{GS} data. V_{DS} varies from 50 mV to 300 mV in increments of 50 mV. B) Experimental (solid) and simulated (dashed) current versus V_{DS} data. V_{GS} varies from 0 mV to 1000 mV in increments of 200 mV.

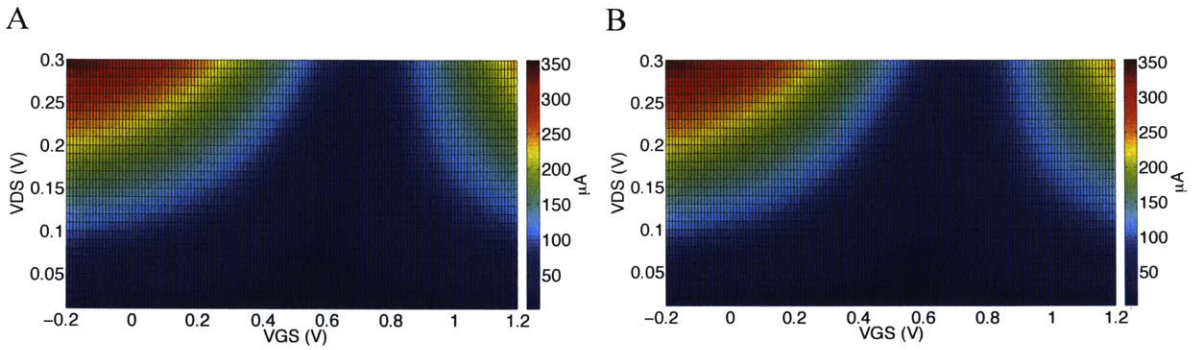

Figure 2.8: A) Experimental data for current as a function of V_{DS} and V_{GS}. B) Simulated data for current as a function of V_{DS} and V_{GS}.

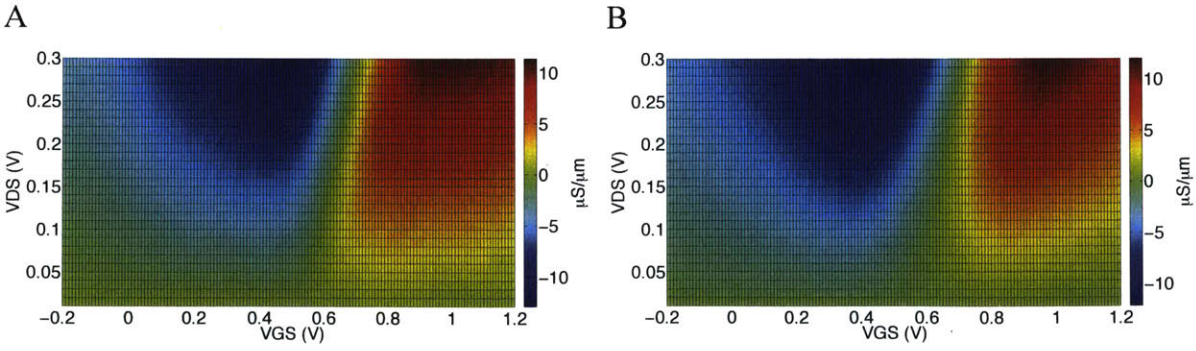

Figure 2.9: A) Experimental transconductance data as a function of V_{DS} and V_{GS}. B) Simulated transconductance as a function of V_{DS} and V_{GS}.

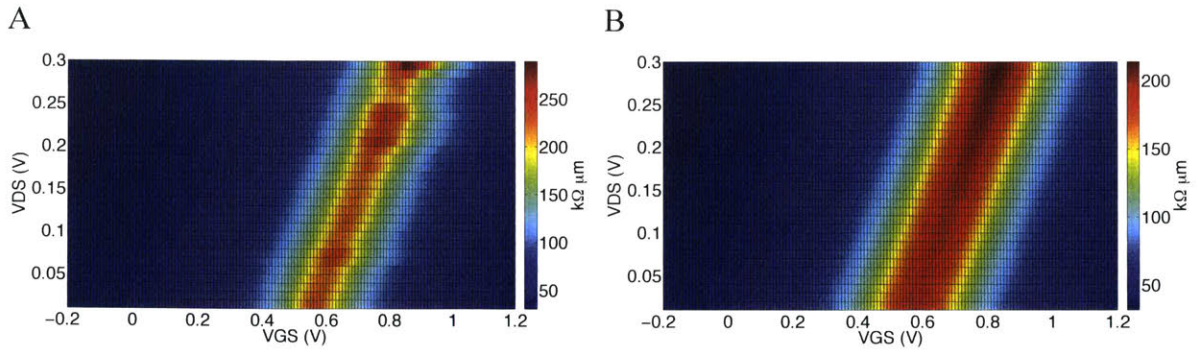

Figure 2.10: A) Experimental output impedance data as a function of V_{DS} and V_{GS}. B) Simulated output impedance as a function of V_{DS} and V_{GS}.

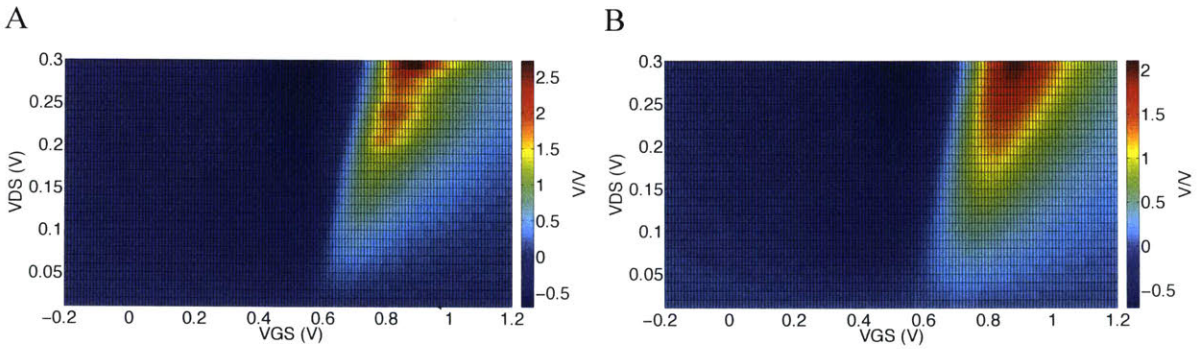

Figure 2.11: A) Experimental intrinsic gain data as a function of V_{DS} and V_{GS}. B) Simulated intrinsic gain as a function of V_{DS} and V_{GS}.

2.8 Performance Optimization

The graphene EGFET model (2.13) shows that increasing the degree of channel passivation increases the total series resistance. Large series resistance translates into diminished transconductance and decreased sensitivity. Optimal graphene EGFET designs should therefore eliminate the need for passivation in the channel region. Recessed channel passivation, however, directly exposes source and drain contacts to the electrolyte, which may result in large leakage currents. Excessive leakage current may be

avoided by minimizing the exposed area and using a source-drain metal such as platinum, which possesses wide electrochemical potential window in aqueous NaCl electrolytes as shown in **Figure 2.12**. Platinum's high chemical stability and biocompatibility also make it well suited for chemical and biological sensing applications.

Devices with and without partial channel passivation were fabricated on the same die and thoroughly compared in **Figures 2.13-2.19**. The electrolyte is 100 mM aqueous NaCl and the graphene EGFET channel dimensions are W/L = 40μm/30μm. Graphene EGFETs with recessed channel passivation were found to produce roughly four times higher transconductance as depicted in **Figure 2.15**. Experimental data shows devices with recessed passivation also may be biased over a wider range of V_{GS} values while still producing near-optimal transconductance. Output impedance data is provided in **Figure 2.17**. Devices with recessed channel passivation also produce higher intrinsic gain as shown in **Figure 2.18**. This stems from the reduced series resistance of devices with recessed passivation. The effect of series resistance on intrinsic gain is examined in detail in the subsequent section. As expected, gate leakage current increases with recessed channel passivation, but remains negligible in comparison to the channel current. Dependence of V_{DIRAC} on V_{DS} as described by (2.17) is verified in **Figure 2.19**.

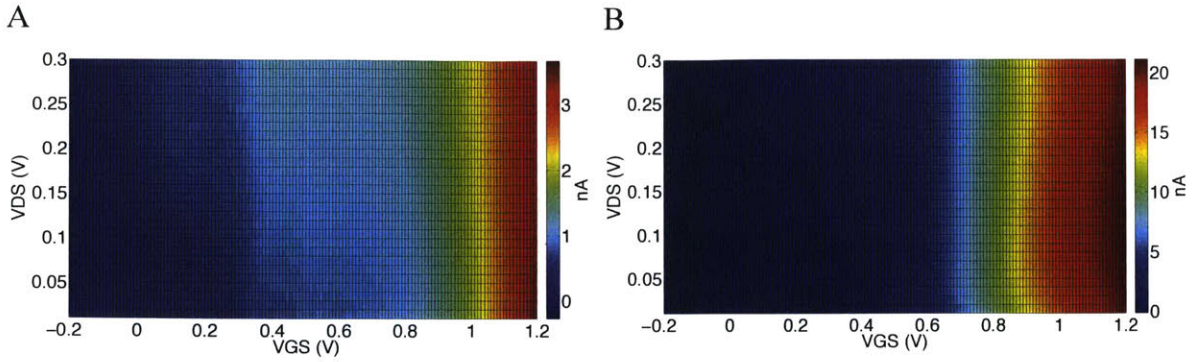

Figure 2.12: A) Gate leakage current as a function of V_{GS} and V_{DS} for a device with partial channel passivation. B) Gate leakage current as a function of V_{GS} and V_{DS} for a device with recessed passivation.

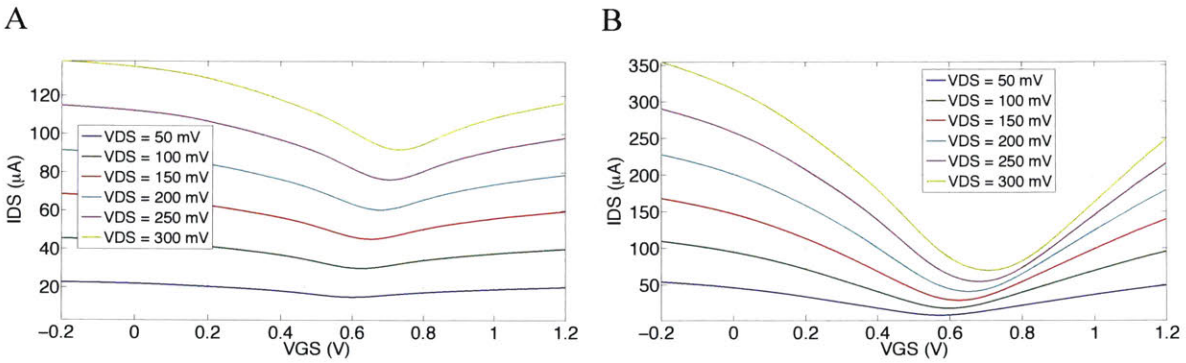

Figure 2.13: A) Current-voltage data for a device with partial channel passivation. B) Current-voltage data for a device with recessed passivation.

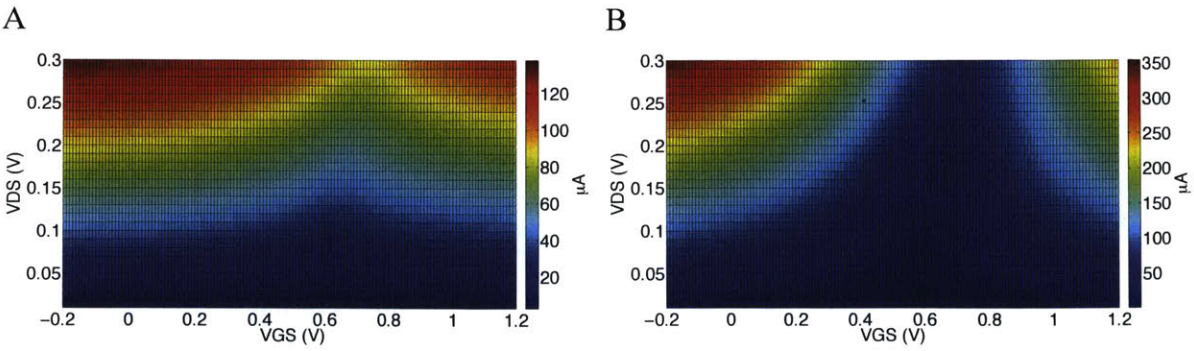

Figure 2.14: A) Channel current as a function of V_{GS} and V_{DS} for a device with partial channel passivation. B) Channel current as a function of V_{GS} and V_{DS} for a device with recessed passivation.

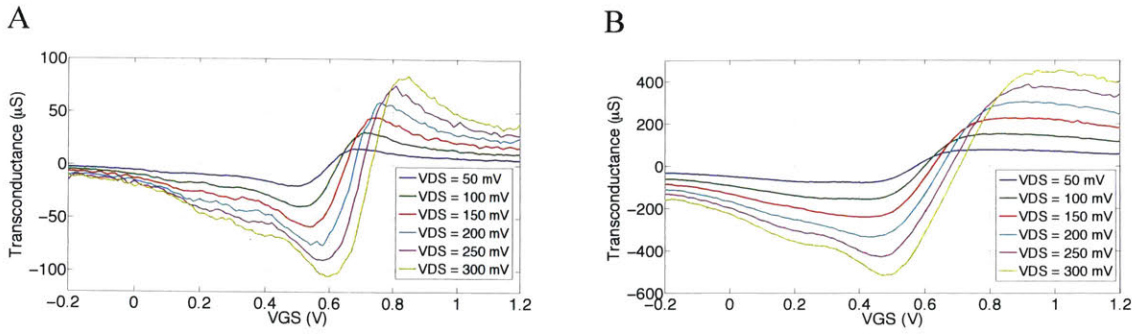

Figure 2.15: A) Transconductance versus V_{GS} for a device with partial channel passivation. B) Transconductance versus V_{GS} for a device with recessed passivation.

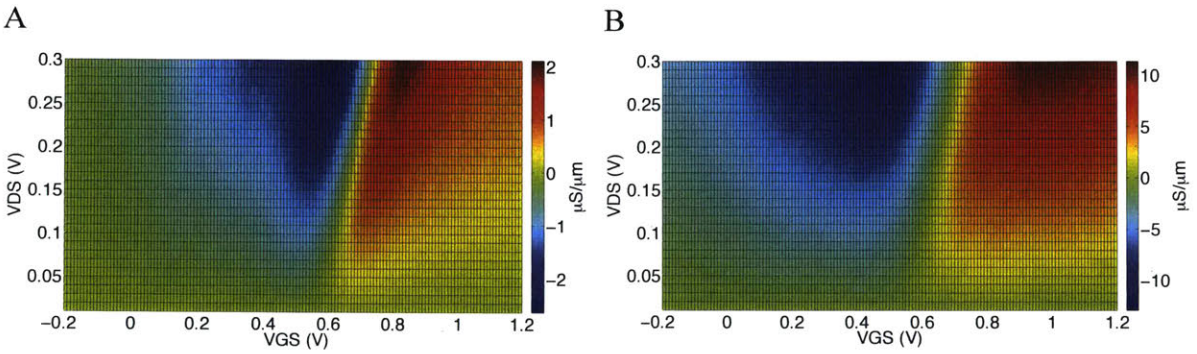

Figure 2.16: A) Transconductance as a function of V_{GS} and V_{DS} for a device with partial channel passivation. B) Transconductance as a function of V_{GS} and V_{DS} for a device with recessed passivation.

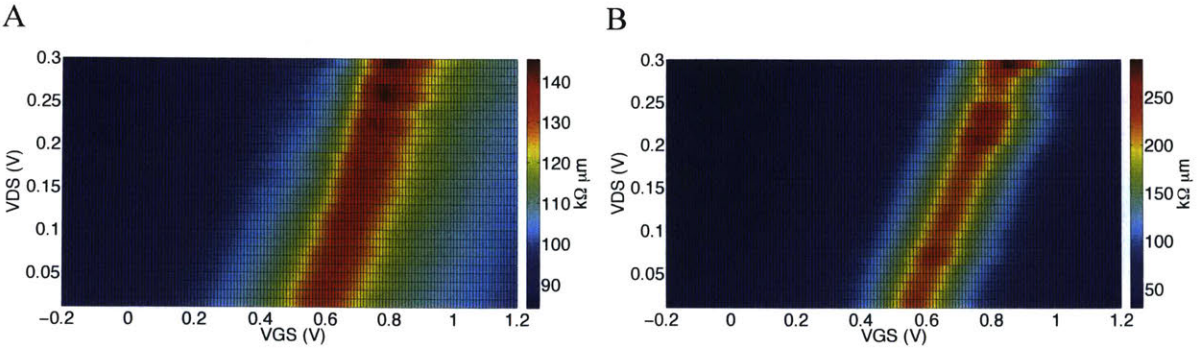

Figure 2.17: A) Output impedance as a function of V_{GS} and V_{DS} for a device with partial channel passivation. B) Output impedance as a function of V_{GS} and V_{DS} for a device with recessed passivation.

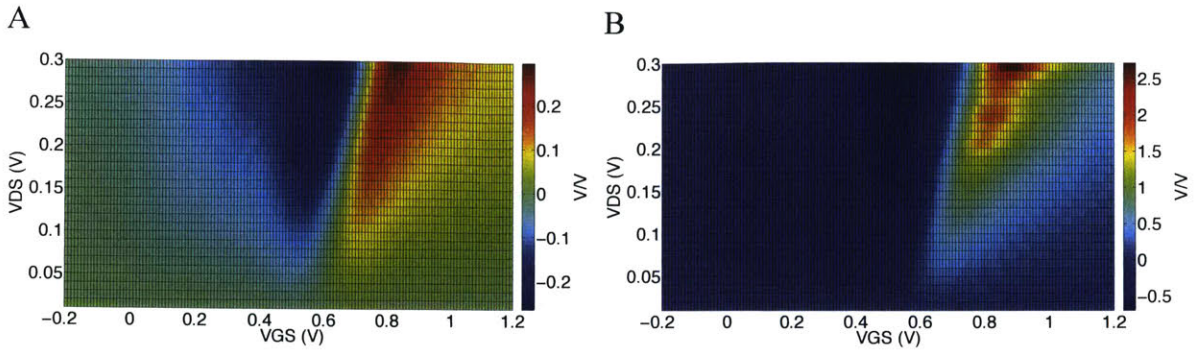

Figure 2.18: A) Intrinsic gain as a function of V_{GS} and V_{DS} for a device with partial channel passivation. B) Intrinsic gain as a function of V_{GS} and V_{DS} for a device with recessed passivation.

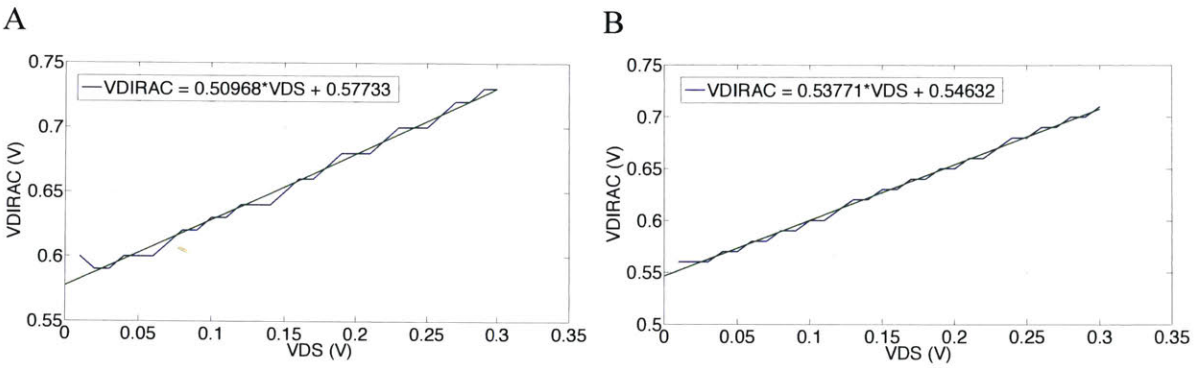

Figure 2.19: A) Dirac point as a function of V_{DS} for a device with partial channel passivation. B) Dirac point as a function of V_{DS} for a device with recessed passivation.

Graphene EGFET performance trends are investigated using the parameters extracted for our polyimide substrate process. Electrogenic cell sensing and more specifically neuronal action potential sensing is chosen as a specific application for device optimization. This sets the maximum channel width to 10 μm, which is roughly the diameter of a mouse hippocampal neuron. Channel widths greater than the neuron diameter result in only partial channel modulation and sub-optimal sensitivity. Channel current is then computed as a function of V_{GS} and V_{DS} while varying the channel length

by several orders of magnitude. Given a maximum V_{DS} of 1.0 V and V_{GS} range from -0.2 to 1.2 V, graphene EGFETs are shown capable of intrinsic gains of 9 V/V with a breakdown of transconductance and output impedance described in **Figure 2.20**.

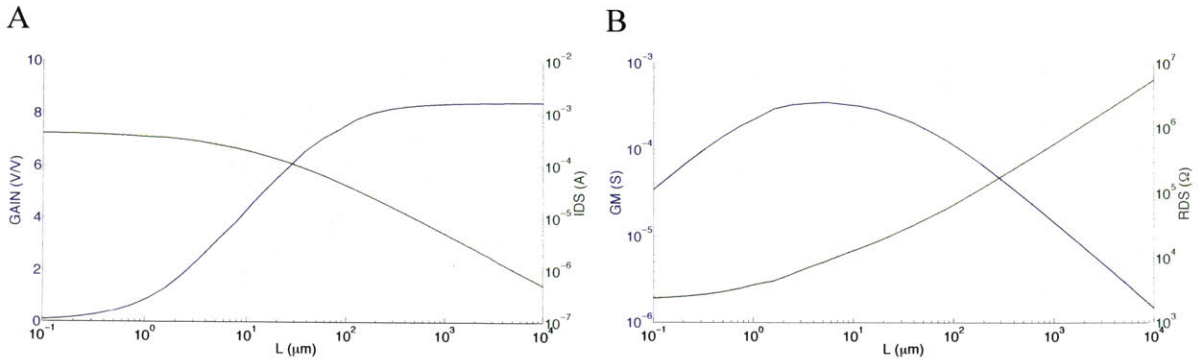

Figure 2.20: A) Simulated maximum intrinsic gain and current consumption versus channel length. B) Simulated transconductance and output impedance versus channel length.

The gain versus channel length plot depicts an important trait: graphene EGFET intrinsic gain is virtually independent of channel length. This behavior is apparent for larger channel lengths, where the effect of contact resistance is negligible. Intrinsic gain only begins to roll off at lower channel lengths because of decreasing transconductance due to contact resistance. This reduction in transconductance occurs because at short channel lengths, the contact resistance flattens out the current-voltage characteristic. With this understanding, the intrinsic gain curve can be shifted left to produce constant intrinsic gain across an even larger range of channel lengths by reducing contact resistance.

An alternative to maximizing the intrinsic gain is to focus on optimizing transconductance performance and matching graphene EGFETs with transresistance

amplifiers. **Figure 2.21** depicts the small-signal model for the two-stage amplifier circuit. The voltage gain for the circuit is given by (2.18)

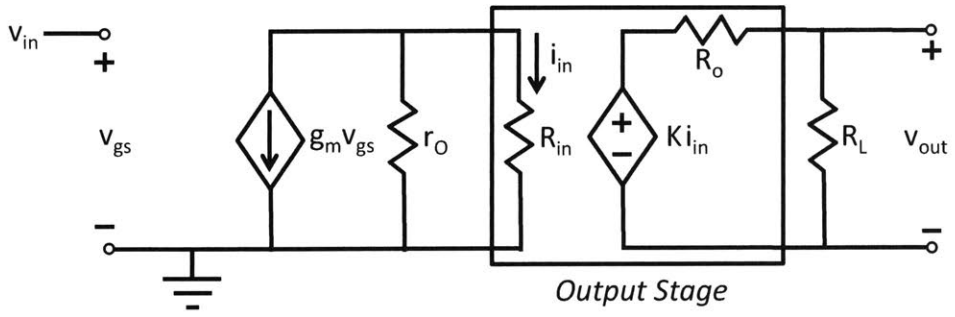

Figure 2.21: Graphene EGFET small-signal model with transresistance output amplifier stage.

$$G_v = \frac{v_{out}}{v_{in}} = -\left(g_m \frac{r_o}{r_o + R_{in}}\right)\left(K\frac{R_L}{R_L + R_o}\right) \tag{2.18}$$

where G_v is the overall voltage gain, v_{in} is the small signal gate voltage, v_{out} is the small signal output voltage, g_m is the graphene EGFET transconductance, r_o is the graphene EGFET output impedance, R_{in} is the input impedance of the second stage, K is the gain of the second stage, R_o is the output impedance of the second stage, and R_L is the load impedance. Given a fixed process technology, the most straightforward way to increase transconductance in graphene EGFETs is to increase the W/L ratio. For certain applications such as electrogenic cell sensing, the maximum width is dictated by cell diameter. The only means to optimize transconductance then becomes channel length reduction. As seen previously, this works to a limited extent. As the channel length becomes infinitesimal, the entirety of the drain-source voltage drops across the contact

resistances leaving no current to be modulated by the graphene region. **Figure 2.22** depicts transconductance behavior as a function of channel length along with the corresponding current consumption.

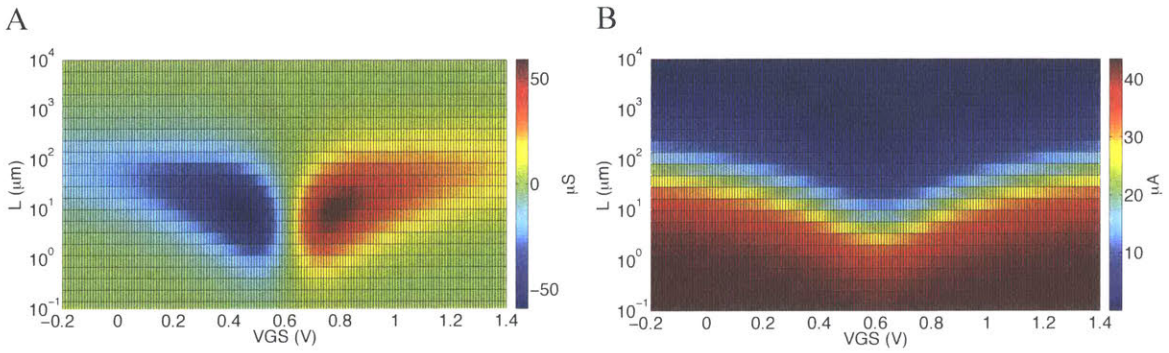

Figure 2.22: A) Simulated transconductance as a function of channel length for V_{DS} = 100 mV. B) Simulated current versus channel length for V_{DS} = 100 mV.

For the flexible polyimide substrate process and a set channel width of 10 μm, the optimal channel length is around 5 μm. This unintuitive and rather modest W/L ratio demonstrates the utility of graphene EGFET models in sensor design. **Figure 2.22** also reveals that slightly longer than optimal channel lengths provide transconductance performance over a broader V_{GS} range. Substantially shorter channel lengths, on the other hand, only serve to restrict the range of acceptable V_{GS} biases and increase power consumption.

Sensor designs focusing on high transconductance sensors coupled with transresistance amplifiers also require the input impedance of the second stage to be much less than the output impedance of the first stage. Using the developed model, the

graphene EGFET output impedance can be readily determined as shown in **Figure 2.23** enabling appropriate design of the second stage amplifier.

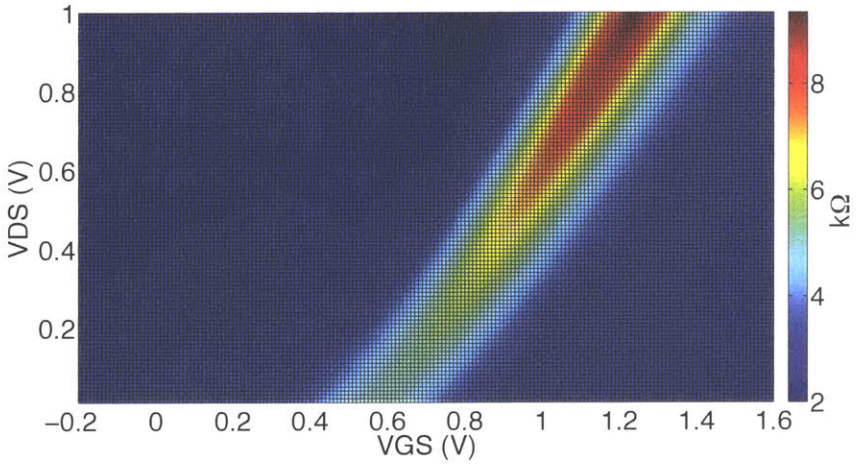

Figure 2.23: Output impedance as a function of V_{GS} and V_{DS} for a graphene EGFET with W/L = 10 μm / 5 μm.

2.9 A Compact Piecewise DC Graphene EGFET Model

The previous DC model for graphene EGFETs developed in has been shown capable of fitting experimental data with great accuracy. It solves for I_{DS} using a nested iterative process to compute the potential profile spatially along the graphene channel until the applied V_{DS}, V_{GS}, and I_{DS} are all in agreement. This iterative approach is highly accurate but computationally expensive and impractical when fitting to a large sample size of graphene EGFET *I-V* characteristics. Thus, developing a compact, yet accurate, DC model for graphene EGFETs is imperative. The previously developed model is provided in (2.19) as a reference and may be thought of, in some sense, as the basis for the derived compact model.

$$I_{DS} \approx \frac{\mu \frac{W}{L} \int_{I_{DS}R_C}^{V_{DS}-I_{DS}R_C} \sqrt{(qn_o)^2 + \left[C_{TOP}(V)[V_{GS} - V - V_o]\right]^2}\, dV}{1 + \left|\frac{\mu(V_{DS} - 2I_{DS}R_C)}{Lv_{sat}}\right|} \tag{2.19}$$

W is the channel width, L is the channel length, V is the potential along the channel, and v_{sat} is the saturation velocity. Equations detailing the voltage-dependent top-gate capacitance are not reproduced as our model will approximate $C_{TOP}(V)$ with a constant in order to reduce computational expense. As in the previous model, the compact model will also assume constant and equivalent electron and hole mobilities along with symmetric contact resistances.

Saturation velocity is safely neglected in the development of a compact model because graphene EGFETs are typically biased at low voltages to avoid undesirable oxidation-reduction reactions. Graphene quantum capacitance is neglected to produce a constant top-gate capacitance. The square root form of the integrand in (2.19) does not have a physical basis but serves to produce a nice rounding near the minimum carrier concentration in the previous model and to provide symmetry. The development of a compact model will instead assume an abrupt transition near the minimum carrier concentration, which has a stronger physical basis. This transforms (2.19) into a simpler albeit piecewise equation given by (2.20).

$$I_{DS} \approx k \begin{cases} \int_{V_{RC}}^{V_{DS}-V_{RC}} n_o' + C(V - V_X)\, dV & V_X \le V_{RC} \\ \int_{V_{RC}}^{V_X} n_o' + C(V_X - V)\, dV + \int_{V_X}^{V_{DS}-V_{RC}} n_o' + C(V_X - V)\, dV & V_{RC} < V_X < V_{DS} - V_{RC} \\ \int_{V_{RC}}^{V_{DS}-I_{DS}R_C} n_o' + C(V_X - V)\, dV & V_X \ge V_{DS} - V_{RC} \end{cases} \tag{2.20}$$

A number of variables have been combined and renamed due to space limitations. The new variables include $k = \mu W/L$, $C = C_{TOP}$, $V_X = V_{GS} - V_o$, $n'_o = qn_o$, and $V_{RC} = I_{DS}R_C$. I_{DS} remains present on both sides of the equation, but with a little manipulation, can be isolated to the left-hand-side. This results in the final compact piecewise DC model for graphene EGFETs given by (2.21)

$$I_{DS} \approx \begin{cases} \dfrac{kV_{DS}[C(\frac{V_{DS}}{2} - V_X) + n'_o]}{1 + 2kR_C[C(\frac{V_{DS}}{2} - V_X) + n'_o]} & \text{when } V_X < V_{RC} \\ \dfrac{1 + kR_C(CV_{DS} + 2n'_o) - \sqrt{[1 + kR_C(CV_{DS} + 2n'_o)]^2 - 4M[\frac{1}{2}kC[(V_{DS} - V_X)^2 + V_X^2] + kn'_oV_{DS}]}}{2M} & \text{when } V_{RC} \le V_X \le V_{DS} - V_{RC} \\ \dfrac{kV_{DS}[C(V_X - \frac{V_{DS}}{2}) + n'_o]}{1 + 2kR_C[C(V_X - \frac{V_{DS}}{2}) + n'_o]} & \text{when } V_X > V_{DS} - V_{RC} \end{cases} \quad (2.21)$$

where one new variable, $M = kCR_C^2$, is introduced due to space limitations. Although the model may appear daunting, it is in fact readily coded and computationally inexpensive. The three segments of the compact piecewise model correspond to scenarios in which the graphene channel is p-type, n-type, or a mixture of the two. **Figure 2.24** shows the derived compact piecewise model produces smooth and continuous transitions between each of the segments and ultimately yields graphene EGFET curves with all key features intact.

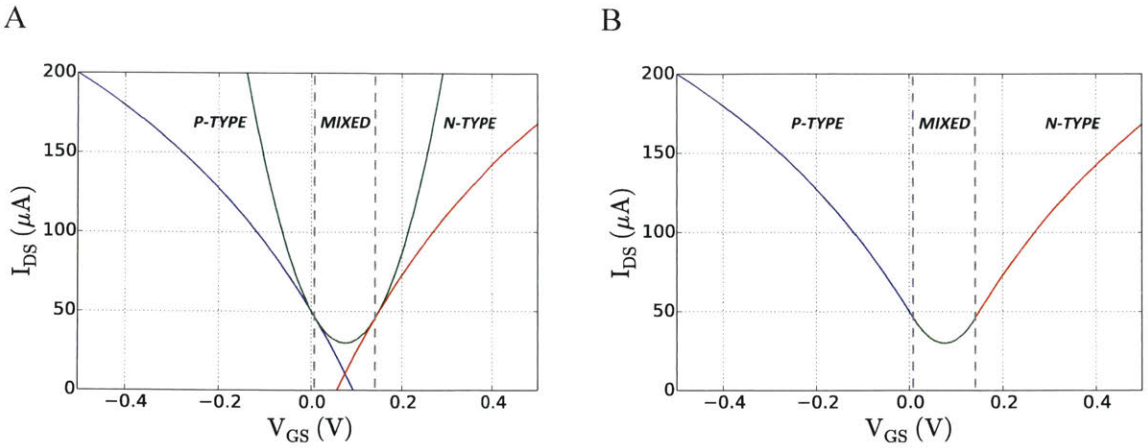

Figure 2.24: A) Plot showing the different segments of the piecewise model and their smooth and continuous intersections. B) Different domains of the piecewise model stitched together to yield the overall graphene EGFET I_{DS} vs. V_{GS} curve. Parameters are V_{DS} = 150 mV, W/L = 30 μm / 30 μm, μ = 450 cm^2 /Vs, C_{TOP} = 9.0 μF/cm^2, R_C = 5 kΩ μm, $n_o = 10^{12}$ /cm^2, and V_O = 0.0 V.

2.10 Summary

This work develops a highly accurate DC current–voltage model for graphene EGFETs. This was accomplished by combining models for dielectric-gated graphene FETs with models for the graphene electrolyte interface. The developed graphene EGFET model was shown capable of producing as little 2% error in the DC current–voltage characteristic. The model can then be used to compute other device characteristics required for circuit design such as transconductance, output impedance, and intrinsic gain. The model allows for heterogeneous top-gate capacitances, which enable the study of different passivation schemes and cases where the graphene channel is only partially modulated (e.g., partial coverage by an electrogenic cell). The developed model shows partial channel passivation acts to increase the overall series resistance. This was experimentally verified and graphene EGFETs with recessed passivation schemes and minimal leakage current were demonstrated.

Fitting the model to experimental data represents a convenient method to estimate device parameters such as minimum carrier concentration, mobility, contact resistance, effective double layer capacitance, and effective charged impurity concentration. This method allows graphene EGFET parameters to be estimated using a single measurement. The alternative requires fabricating specialized devices and a number of different measurements (e.g., Hall, TLM, Mott–Schottky).

Graphene EGFETs were shown capable of substantial intrinsic gains making them suitable for use in amplifier circuits. The intrinsic gain of graphene EGFETs is shown to be virtually independent of channel length provided the effect of contact resistance remains negligible. Alternatively, graphene EGFET sensors may be optimized for transconductance performance and coupled with transresistance amplifiers. A basis for determining an optimal channel length given certain design constraints is established. In addition, for instances in which it is desirable to fit a large sample size of *I-V* characteristics, this section develops a compact piecewise DC model for graphene EGFETs that is much less computationally expensive. Both graphene EGFET models may now be employed for application-specific sensor optimization and as a tool to inform the design of graphene sensors systems.

Chapter 3: AC Modeling of Graphene EGFETs

3.1 Introduction

This chapter advances graphene EGFET technology by developing a physics-based AC device model. Model development is used to develop an understanding of the small-signal frequency-dependent amplification characteristics, limitations, and tradeoffs for this new class of device. This chapter also demonstrates graphene EGFETs operating as functional amplifiers for the first time.

A number of models have been developed describing the DC behavior of graphene field-effect transistors (FETs) including two models accurately describing the DC characteristics of graphene electrolyte-gated field-effect transistors (EGFETs) [102]–[107]. Nothing to date, however, has been reported regarding the AC capabilities of graphene EGFETs. Accurate frequency response models are critical for the development of graphene EGFETs in applications such as electrophysiology. Previous works have shown graphene capable of providing low-noise signal transduction for neuronal action potentials [120]–[123]. These studies, however, employ graphene as an electrode or use graphene EGFETs merely for source-drain current modulation (i.e. as tunable resistors). As a result, these electrophysiology studies do not develop the ability of graphene to provide signal amplification at the sensor level.

Frequency response characterization of graphene EGFETs may prove useful for a number of other reasons. For instance, these devices may find use as high-speed chemical sensors in high-throughput microfluidics [43]. Frequency response characterization also potentially enables sensing technologies like electronic tongues—where changes in the frequency response (i.e. spectral content) may be analyzed to sense

changes in solution composition. This is closely related to spectroscopic and time constant techniques currently employed in electronic nose technologies [124]–[126]. Frequency response characterization of graphene EGFETs also plays a critical in avoiding aliasing when interfacing these sensors with analog-to-digital (ADC) converters in the development of practical sensor readout systems [127].

Graphene EGFETs are microfabricated to measure their intrinsic voltage gain, frequency response, and in order to develop the frequency-dependent small-signal model. The transfer function of the graphene EGFET model is found to contain an additional pole due to a unique resistive element stemming from electrolyte gating. Intrinsic voltage gain, cutoff frequency, and transition frequency for the microfabricated graphene EGFETs are approximately 3.1 V/V, 1.9 kHz, and 6.9 kHz, respectively.

3.2 Frequency-Dependent Small-Signal Model

The graphene EGFETs under study are three terminal devices possessing source, drain, and gate terminals. All voltages and currents are referenced with respect to the source terminal making V_{GS}, V_{DS}, I_{GS} and I_{DS} an exhaustive list of the voltages and currents of interest. Small signal intrinsic voltage gain is defined as $A_V = g_m r_o = \partial V_{DS}/\partial V_{GS}$, where g_m is the transconductance, which is defined as $\partial I_{DS}/\partial V_{GS}$, and r_o is the output impedance defined as $\partial V_{DS}/\partial I_{DS}$. Development of a frequency-dependent graphene EGFET small-signal model requires an accurate model for electrode-electrolyte interfaces. This is accomplished using a simplified Randles circuit as given by **Figure 3.1** [128], [129].

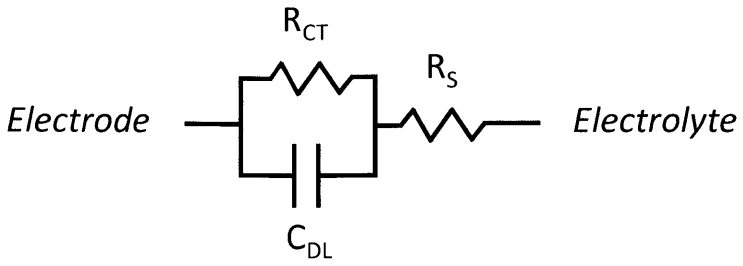

Figure 3.1: Schematic representation of the simplified Randles circuit commonly used to model electrode-electrolyte interfaces.

R_{CT} represents the charge transfer resistance, R_S is the solution resistance, and C_{DL} is the double layer capacitance. Electrode-electrolyte interfaces occur in three locations: the electrolyte-source interface, the electrolyte-drain interface, and at the reference electrode's interface with the electrolyte. The simplified Randles circuit is substituted into the small-signal model at each of these locations. Graphene is known to possess a wide electrochemical window in electrolytic environments [66]. This translates into a very high charge transfer resistance R_{CT} – roughly on the order of GΩ. Because of this, R_{CT} can be safely neglected at the gate-source and gate-drain terminals. This leads to the small-signal graphene EGFET model depicted in **Figure 3.2**.

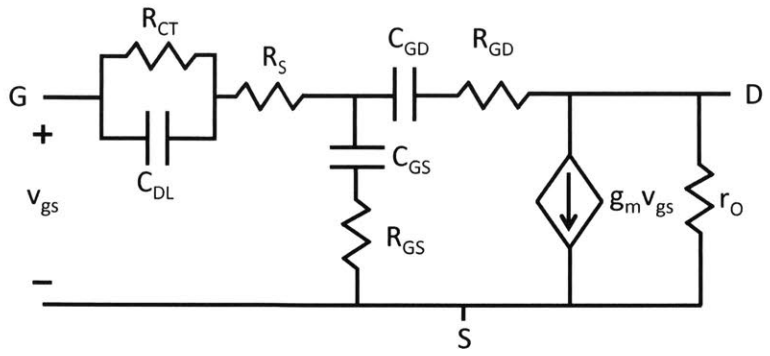

Figure 3.2: Graphene EGFET small-signal models depicting gate-source and drain-source capacitances and resistances using the simplified Randles circuit model.

Electrochemistry experiments possess two interfaces, only one of which is the focus of study. The first interface exists between the reference electrode and electrolyte, while the second interface occurs between the electrolyte and graphene EGFET. Reference electrodes are specifically designed to provide a stable reference potential and effectively translate changes in applied voltage entirely to the interface under study. This means the reference electrode effectively translates the entirety of the small signal voltage v_{gs} to the graphene EGFET and electrolyte interface. Because no series voltage drop occurs at the reference electrode, the simplified Randles circuit for the reference electrode may be neglected. Applying this fact in conjunction with the Miller theorem leads to the final small-signal model depicted in **Figure 3.3**.

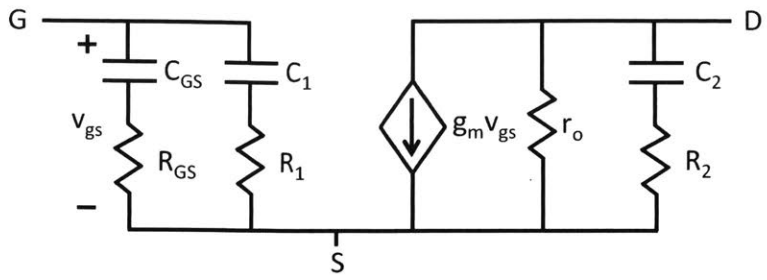

Figure 3.3: Final graphene EGFET small-signal model after application of the Miller theorem.

The small-signal model leads to a transfer function given by (3.4).

$$A_v(s) = -g_m r_o \frac{1 + sR_2C_2}{1 + s(R_2 + r_o)C_2} \tag{3.4}$$

It becomes evident that the graphene EGFET small-signal model, unlike a Si-MOSFETs, possesses a resistive component R_2 in series with the output parasitic capacitance. This unique component stems from the fact that graphene EGFETs are electrolyte-gated. Looking at the transfer function in the limits of low and high frequency operation produces the (3.5) and (3.6), respectively.

$$\lim_{s\to 0} A_v(s) = -g_m r_o \tag{3.5}$$

$$\lim_{s\to \infty} A_v(s) = -g_m r_o \frac{R_2}{R_2 + r_o} \tag{3.6}$$

R_1 and C_1 are given by equations (3.7) and (3.8). Because gain A_v is a negative

value, the absolute value of the gain $|A_v|$ is used for clarity in showing how the magnitude of parasitic impedances are amplified at the input.

$$R_1 = R_{GD}(1 + |A_v|) \tag{3.7}$$

$$C_1 = C_{GD}(1 + |A_v|) \tag{3.8}$$

Similarly, equivalent impedances at the output are slightly reduced and given by (3.9) and (3.10). This wholly details the development of the graphene EGFET small-signal model from first principles and provides the necessary reference equations describing individual model components.

$$R_2 = \frac{|A_v|}{1 + |A_v|} R_{GD} \tag{3.9}$$

$$C_2 = \frac{(1 + |A_v|)}{|A_v|} C_{GD} \tag{3.10}$$

3.3 Fabrication Process

Graphene EGFETs were fabricated on a piranha cleaned 4" thermally oxidized silicon wafer. Source and drain Ti/Au (10nm/150nm) contacts were patterned using lift-off photolithography. Monolayer graphene was then grown on copper foils using chemical vapor deposition (CVD) and transferred over the entire substrate [42]. The graphene channel regions were defined using MMA/SPR700 bilayer resist stacks and

helium and oxygen plasma at 16 sccm and 8 sccm, respectively. Bilayer photoresist stacks were removed using acetone and isopropanol. The entire wafer was passivated with approximately 0.6 μm of SU-8 2000.5 and windows were photo defined to provide electrolyte access to the graphene EGFET channel regions. The SU-8 was hard-baked at 150°C for five minutes to help remove cracks and pinholes. **Figure 3.4** depicts a graphene EGFET at various stages in the fabrication process. An aqueous electrolyte droplet of 100 mM NaCl was pipetted over the graphene EGFET channel regions and a reference electrode was inserted into the droplet to gate the devices. Aqueous 100 mM NaCl was chosen because of its charge symmetry and similarity to physiological osmolarity.

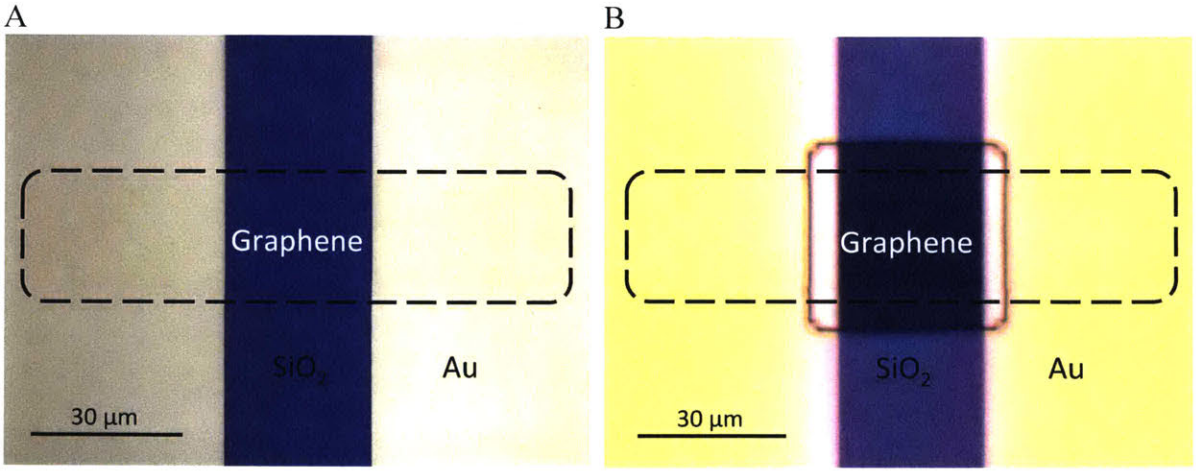

Figure 3.4: A) Mesa etched graphene after removal of the bilayer MMA/SPR700 resist stack and B) completely fabricated graphene EGFET with lead passivation using recessed SU-8 layer.

3.4 Experimental Setup

Two experimental setups were employed for graphene EGFET characterization: one for DC characterization and one for AC characterization. DC characterization was performed to measure the graphene EGFET drain-source current I_{DS} and a function of

V_{DS} and V_{GS}. This enables the calculation of transconductance, output impedance as well as intrinsic voltage gain. DC characterization also provides an independent means for measuring intrinsic voltage gain. In that way, DC and AC voltage gains can be compared and verified as consistent. AC characterization was performed by applying a small-signal voltage V_{GS} to a common-source graphene EGFET amplifier and measuring the resulting output voltage V_{DS} as a function of frequency.

The graphene EGFET experimental data is obtained from a device with dimensions W/L = 30 μm / 30 μm and recessed passivation such that approximately 10 μm of the drain and source contacts were exposed to electrolyte. The device was measured in 100 mM aqueous NaCl electrolyte. DC measurements employed a platinum wire pseudo reference electrode for convenience. AC measurements require the use of a Ag/AgCl reference electrode. All measurements are taken at room temperature under ambient conditions with normal ventilation. The volume of the electrolyte droplet was monitored throughout the experiment and did not decrease appreciably indicating constant electrolyte concentration over the course of measurements. **Figure 3.5** depicts graphene EGFET measurement setup.

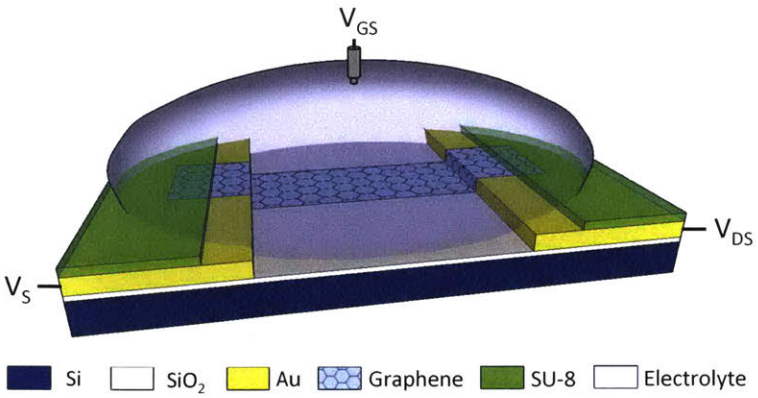

Figure 3.5: Graphene EGFET with recessed top-gate capacitance due to non-self-aligned source/drain passivation. The gate voltage is applied using a reference electrode.

3.5 DC Characterization

DC data was acquired by sweeping V_{GS} from -0.2 to 0.8 V and V_{DS} from 10 mV to 150 mV. The step size was 10 mV for both V_{GS} and V_{DS}. The V_{GS} step rate was 500 ms per 10 mV. A ten second hold time was allotted when resetting V_{GS} from 0.8 V to -0.2 V and incrementing V_{DS} by 10 mV. Further increasing the hold time and decreasing the sweep rate has little effect on the DC curves meaning sufficient time was given for the ions to redistribute at the graphene-electrolyte interface and for the electric double layer to reach steady state. Full DC characterization consists of over 1500 data points. A conventional representation of the graphene EGFET DC characteristic is presented in **Figure 3.6**.

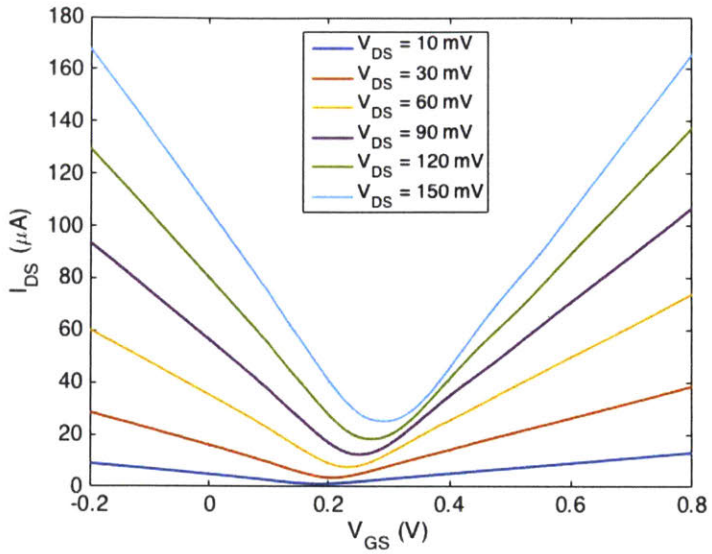

Figure 3.6: Graphene EGFET I_{DS} vs. V_{GS} for different applied V_{DS} values.

Intrinsic gain for the graphene EGFET was calculated by taking partial derivatives with respect to V_{GS} and V_{GS}. Recall that intrinsic gain $A_V = g_m r_o = \partial V_{DS}/\partial V_{GS}$, where g_m is $\partial I_{DS}/\partial V_{GS}$ and r_o is $\partial V_{DS}/\partial I_{DS}$. Partial derivatives of the graphene DC characteristic are calculated numerically using finite differences to produce **Figure 3.7**.

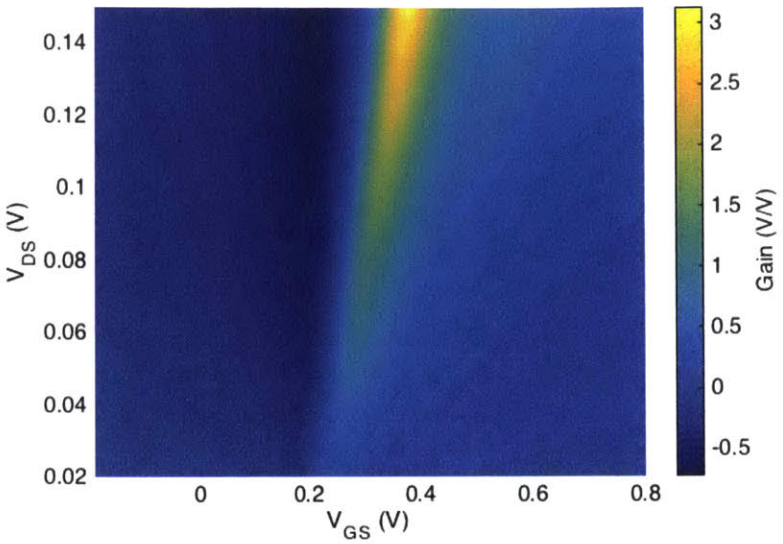

Figure 3.7: Intrinsic voltage gain as a function of V_{DS} and V_{GS} as calculated from DC characterization.

3.6 AC Characterization

The frequency response of graphene EGFETs was investigated using the common-source (CS) amplifier configuration. In this way graphene EGFET frequency response is investigated while simultaneously demonstrating a graphene EGFET as functional amplifiers for the first time. A 98.99 kΩ resistor was employed as the drain resistor R_D. The operating voltage V_{CC} was approximately 3.3 V and the drain of the graphene EGFET was biased at approximately 150 mV. Graphene EGFETs are not biased at high V_{DS} voltages to avoid undesirable redox reactions at the graphene-electrolyte interface and potential damage to the graphene channel. A small-signal 20 mVp-p sinusoid v_{in} was superimposed on a DC V_{GS} bias. The DC bias was then manually adjusted to maximize the output v_o and small-signal gain of the amplifier. The optimal V_{GS} bias was found to be to the right of the Dirac point on the graphene *I-V* curve, which is consistent with **Figure 3.7**. This indicates that the graphene EGFET

channel is n-type and that the transconductance is positive with respect to the orientation depicted in **Figure 3.3**. The frequency of the small-signal input voltage v_{in} was then swept from 10 Hz to 50 kHz in order to characterize the CS amplifier's frequency-dependent magnitude response. The CS amplifier transfer function closely resembles the transfer function of the intrinsic graphene EGFET derived in (3.4). The key exception is that the CS amplifier contains an additional drain resistor R_D at the output, which leads to the CS amplifier transfer function given by (3.11).

$$G_v(s) = -g_m(r_o//R_D)\frac{1 + sR_2C_2}{1 + s[R_2 + (r_o//R_D)]C_2} \tag{3.11}$$

The measured CS amplifier magnitude response was fit to the newly developed small-signal model for graphene EGFETs as shown by **Figure 3.8**. The CS amplifier reference schematic is provided as an inset for convenience. Fitting was achieved using bounded simulating annealing in conjunction with a least squares error function. Transconductance was estimated at 250 μS from the DC characterization data previously obtained for a V_{DS} operating bias of 150 mV. Small-signal model parameters r_o, R_2, and C_2 were extracted as 12.2 kΩ, 3.4 kΩ, and 5.7 nF, respectively. Experimental data verifies the presence of parasitic capacitance C_2, which is responsible for the roll-off in gain. The experimental magnitude response also verifies the presence of resistance R_2 at the output, a unique feature in graphene EGFETs stemming from electrolyte solution resistance R_S. Maximum gain, cutoff frequency, and transition frequency were found to be approximately 2.8 V/V, 2.0 kHz, and 7.8 kHz, respectively.

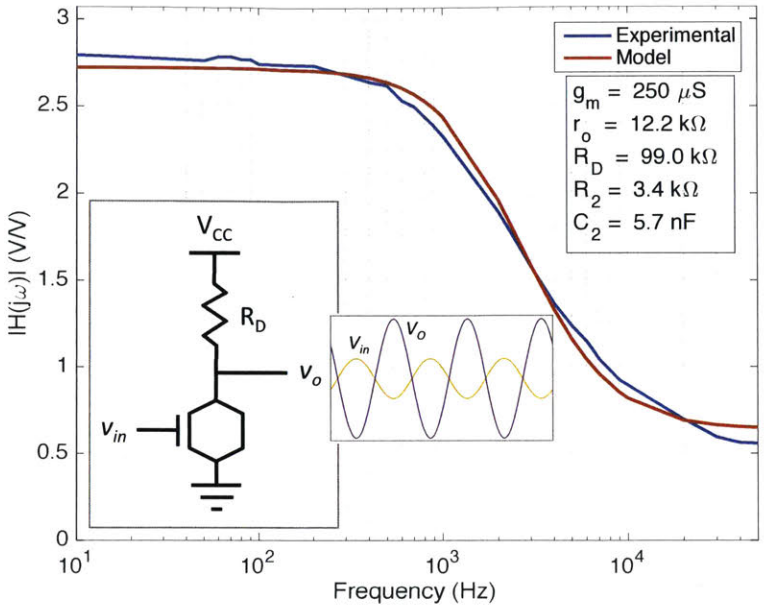

Figure 3.8: Fit of experimental graphene EGFET magnitude response with newly developed small-signal model for graphene EGFETs.

The intrinsic magnitude response of the graphene EGFET is readily computed due to its similarity to the CS amplifier magnitude response as seen from (3.4) and (3.11). Corresponding intrinsic phase response was computed using the extracted parameter values previously listed. A Bode plot for the intrinsic graphene EGFET magnitude and phase response is shown in **Figure 3.9**. The maximum intrinsic gain was found to be 3.1 V/V, the cutoff frequency was 1.9 kHz, and the transition frequency occurs at approximately 6.9 kHz. The corresponding equations for intrinsic graphene EGFET magnitude response and phase response are provided by (3.12) and (3.13).

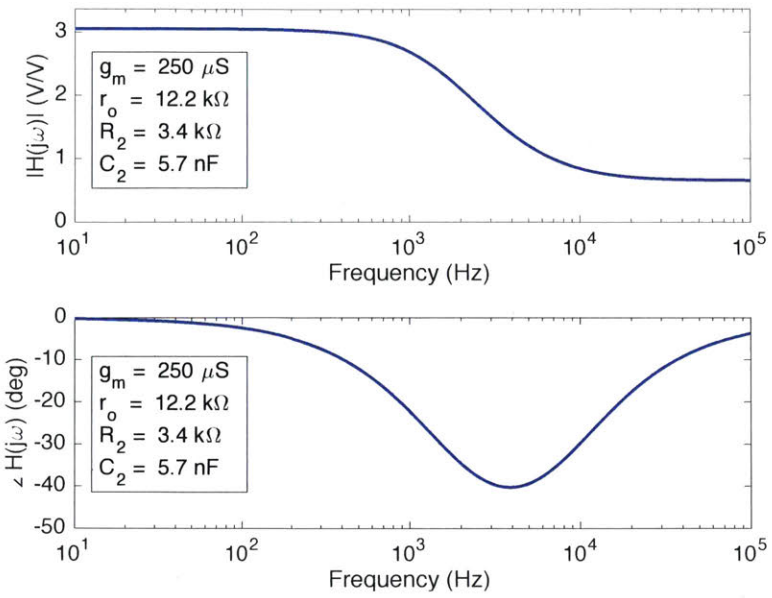

Figure 3.9: Bode plot depicting the intrinsic graphene EGFET magnitude and phase response.

$$\|A_v(j\omega)\| = g_m r_o \frac{\sqrt{1 + (\omega R_2 C_2)^2}}{\sqrt{1 + [\omega(R_2 + r_o)C_2]^2}} \tag{3.12}$$

$$\angle A_v(j\omega) = \frac{\tan^{-1}(\omega R_2 C_2)}{\tan^{-1}[\omega(R_2 + r_o)C_2]} \tag{3.13}$$

It is important to note that the CS amplifier small-signal equivalent circuit model neglects series resistance introduced by contact resistances. Previous work establishes the contact resistance at 6.3 kΩ · μm for this graphene EGFET microfabrication process, which translates to a small additional series resistances of approximately 200 Ω per contact [130]. Gated contact resistances are accurately approximated as linear over a small voltage range, which is precisely the case for the small-signal V_{GS} modulation of 20

mVp-p. Including contact resistance in the CS amplifier small-signal equivalent circuit model results in the DC gain described by (3.14).

$$\lim_{s\to 0} G_v(s) = -\frac{g_m R_D}{1 + g_m R_{C2} + \frac{R_{C1}}{r_o} + \frac{R_{C2}}{r_o} + \frac{R_D}{r_o}} \tag{14}$$

R_{C1} and R_{C2} represent the series resistances at the drain and source terminals, respectively. Because $g_m R_{C2} \ll 1$ and contact resistances R_{C1} and R_{C2} are much less than r_o, (3.14) reduces to the DC gain previously described in (3.11). Thus contact resistances may be safely neglected in small-signal circuit models used to calculate of amplifier gain and frequency response.

3.7 Performance Insights & Tradeoffs

Examination of parasitic capacitance C_2 provides further insight into the performance tradeoffs affecting graphene EGFET frequency response. Parasitic capacitance C_2 occurs between the drain and source. The extracted value of 5.7 nF for C_2 is too large to result from the graphene-electrolyte interface capacitance. Given the channel dimensions, the graphene-electrolyte interface contributes approximately 13.5 pF of parasitic gate-drain capacitance.

Figure 3.10A shows that the drain contact lead accounts for the majority of the parasitic capacitance C_2. Long contact leads are required to connect source and drain regions of the graphene EGFET, which are immersed in an electrolyte droplet, to dry contact pads that must be located further away (i.e. not submerged in electrolyte). A

capacitance of 5.2 nF was extracted using EIS for the drain contact lead. This value is roughly equivalent (and consistent) with the 5.7 nF value of C_2 extracted using the newly developed small-signal model. Thus, contact lead capacitance greatly hampers graphene EGFET frequency response and motivates the development of smaller area leads.

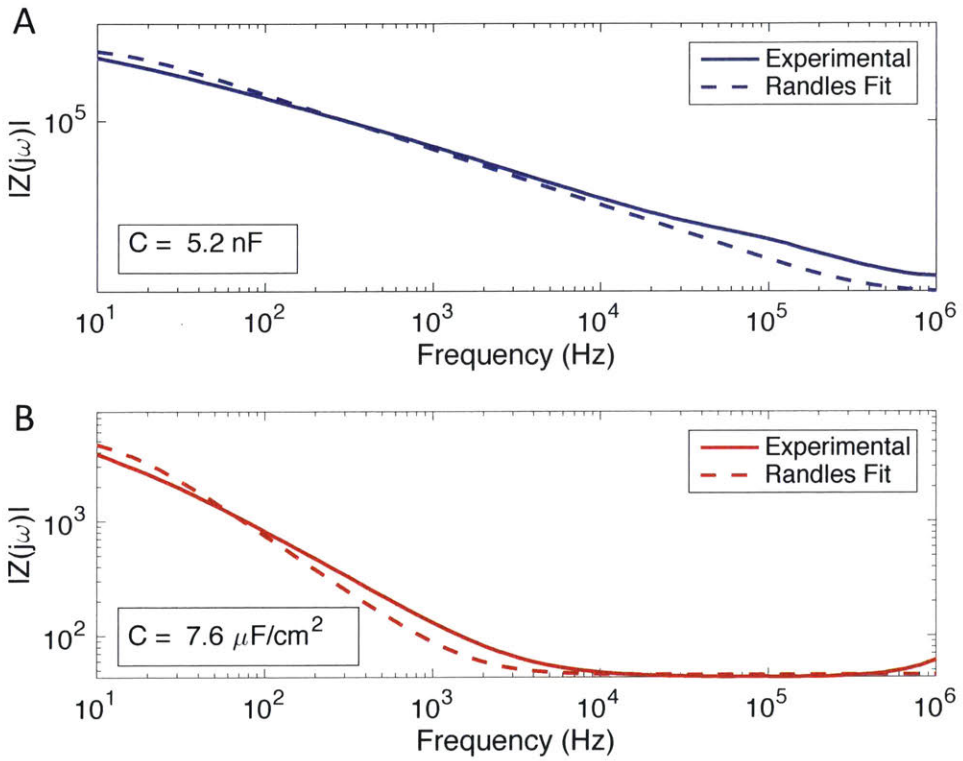

Figure 3.10: Electrochemical impedance spectroscopy (EIS) of A) the drain contact lead with the graphene channel removed and B) the Au-electrolyte interface capacitance. Measurements were taken in aqueous 100 mM NaCl.

Figure 10B shows the Au-electrolyte interface capacitance for the exposed metal of the drain region is approximately 7.6 μF/cm^2. This is roughly 150% larger than the graphene-electrolyte interface capacitance and contributes approximately 40 nF in parasitic capacitance given the dimensions of the exposed drain metal. This results in an

important tradeoff. Recessed channel passivation is known to reduce series resistance and enhance graphene EGFET transconductance performance. Recessed passivation, however, also introduces a parasitic capacitance substantially greater than that of the graphene-electrolyte interface. This motivates tighter misalignment constraints to reduce the metal exposure of the drain region. This finding also motivates development of self-aligned fabrication processes.

Lastly, attention should be drawn to the fact that R_2 introduces a pole in the graphene EGFET transfer function and ultimately controls the degree of gain degradation seen at high frequencies. R_2 stems from the solution resistance and therefore may be manipulated to a limited extent in many chemical and biological sensing applications. For instance, applications in which graphene EGFETs are employed as ion-selective chemical sensors (e.g. Na^+, K^+, Cl^-, Ca^{2+}) must necessarily vary ion concentrations and therefore solution resistance. Similarly, biological sensing applications provide little control over the cell medium composition and resulting solution resistance. This further motivates the reduction of parasitic capacitances, especially C_2 in order to enhance the frequency response of graphene EGFETs.

3.8 Summary

To the extent of our knowledge, this work develops the first small-signal frequency-dependent model for graphene electrolyte-gated field-effect transistors (EGFETs). This was accomplished by incorporating the Randles circuit into the small-signal field-effect transistor model. The newly developed small-signal model was shown capable of fitting experimental data exceptionally well. Extracted parameters from the

small-signal model were in good agreement with the parameters independently derived from DC characterization. Thus two separate methods were employed to extract parameters, both of which yielded similar results. The small-signal model shows that graphene EGFETs contain a unique additional resistive element in series with the parasitic output capacitance. This added resistive element adds a zero to the transfer function causing the graphene EGFET magnitude response to level off at high frequencies. The presence of this additional pole was experimentally verified. All of these reasons attest to the accuracy of the newly developed small-signal model for graphene EGFETs.

This work also employs graphene EGFETs as common-source amplifier configuration. To the extent of our knowledge, this work demonstrates for the first time, the ability of graphene EGFETs to function effectively as amplifiers providing a gain of 3 V/V. This concretely demonstrates the utility of graphene EGFETs as amplifiers for chemical and biological applications.

The majority of the parasitic drain-source capacitance C_2 was found to stem from the access lead for the drain. Contributions of the graphene-electrolyte interface and exposed metal drain contact are measured and compared as well. This reveals an important tradeoff in graphene EGFET design. Recessed channel passivation reduces parasitic series resistance and enhances graphene EGFET transconductance. However, recessed channel passivation also necessarily exposes some portion of the source and drain contacts. This increases parasitic capacitances and diminishes the operating frequencies for graphene EGFETs. This motivates the development of self-aligned microfabrication processes for high-performance graphene EGFETs.

This work provides a number of insights into the frequency-dependent small-signal behavior of graphene electrolyte-gated field-effect transistors (EGFETs). As such, it marks an important step in the development of graphene EGFETs for high-speed chemical and biological sensing applications.

Chapter 4: Graphene Sensor Systems

4.1 Introduction

This chapter transitions graphene EGFET technology from devices to the system level. A number of previous works explore the use of graphene as the channel material in electrolyte-gated field-effect transistors (EGFETs). These works include applications to chemical sensing, electrogenic cell sensing, and the development of electronic models [57], [58], [87], [110], [120], [121]. Sample size and yield, however, are always very limited – often limited to tens of devices at best. As a result, these works contain very limited statistical information regarding variation in electrical performance and typically do not present any information on the variation in underlying device parameters responsible for these electrical variations. A few previous works provide insight into graphene variation using Raman spectroscopy, scanning tunnelling microscopy, and THz time-domain spectroscopy [131]–[133]. For sensing applications involving graphene EGFETs, however, variation data obtained directly from measurements of actual graphene EGFETs is clearly the most relevant.

This chapter develops a novel graphene EGFET array architecture along with a compact, self-contained, and inexpensive measurement system that allows DC characterization of hundreds of graphene EGFETs as a function of V_{DS} and V_{GS} within a matter of minutes. This is achieved by developing a sensor array architecture capable of interrogating M x N devices using M + N wires. This specific implementation produces a sample size of 256 graphene EGFETs using a 16 x 16 array, which is accessed using 32 wires. This enables statistical analysis of graphene EGFET electrical performance parameters such as drain-source current, transconductance, output conductance, and

voltage gain for the first time. A reliable graphene electrolyte-gated field-effect transistor (EGFET) fabrication process is presented capable of producing 100% yield for a sample size of 256 devices. A new compact piecewise DC model for graphene EGFETs is developed and shown capable of fitting 87% of I_{DS} vs. V_{GS} curves with a mean percent error of 7% or less. The model is used to extract variations in device parameters such as mobility, contact resistance, minimum carrier concentration, and Dirac point. Correlations in variations are presented. Lastly, this chapter presents a framework for application-specific optimization of large-scale sensor designs based on graphene EGFETs.

4.2 Sensor System Design

The measurement system developed is depicted in **Figure 4.1A-B** and consists of a personal computer, microcontroller, custom-designed printed circuit board (PCB), and insertable graphene EGFET array chip. The personal computer primarily functions to record and process measured data and to program the microcontroller. The microcontroller supplies power to the PCB and provides digital control signals to manage row and column selection in the graphene EGFET array. The microcontroller is equipped with two 12-bit digital-to-analog (DAC) outputs that control the drain-source voltage V_{DS} and gate-source voltage V_{GS}.

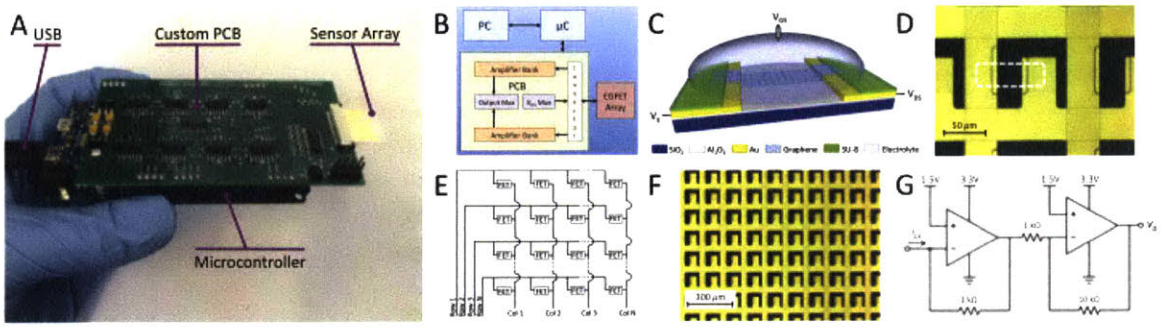

Figure 4.1: A) Complete measurement system and sensor array insert, B) system overview, C) graphene EGFET diagram, D) microscope image of graphene EGFET with channel region outlined in white (dashed), E) sensor array architecture, F) microscope image of graphene EGFET sensor array, G) transimpedance amplifier schematic.

The custom-designed PCB forwards the microcontroller-generated V_{DS} and V_{GS} biases to the appropriate graphene EGFET within the array. The V_{DS} bias is applied to the appropriate row via a 16-channel low-impedance analog multiplexer. The PCB then amplifies the resulting graphene EGFET I_{DS} currents across the entire row using a two-stage low-noise transimpedance amplifier (**Figure 4.1G**). The gains of the first and second stages are -1000 V/I and -10 V/V, respectively. Another 16-channel analog multiplexer performs column selection and forwards the amplified I_{DS} signal to the microcontroller.

The amplified I_{DS} signals are routed from the PCB to a 12-bit analog-to-digital converter (ADC) on the microcontroller. All data is transmitted back to the personal computer via USB. The benchtop system is capable of characterizing I_{DS} as a function of V_{DS} and V_{GS} for 256 graphene EGFETs within a matter of minutes. The measurement system also readily incorporates Ag/AgCl and saturated calomel reference electrodes for chemical and biological sensing applications requiring stable reference potentials.

4.3 Sensor Array Fabrication

Graphene EGFETs consist of a graphene channel between two conductive source-drain contacts, typically metals. A diagram of a graphene EGFET diagram and a microscope image of an actual device are depicted in **Figure 4.1C** and **4.1D**, respectively. The fabrication process begins with a No. 2 coverslip with dimensions 2.2 cm x 2.2 cm and 0.2 mm thickness. The coverslip is coated with 25 nm of Al_2O_3 using atomic layer deposition (ALD). This ensures excellent photoresist adhesion in the subsequent metal lift-off process used to form Ti/Au (10 nm / 150 nm) contact leads and array rows. Another 25 nm of Al_2O_3 is deposited as interlayer dielectric. BCl_3 plasma is used to etch windows into the interlayer dielectric to allow contact between first and second metal layers where appropriate. Array columns are formed by depositing a second layer of Ti/Au (10-nm/150-nm) using electron beam evaporation and lift-off photolithography.

Commercial graphene covered in poly methyl methacrylate (PMMA) from ACS Material is transferred over the array and nitrogen dried to remove any underlying water. The transferred graphene/PMMA film is baked for 15 minutes at 80°C and for two hours at 130°C. This allows the PMMA to reflow, which helps promote adhesion between the graphene and substrate. The sample is immersed in acetone for several hours to remove the PMMA. The sample is then annealed for three hours at 350°C in 700 sccm H_2 and 400 sccm Ar to reduce PMMA residue and to further promote adhesion between the graphene and the substrate. The graphene channel regions are defined using MMA/SPR3012 resist stacks and oxygen plasma etching. The sample is immersed in acetone for several hours to remove the resists. The sample is then coated with

approximately 2.4 μm of SU-8 2002. Windows are defined in the SU-8 over the graphene channel regions to allow electrolyte gating. The sample is baked at 150°C for five minutes to remove cracks in the SU-8 and enhance its chemical resistance. The sample is coated with PMMA to protect the graphene from particulates and high-pressure water during subsequent die sawing, which trims the coverslip to the appropriate size for the measurement setup. The sample is immersed in acetone for several hours to remove the protective PMMA layer.

The graphene EGFET array is designed as an insertable chip containing wire sharing to the extent possible while maintaining the ability to access individual devices. This allows M x N devices to be accessed using M + N wires. The design shown in **Figure 4.1E** is based on the fact the currents sum in parallel, which allows all output currents from a single column to be tied together as one output. Row multiplexing biases one device per column such that the entire output current for a given column stems from one device. Individual columns are replicated row-wise. The implementation of the arrayed structure is shown in **Figure 4.1F**.

4.5 Variation in Electrical Performance

Individual graphene EGFETs within the array were characterized using 100 mM aqueous NaCl as the electrolyte and a Au plated wire as a pseudoreference gate electrode. $\mathbf{V_{DS}}$ was swept from 10 mV to 150 mV in increments of 10 mV. $\mathbf{V_{GS}}$ was swept from -0.5 V to 0.7 V in increments of 10 mV with a sweep rate of 10 mV/s. A 30 s hold time was applied at the beginning of each $\mathbf{V_{GS}}$ sweep. This provides sufficient time for ion migration so the electrical double layer may reach steady state. A traditional

representation of the measured graphene EGFET *I-V* characteristics is presented in **Figure 4.2.**

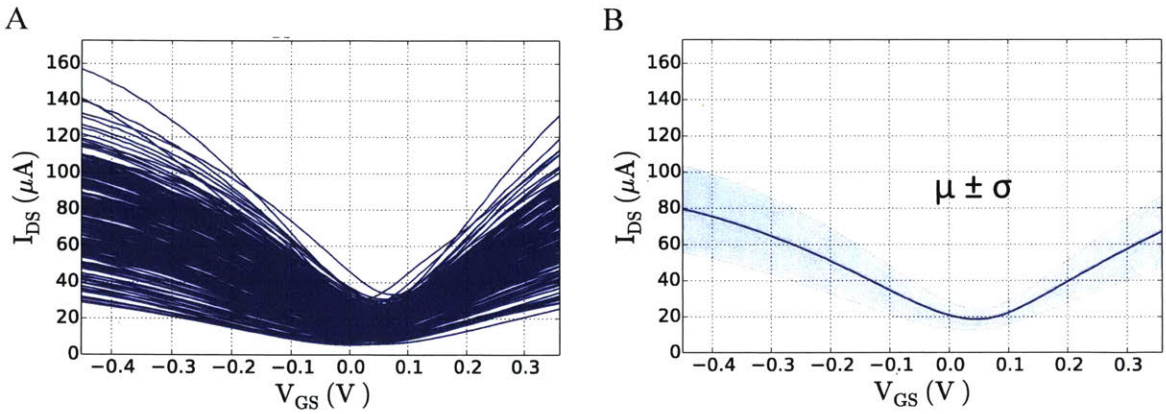

Figure 4.2: A) Individually measured graphene EGFET I_{DS} vs. V_{GS} curves, B) mean I_{DS} vs. V_{GS} (solid blue) plus or minus one standard deviation (shaded blue).

Plots of the acquired mean and standard deviation in $\mathbf{I_{DS}}$ vs. $\mathbf{V_{GS}}$ data are presented in **Figure 4.3**. Mean and standard deviation plots are provided for transconductance $\mathbf{g_m}$, output conductance $\mathbf{g_o}$, and intrinsic gain $\mathbf{G_V}$ in **Figures 4.4-4.6**, respectively. Transconductance $\mathbf{g_m}$ and output conductance $\mathbf{g_o}$ are defined as $\boldsymbol{\partial I_{DS}/\partial V_{GS}}$ and $\boldsymbol{\partial I_{DS}/\partial V_{DS}}$, respectively. Partial derivatives are calculated numerically using finite differences. Intrinsic voltage gain $\mathbf{G_V}$, also referred to simply as gain, is obtained by dividing the transconductance by output conductance.

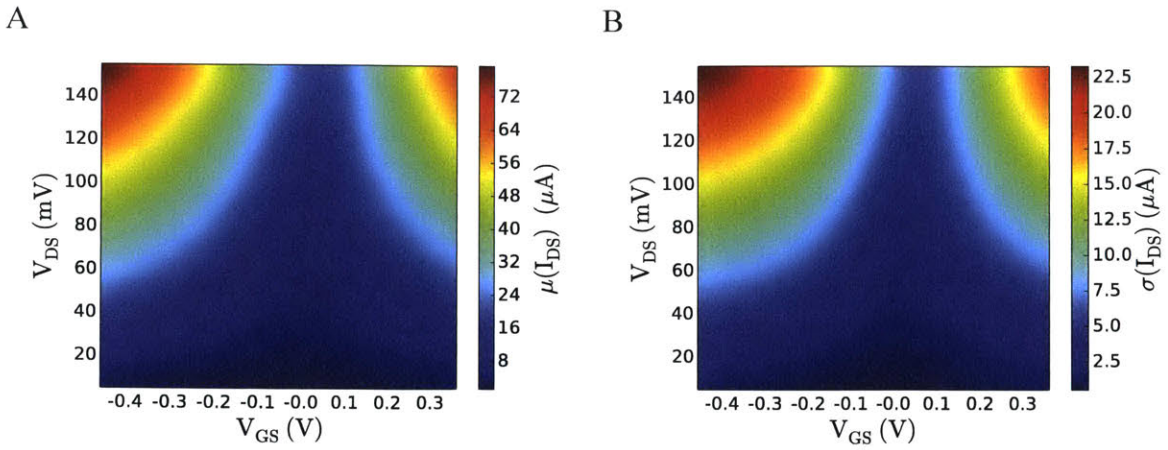

Figure 4.3: Experimentally derived A) mean source-drain current I_{DS} and B) standard deviation in source-drain current I_{DS}.

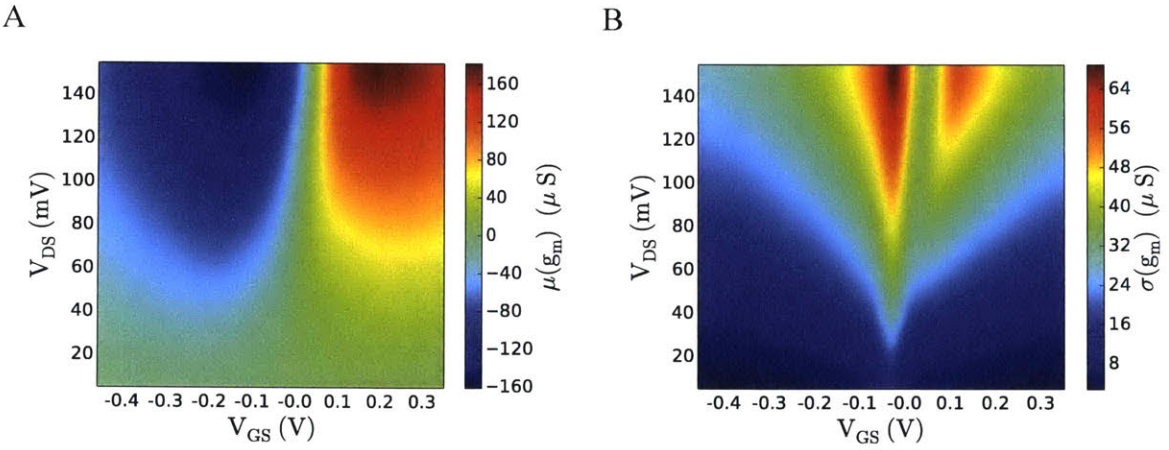

Figure 4.4: Experimentally derived A) mean transconductance g_m and B) standard deviation in transconductance g_m.

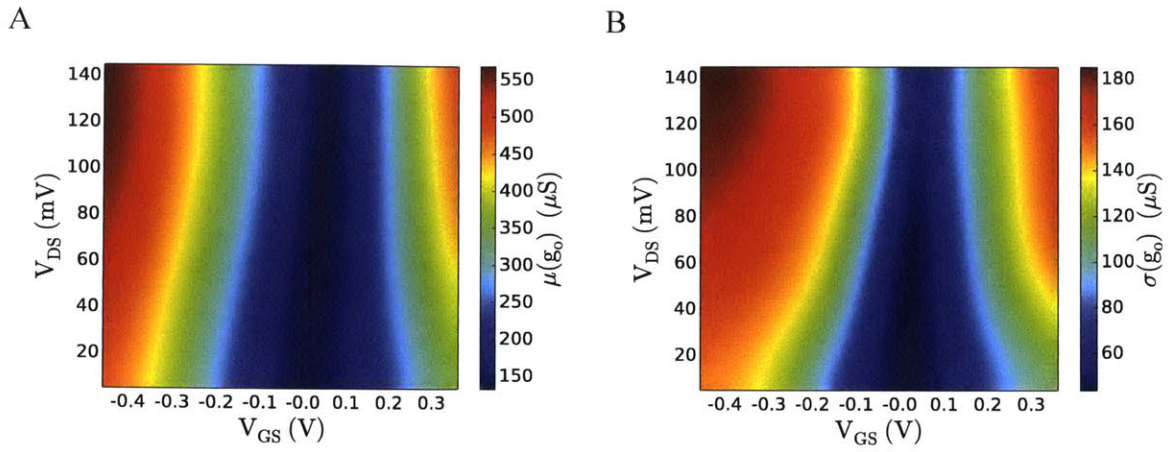

Figure 4.5: Experimentally derived A) mean output conductance g_o and B) standard deviation in output conductance g_o.

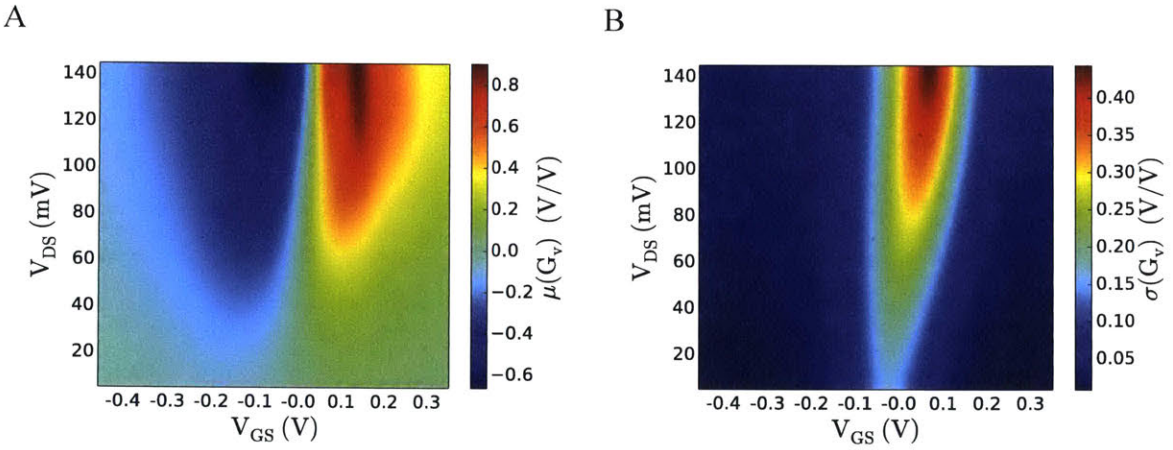

Figure 4.6: Experimentally derived A) mean intrinsic voltage gain G_V and B) standard deviation in intrinsic voltage gain G_V.

4.6 Graphene EGFET Parameter Variations

Variations in process-dependent parameters $\mu, R_C, n_o,$ and V_o are extracted using the compact piecewise DC graphene EGFET model developed in *Chapter 2*. The top-gate capacitance C_{Top} is approximated as a constant 3 $\mu F/cm^2$ based on electrochemical impedance spectroscopy (EIS) measurement of the graphene-electrolyte interface

capacitance. A number of previous works provide extensive examination of graphene's electric double layer and quantum capacitance [57], [64], [109], [134]. For $V_{DS} = 150$ mV, the mean percent error between model and experimental I_{DS} vs. V_{GS} curves was 7% or less for 87% of devices. Cases failing to meet this accuracy criterion were considered outliers and discarded. Because the model contains simplifying assumptions and inevitably fits experimental data with some degree of error, extracted device parameters and distributions represent approximations. This work, nonetheless, provides insight into parameter distributions for graphene EGFETs for the first time as shown in **Figure 4.7**.

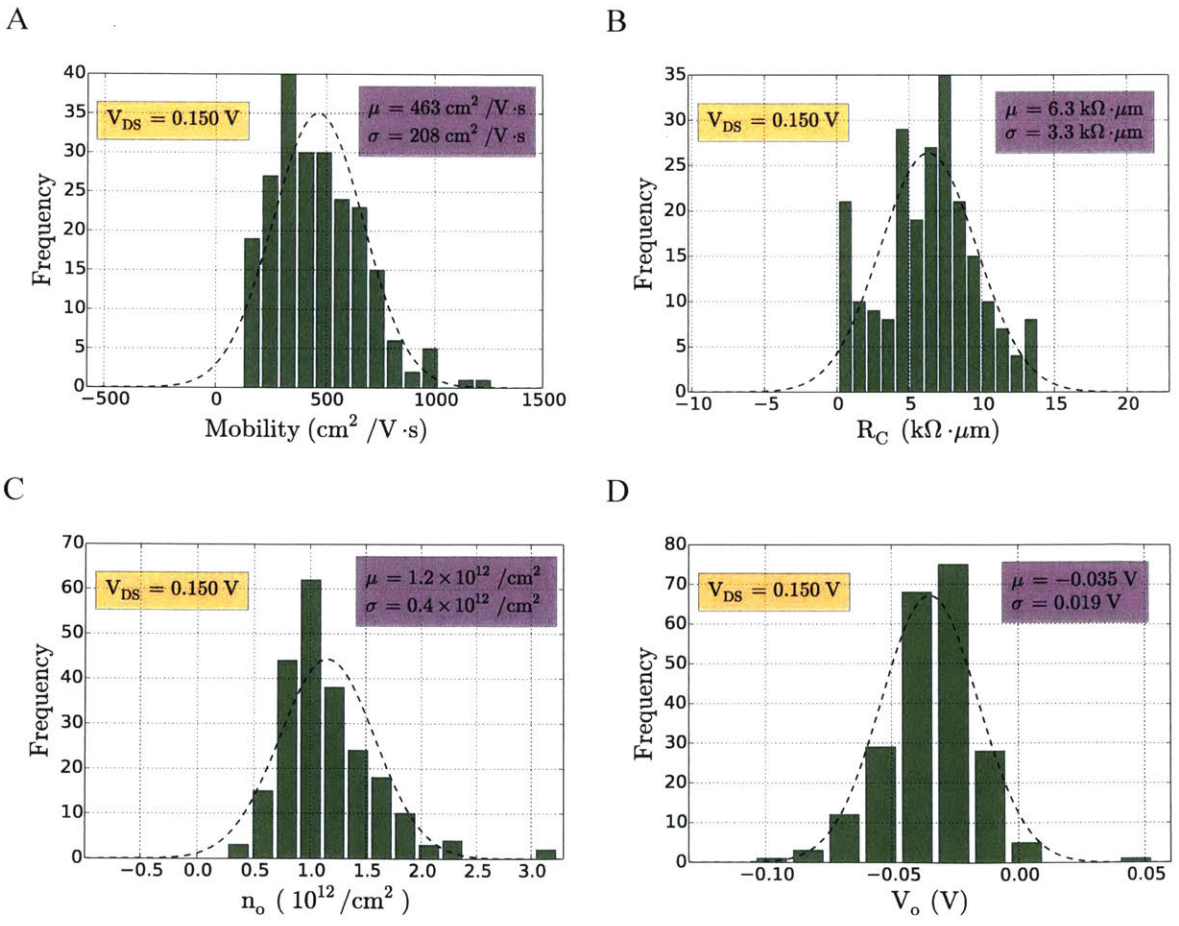

Figure 4.7: Extracted graphene EGFET distributions for A) mobility, B) contact resistance, C) minimum carrier concentration, and D) Dirac point.

Variations do not exhibit strong spatial trends (**Appendix A1.2**). The 100% yield is also indicative of excellent graphene transfer and a uniformly processed array. **Table 4.1** compares extracted parameter values with those previously reported in literature.

Table 4.1: Extracted Parameters

Parameter	Units	Mean	S.D.	Reported	References
μ	cm^2/Vs	463	208	300 – 451	[110], [119]
R_C	$k\Omega\ \mu m$	6.3	3.3	11.5	[110]
n_o	$10^{12}/cm^2$	1.2	0.4	0.2 – 4.0	[22], [102], [110]
V_o	mV	– 35	19	N/A	N/A

Correlation coefficients are computed to reveal relationships between parameter variations as shown in **Table 4.2**. Mobility and minimum carrier concentration are found inversely correlated [22]. Minimum carrier concentration was found correlated with the Dirac point and contact resistance was found correlated with both minimum carrier concentration and mobility.

Table 4.2: Process Parameter Correlation Coefficients

	μ	R_C	n_o	V_o
μ	1	0.53	-0.52	0.40
R_C	0.53	1	-0.55	0.15
n_o	-0.52	-0.55	1	0.14
V_o	0.40	0.15	0.14	1

4.7 Performance Optimization & Trade-offs

Before performing optimization, the impact of the input variables on the loss function should be studied. This is especially important for problems with a physical

basis such as graphene EGFET performance optimization. As an example of application-specific optimization, we have chosen the use of graphene EGFET arrays in a common-source amplifier configuration for the monitoring of electrogenic cells such as neurons or cardiac cells. In this application, we primarily wish to optimize the voltage gain. By investigating how the design parameters (V_{DS}, V_{GS}, W, L) and process-dependent parameters (μ, C_{TOP}, R_C, n_o, V_O) affect gain, we can develop some intuition regarding performance.

We investigate trends in gain performance by strategically modifying the design parameters and process-dependent parameters. At most, we may visualize three-dimensional data. For this reason, only two input parameters are varied at a time while all remaining parameters are fixed to some baseline value. Baseline parameter values are set based on the values extracted from our fabrication process as detailed in **Table 4.3**. Note that V_{GS} has no single baseline value. This is because gain is calculated across a V_{GS} range of ±1V. The reported "gain" values depicted in **Figures 4.9-4.12** are in fact the maximum attainable gain given that the designer is free to manipulate V_{GS} to any value within ±1V in order to maximize the gain. This allows gain to be plotted as a function of two variables without continually sacrificing one dimension to V_{GS}. A V_{GS} range of ±1V is chosen because it is approximately the range of the graphene's electrochemical potential window in phosphate buffered saline [66]. Outside of this range, substantial oxidation-reduction reactions occur which may damage the graphene or alter its electrical properties.

Table 4.3: Baseline Input Parameters

Parameter	Units	Value
V_{DS}	mV	200
V_{GS}	mV	N/A
W	μm	30
L	μm	30
μ	cm^2/Vs	463
C_{Top}	$\mu F/cm^2$	3.0
R_C	kΩ μm	6.3
n_o	$10^{12}/cm^2$	1.2
V_o	mV	−35

The V_{DS} bias is limited to a maximum value of 200 mV to ensure I_{DS} values generated by the model for short channel lengths are sustainable in actual graphene EGFETs. Limiting V_{DS} also avoids model inaccuracies due to velocity saturation.

Figure 4.8A shows the optimal V_{GS} does not vary significantly with changing channel length. **Figure 4.8B** shows that the gain is also virtually independent on channel width provided that all other parameters remain constant. This is because increasing the channel width increases the transconductance and output conductance equally, leaving the overall gain unaffected. This suggests we may be able to reduce the optimization parameter space by eliminating the need to optimize the channel width. Gain also falls off as channel length is reduced. This is because at shorter channel lengths, contact resistance has a more pronounced effect on the transconductance while keeping the output conductance relatively constant because it is dominated by the graphene. **Figure 4.9A** shows that if an application requires higher gain, one can simply increase the V_{DS} bias.

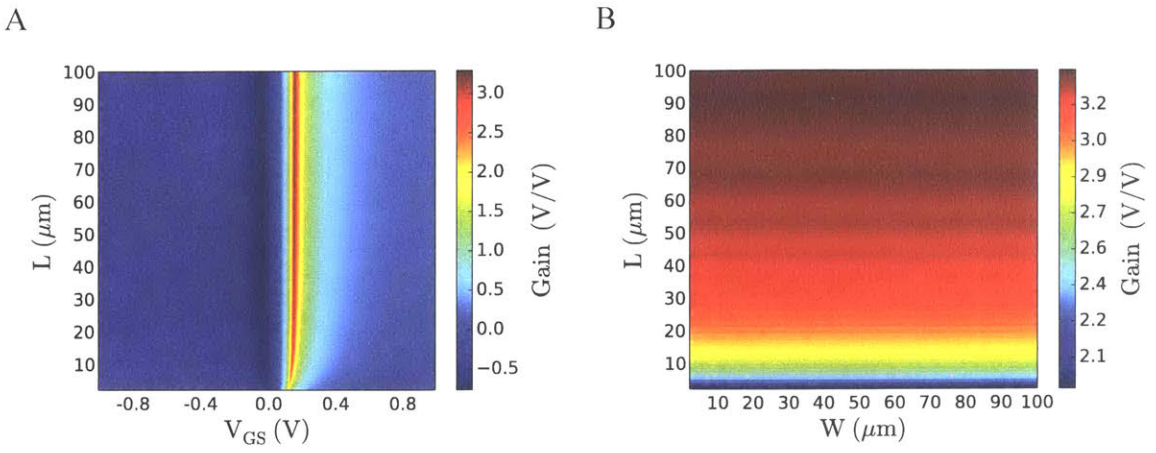

Figure 4.8: Model derived trends for intrinsic voltage gain as a function of A) V_{GS} and L, and B) W and L.

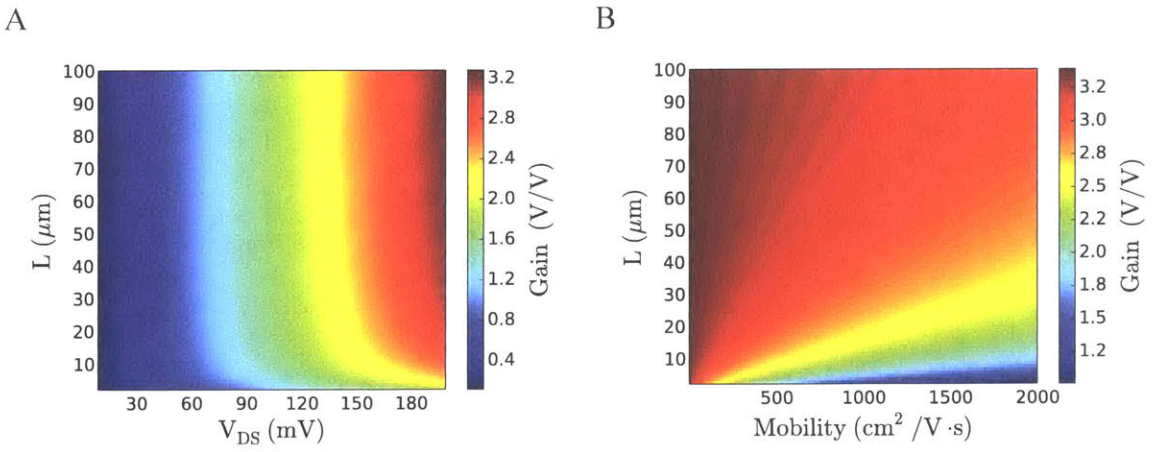

Figure 4.9: Model derived trends for intrinsic voltage gain as a function of A) V_{DS} and L, and B) mobility and L.

Now that we have investigated the effects of design parameters on the intrinsic voltage gain, we turn to analyzing the process-dependent parameters. As the name indicates, these parameters are largely dependent on fabrication processes and more difficult for a designer to control. In some cases, however, it may be worthwhile to modify the fabrication process or perform some post-fabrication treatment of devices in order to achieve better performance.

Figure 4.9B shows that increasing mobility reduces gain provided all other parameters are held constant. This stems from the fact that increasing mobility increases output conductance to a greater extent than transconductance. This effect becomes more pronounced at short channel lengths where contact resistance has a greater effect. Another interpretation is that high mobility increases the importance of having low contact resistance. It is important to note that it may not be possible to increase mobility to the extent simulated while keeping all other parameters constant as is assumed. For instance, higher mobilities are likely accompanied by lower values in minimum carrier concentration n_0, which is also supported by our correlation data in **Table 4.2**. Decreasing n_0 has its own affect on gain. In any event, increasing mobility by a reasonable few hundred cm^2/Vs does not greatly diminish gain except at very short channel lengths where contact resistance plays a greater role.

Increasing the top-gate capacitance is found to produce higher gain as shown in **Figure 4.10A.** Larger top-gate capacitances more effectively translate V_{GS} signals into the graphene channel. In practice, however, the top-gate capacitance is limited by graphene's quantum capacitance and hydrophobicity [57], [110]–[112]. Nonetheless, it becomes desirable to perform measurements in electrolytes that maximize the top-gate capacitance to the extent possible.

Lower contact resistances are found to produce higher gain provided all other parameters are fixed. This is shown in **Figure 4.10B**. Lower contact resistances produce higher transconductances while having little effect on the output conductance, which is mostly determined by the graphene channel. This effect becomes more pronounced at small channel lengths where contact resistance has a greater effect on performance.

Because contact resistance is a parasitic provides absolutely no benefit, it should be minimized.

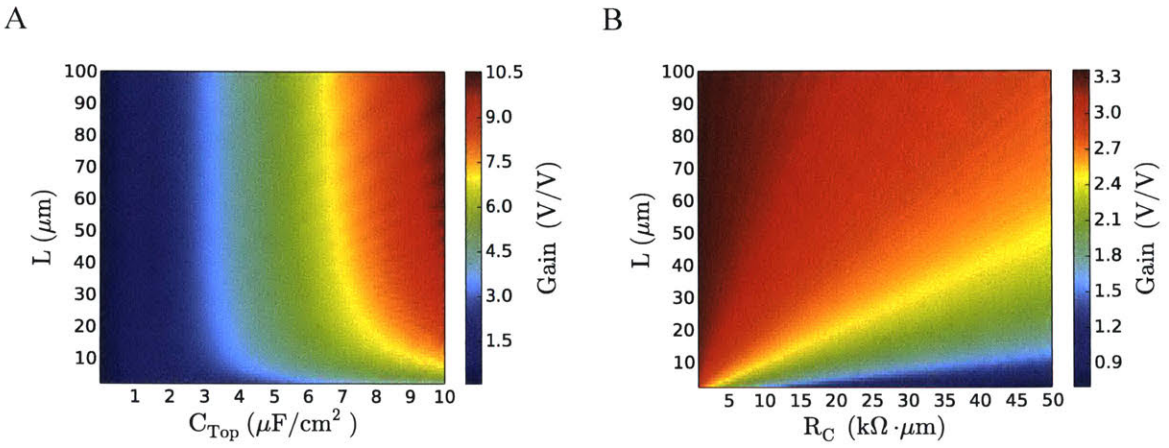

Figure 4.10: Model derived trends for intrinsic voltage gain as a function of A) C_{Top} and L, and B) R_C and L.

Figure 4.11A shows that decreasing n_o increases gain. Decreasing n_o likely has little effect on the transconductance. It does, however, lower the output conductance, especially in the region around the minimum conduction point on the I_{DS} vs. V_{GS} curve. This is the region where the maximum gain is typically found. Ultimately, decreasing n_o decreases g_o while keeping g_m relatively constant, leading to increased gain. **Figure 4.11B** shows that the optimal gain is not affected by the location of the Dirac point because the V_{GS} bias can be tune accordingly.

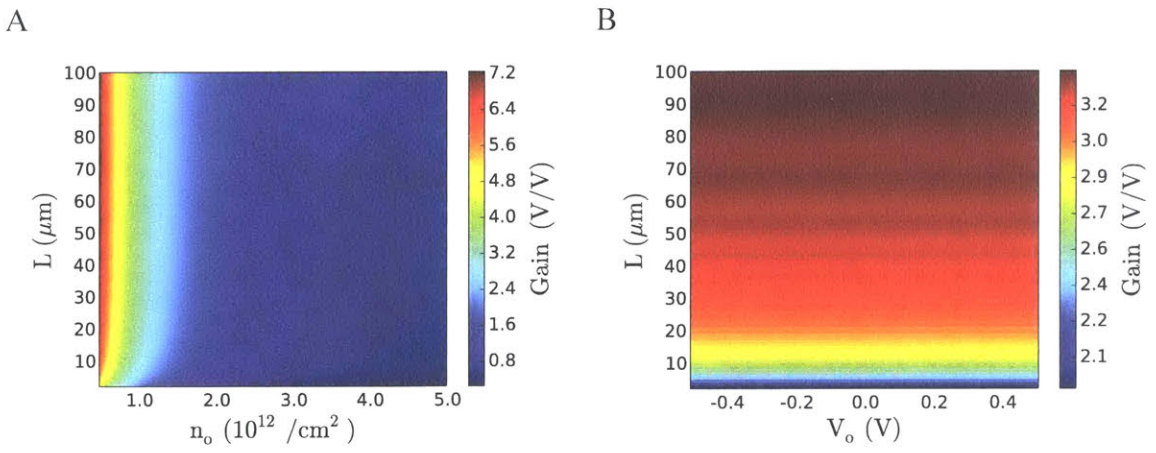

Figure 4.11: Model derived trends for intrinsic voltage gain as a function of A) n_0 and L, and H) V_O and L.

Gain was found to increase with channel length in every case. General trends for optimizing gain in graphene EGFETs are summarized in **Table 4.4**.

Table 4.4: Gain Optimizing Parameter Trends

Parameter	V_{DS}	V_{GS}	W	L	μ	C_{TOI}	R_C	n_o	V_o
Desired	↑	N/A	↕	↑	↓*	↑	↓	↓	↕

*Counterintuitive result

Now that some intuition exists regarding gain performance of graphene EGFETs, it is possible to move on to a more thorough procedure for optimizing gain performance. Instead of optimizing purely for gain, it is possible to include penalties for variability in gain as well as increases in device area, noise, and power consumption. Minimizing variability in gain performance is especially important for applications where all devices are gated using a common V_{GS}. Equation (4.1) describes the objective function including these penalty terms. The fact that gain is a function of design and process parameters is omitted for readability. Equation (4.1) also assumes the likely scenario in which the

designer is free to manipulate the design parameters but has no control over the process-dependent parameters.

$$H(V_{DS}, V_{GS}, W, L) = \mu(\text{Gain}) + k_1\sigma(\text{Gain}) + k_2 WL + k_3 I_{DS} \quad (4.1)$$

Here $\boldsymbol{\mu(\text{Gain})}$ and $\boldsymbol{\sigma(\text{Gain})}$ are the mean and standard deviation of the intrinsic voltage gain, respectively. Constants $\mathbf{k_1}$, $\mathbf{k_2}$, and $\mathbf{k_3}$ should be negative values because increases in variation, area, noise, and power consumption are typically undesirable. Optimization algorithms are typically designed to minimize a loss function. Equation (4.1) may be transformed into the appropriate loss function by taking the negative logarithm. The standard deviation in gain term may be approximated using a multivariate normal distribution in conjunction with the parameter variation data and covariance data. The loss function may then be minimized using a standard optimization algorithm capable of handling non-convex problems. This example provides a framework for optimizing the performance of graphene EGFET arrays for specific applications under a number of design constraints and trade-offs. Although this example deals with optimizing voltage gain, the method may be readily applied to the optimization of other electrical characteristics, such as transconductance.

4.8 Summary

Large-scale sensor arrays based on graphene EGFETs represent a promising technology for both chemical and biological sensing applications. This work demonstrates a reliable fabrication process by producing a large-scale graphene EGFET

array with 256 devices and 100% yield. The developed array architecture in conjunction with a compact and self-contained measurement system enables DC characterization of 256 graphene EGFETs as a function of V_{DS} and V_{GS} within minutes. These technological advancements represent a milestone in the development of graphene EGFET sensors by enabling the convenient and rapid acquisition of high quality data for a large number of devices. Large sample size statistical data on the electronic performance of graphene EGFETs is provided for the first time. This includes mean and standard deviations for drain-source current, transconductance, output conductance, and intrinsic gain.

This employs the compact piecewise DC graphene EGFET model, which is shown capable of fitting 87% of graphene EGFET I_{DS} vs. V_{GS} curves with a mean percent error of 7% or less. The compact model enables the extraction of device parameters for a large number of graphene EGFETs for the first time. By extension, this enables the extraction of parameter distributions for mobility, contact resistance, minimum carrier concentration, and Dirac point. It is now possible to characterize the impact of different fabrication processes on device parameter distributions. This is an important step in the development of any sensor technology based on graphene EGFETs.

Lastly, this work provides some intuition regarding the impacts of design parameters and process-dependent parameters on the intrinsic voltage gain of graphene EGFETs. Graphene EGFETs exhibit reasonable gain making them suitable for use as amplifiers or buffers in certain sensing applications. To maximize performance, this work provides a framework for application-specific optimization of large-scale sensor arrays under a number of design constraints and trade-offs. The sum of these

contributions make this work a resource for the development of future chemical and biological sensor systems based on graphene EGFETs.

Chapter 5: Graphene Ionized Calcium Sensors

5.1 Introduction

This section adapts the previously developed graphene EGFET technology as a chemical sensor system for the detection of ionized calcium. The graphene EGFET-based chemical sensors are similar to silicon-based ion-selective field-effect transistors (ISFETs) in that they enable miniaturization ion-selective electrodes (ISEs) [135]. Unlike ISFETs, however, graphene exhibits high chemical stability and does not form a native oxide [61], [63], [136]–[138]. Using graphene EGFETs enables sensor arrays to scale much better than electrode-based approaches [139]. The abundance of graphene EGEFT sensors can also be used to exploit sensor redundancy and enhance measurement accuracy. Lastly, this work serves as a first step in the development of sensor systems capable of simultaneous multi-analyte detection in a compact form factor.

Use of graphene provides a number of advantages. In its simplest form, an unfunctionalized graphene EGFET sensor consists of a graphene channel between two conductive contacts. As such, graphene EGFET chemical sensors offer the benefit of simpler construction over silicon-based ISFET counterparts [140]. Unlike silicon-based ISFETs, graphene EGFET chemical sensors also lend themselves innately to mechanically flexibility and optical transparency for sensing applications [42], [68], [70], [71], [122], [141]. This can potentially enable low-profile smart skin type sensors [142]. Because graphene is atomically thin carbon, it is potentially extremely economical. Chemical vapor deposition growth processes also enables large-area synthesis with uniformity in material properties [37], [38].

Chemical sensors using graphene have been developed using a variety of functionalization chemistries [143]. Graphene functionalizations typically come in two flavors: covalent and noncovalent. Functionalizations are typically coupled to the graphene π-bonds, which are responsible for graphene's charge transport properties. Covalent bonds may provide added sensitivity and stability, but strongly disrupt π-bonds and degrade graphene's electrical properties. Noncovalent chemistries help minimize these adverse effects. Although both types of functionalization enhance sensitivity, they often do not effectively block interfering molecules from interacting with graphene's extremely sensitive surface [54], [55] . As a result, selectivity—an equally important performance metric—is typically poor or goes unreported altogether. This blocking function is critical because as an all-surface material, graphene exhibits innate sensitivity to many environmental changes [119], [144].

This chapter develops a compact sensor system capable of monitoring hundreds of graphene Ca^{2+} sensors simultaneously. This enables thorough evaluation of graphene Ca^{2+} sensor performance at a statistically significant sample size (N=152). The Graphene Ca^{2+} sensors are based on graphene electrolyte-gated field-effect transistors (EGFETs) and are functionalized for ionized calcium using a polyvinyl chloride (PVC) membrane containing a neutral calcium ionophore (ETH 129) [145], [146]. Ionophores provide sensitivity and a high degree of selectivity for ionized calcium. Ca^{2+} was chosen as the target analyte because of its commonplace in diagnostic testing and physiological importance in blood, urine, and sweat [142], [147], [148].

Graphene Ca^{2+} sensors are shown capable of accurately quantifying ionized calcium concentrations over several orders of magnitude. Sensors exhibit excellent

reversibility and response time. Sensors also exhibit a virtually ideal Nernstian response of 30.1 mV/decade with little variation (σ = 1.9 mV/decade). This work contributes an alternative calibration and measurement method using a least squares distribution matching technique that extracts relative shifts in the *I-V* characteristics to quantify ionized calcium concentrations. The method is much faster in that it eliminates the need for full *I-V* characterization at each measurement. The method provides the added benefit of requiring only one calibration solution—making it particularly useful for portable and field-deployable sensor systems. The ability to monitor a large sample size also shows that redundancy in graphene Ca^{2+} responses can be exploited to more accurately quantify ionized calcium concentrations. Sensor redundancy is shown capable of tightening of 95% confidence intervals from ±50% to ±10% of the ionized calcium concentration.

6.2 Graphene Ionized Calcium Sensor Array Fabrication

Fabrication begins with piranha cleaning a 300 μm thick glass substrate. The substrate was coated with 25 nm aluminum oxide using atomic layer deposition to aid adhesion in subsequent photolithography steps. A layer of Ti/Au (5 nm / 300 nm) was deposited using electron beam deposition to form the rows of the sensor array. A 25 nm layer of aluminum oxide was then deposited as interlayer dielectric using atomic layer deposition. Openings were etched into the interlayer dielectric using a BCl_3 plasma to allow contact between the first and second metal layers in the array where appropriate. A second metal layer of Ti/Au (5nm / 300 nm) was then deposited using electron beam deposition. Graphene coated with PMMA from ACS Material was transferred on the substrate so as to cover the entirety of the array. The chip was baked at 80°C for 15

minutes and 130°C for 2 hours. This allows PMMA reflow and enhances adhesion between the graphene and substrate. The sensor array chip was then immersed in acetone for several hours to remove the PMMA.

The chip was subsequently annealed at 350°C in 400 sccm Ar and 7000 sccm H_2 to reduce PMMA residue and further enhance adhesion between the graphene and substrate. The graphene was mesa etched using MMA/SPR3012 resist stacks and oxygen plasma. Both resists were then removed by immersion in acetone for several hours. The chip was spin coated with SU-8 and openings were defined over the graphene channel regions and contact leads. The ion-selective membrane solution was then made by mixing 0.656 g of 2-nitrophenyl octyl ether (oNPOE), 0.328 g of high molecular weight polyvinyl chloride (PVC), 0.01 g of calcium ionophore II (ETH 129), and 0.06 g of potassium tetrakis(4-chlorophenyl) borate. The mixture was dissolved in 6 mL of tetrahydrofuran (THF), which is approximately 85% by weight. The solution was then spin coated over the array at 1500 rpm for 120 seconds and allowed to air dry. The complete measurement system with chip insert is depicted in **Figure 5.1.**

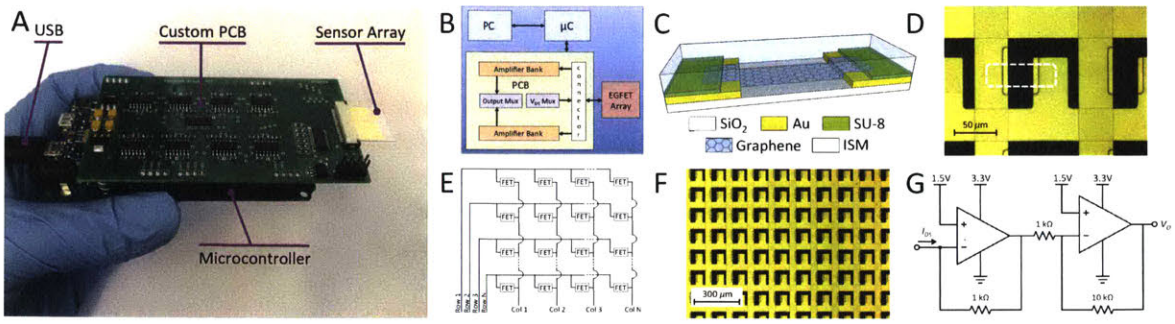

Figure 5.1: A) measurement system with sensor array insert, B) system-level overview, C) graphene Ca^{+} sensor diagram, D) microscope image of a single graphene Ca^{2+} sensor with graphene region outlined (dashed white), E) sensor array architecture, F) microscope image of graphene Ca^{2+} sensor array, G) transimpedance amplifier schematic.

6.3 Measurement Setup

A custom measurement system was employed to rapidly acquire high-quality data from a large number of graphene EGFET Ca^{2+} sensors in a convenient manner. The sensor array chip may be dipped into the solution to measure the analyte concentration. The measurement setup houses a low profile Ag/AgCl reference electrode, which is dipped into the solution along with the sensor array. This allows for a stable reference potential and high-quality data acquisition. The measurement system monitors the source-drain current I_{DS} for each row and column combination in the sensor array. The measurement system also provides control of the gate-source voltage V_{GS} and drain-source voltage V_{DS}. The measurement setup for a single sensor within the array is depicted in **Figure 5.2A**.

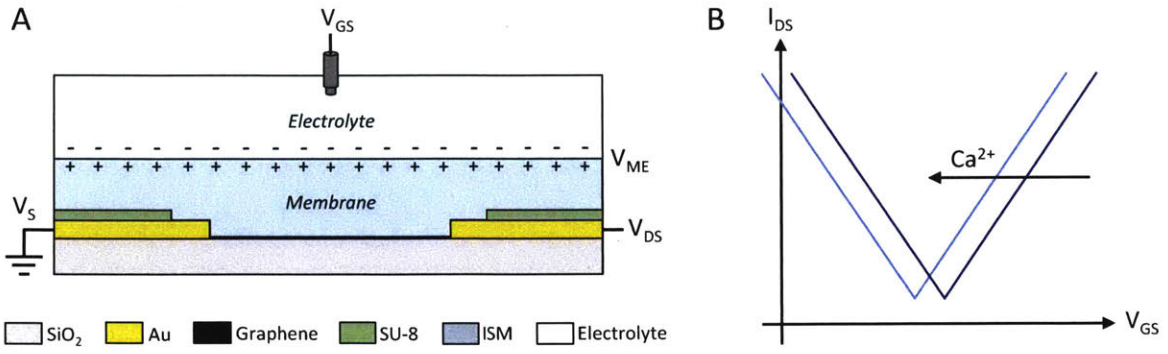

Figure 5.2: A) Graphene Ca^{2+} sensor diagram depicting measurement setup and aligned potential at the membrane-electrolyte interface, B) idealized graphene Ca^{2+} sensor *I-V* characteristic response.

6.4 Graphene Ionized Calcium Sensor Theory

Graphene Ca^{2+} sensor theory is based on a strong understanding of the electrical characteristics of graphene electrolyte-gated field-effect transistors [110], [130]. Transport of ionized calcium at the interface between the electrolyte and the ion-selective membrane is governed by the Nernst equation [149]. In equilibrium, diffusion of Ca^{2+} across the interface is counterbalanced by the electric field induced by the Ca^{2+} ions. This interface potential is depicted in **Figure 5.2A**. As the concentration of Ca^{2+} ions in the solution is increased, the electric field required counterbalance diffusion must increase. Thus, the interface potential increases with increasing Ca^{2+} concentration. Because the interface polarity is aligned with the polarity of V_{GS}, the same current can be achieved at a lower applied V_{GS} in the presence of higher Ca^{2+} concentration. Hence, increasing Ca^{2+} concentration induces a leftward shift of the graphene *I-V* characteristic—depicted in **Figure 5.2B**—resulting in a more p-doped channel.

Ion-selective membranes function by keeping the target ion concentration constant within the membrane phase. This translates into an electrolyte-interface

potential that is solely a function of the target analyte concentration. Because of this, the interface potential can be related back to the target analyte concentration in the electrolyte phase. The ion-selective membrane in this work is based on a charge neutral ionophore. Ionophores are lipophilic molecules that selectively bind to an ion of interest, in this case Ca^{2+}. Ionophores provide both sensitivity and selectivity. Because ionophores are lipophilic they possess a high affinity for the membrane phase over the solution phase and may be assumed confined to the membrane

In order for the analyte, in this case a cation, to move into the membrane in sufficient quantities, another cation must leave the membrane so as to maintain overall charge neutrality. This is the role of ion-exchangers in the membrane. The ion exchanger is a molecule that dissociates within the membrane into a lipophilic anion and a cation that is free to leave the membrane as the analyte cation enters. The lipophilic ion-exchanger anion counterbalances the analyte cation in the membrane so as to maintain overall charge neutrality.

The dominant reaction occurring at the membrane-electrolyte interface is given by (5.1)

$$I_E + L_M \rightleftharpoons IL_M \tag{5.1}$$

where I_E represents the analyte cation (Ca^{2+}) in the electrolyte phase, L_M represents the unbound neutral calcium ionophore, and IL_M represents the complexed ionophore in the membrane phase. The potential at the membrane-electrolyte interface determined by the dominant reaction and governed by the Nernst equation as given by (5.2)

$$V_{ME} = V_M - V_E = V^0 + 2.3\frac{RT}{zF}\log\left(\frac{c_I^E}{c_I^M}\right) \tag{5.2}$$

where V_{ME} is the potential difference between the membrane and electrolyte, V_M is the membrane potential, V_E is the electrolyte potential, V^0 is the built in potential due to differences in electrochemical potential, R is the gas constant, T is the temperature, z is the charge number of the analyte, F is the Faraday constant, c_I^E is the concentration of analyte in the electrolyte phase, and c_I^M is the analyte concentration present in the membrane phase. When c_I^M remains constant, the potential can be related directly to the concentration of c_I^E as shown in (6.3)

$$V_{ME} = V^\theta + 2.3\frac{RT}{zF}\log(c_I^E) \tag{5.3}$$

where V^0 has been renamed V^θ to include the constant term resulting from the $\log(c_I^M)$. For a bivalent ion such as Ca^{2+} at room temperature, the slope is theoretically approximately 30 mV/decade. This translates directly to the minimum conduction point, Dirac point, which shifts by the same amount according to (5.4)

$$V_{\text{Dirac}} = V_{\text{Dirac}}^0 - 2.3\frac{RT}{zF}\log(c_I^E) \tag{5.4}$$

Because graphene EGFET have v-shaped and approximately linear *I-V* characteristic away from the minimum conduction point, there exists a direct linear

relationship between the shift in voltage and change in current. Therefore, it is possible to relate the change in current to the change in analyte concentration as given by (5.5)

$$I_{DS} = I_{DS}^{0} + k \log(c_I^E) \tag{5.5}$$

where I_{DS}^{0} is some constant baseline source-drain current and k is the slope of the voltage shift multiplied by the slope of the graphene *I-V* curve at that particular point.

6.5 *I-V* Characteristics

A solution of 1 M aqueous Ca^{2+} was diluted over several orders of magnitude to provide a variety of concentrations: 100 mM, 10 mM, 1 mM, 100 μM, 10 μM. *I-V* characterization was performed for all devices at each Ca^{2+} concentration. The drain-source voltage V_{DS} was held constant at 100 mV and the gate-source voltage V_{GS} was swept from -0.5 V to 1.0 V in 10 mV increments. A 10-second hold time was used before the gate-source voltage V_{GS} was swept at a rate of 10 mV / 500 ms. This provides adequate time for charged species to migrate and reach steady-state before measurement. Channel dimensions of the graphene Ca^{2+} sensors were W/L = 30 μm / 30 μm. All measurements were conducted under ambient conditions at room temperature.

Solution volumes were large enough (approximately 50 mL) so as not to evaporate appreciably over the course of the experiment. Solution volumes were also large enough so that contamination when moving from lower concentrations to higher concentrations was negligible and could not appreciably alter the Ca^{2+} concentrations. The *I-V* characterization results as a function of concentration are reported in **Figures 5.3-5.5**. The average shift in minimum conduction point as a function of ionized calcium

concentration is provided in **Figure 5.5B**. The average slope of -30.1 mV/dec is in excellent agreement with the theoretical Nernstian slope for a bivalent ion as derived from (6.3). The minimum conduction points, or Dirac points, were calculated as accurately as possible by polynomial fitting the discretized *I-V* characteristics and finding the minimum of the continuous polynomial fit. Further details are provided in the **Appendix A2.**

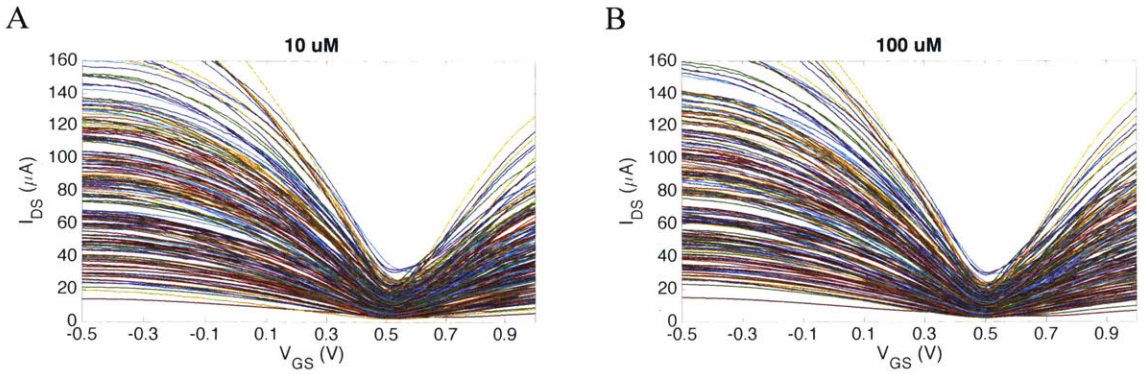

Figure 5.3: *I-V* characteristic for graphene Ca^{2+} sensors in ionized calcium concentrations of A) 10 μM, and B) 100 μM. The sample size is 152 and all measurements are taken at V_{DS} = 100 mV.

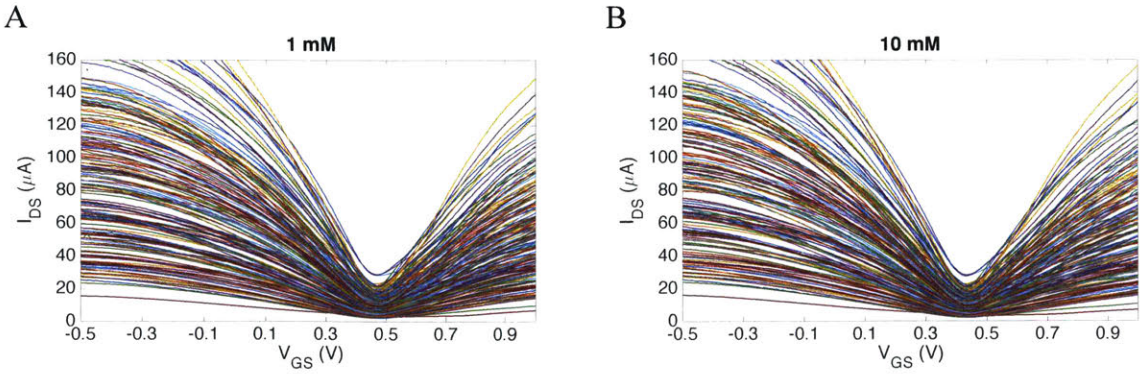

Figure 5.4: *I-V* characteristic for graphene Ca^{2+} sensors in ionized calcium concentrations of A) 1 mM, and B) 10 mM. The sample size is 152 and all measurements are taken at V_{DS} = 100 mV.

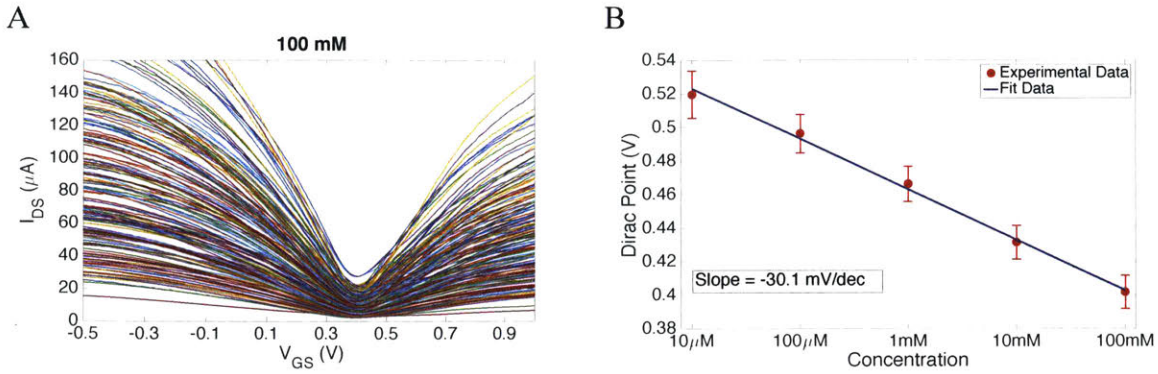

Figure 5.5: A) *I-V* characteristic for graphene Ca^{2+} sensors in ionized calcium concentrations of 100 mM, and B) the slope of the minimum conduction point as a function of ionized calcium concentration. The sample size is 152 and all measurements are taken at V_{DS} = 100 mV.

The distribution in sensor sensitivity is depicted in **Figure 5.6**. A normal quantile plot shows the variation in sensitivity to be normally distributed. The mean sensitivity is 30.1 mV/decade with a standard deviation is 1.9 mV/decade. The distribution is quite narrow with almost all sensitivities being 26-34 mV/decade.

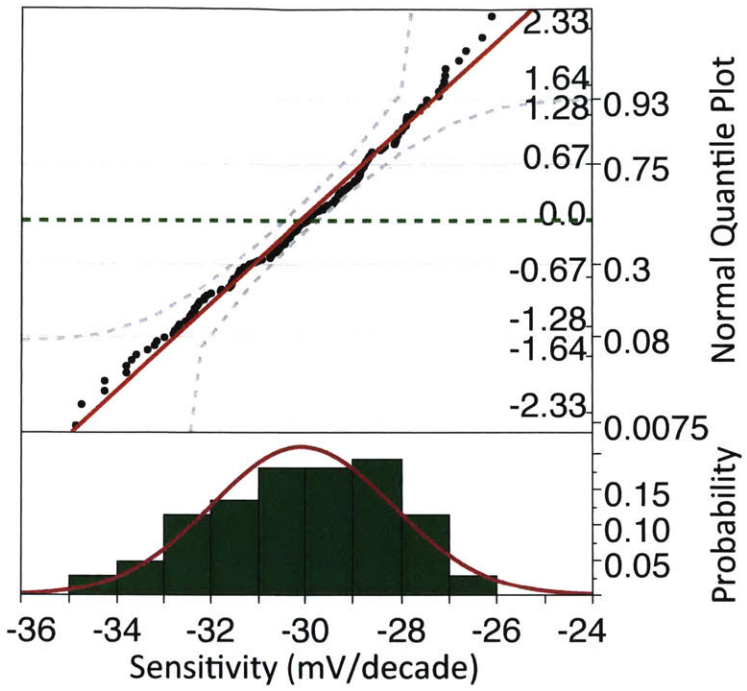

Figure 5.6: Distribution of graphene Ca^{2+} sensors sensitivities. Normal quantile plot of sensitivity distribution falls within the 95% confidence interval (dashed gray) for an ideal Gaussian distribution (red). Mean is close to the 50^{th}-percentile (dashed green).

5.6 Transient Response

Transient response was investigated by dipping the graphene Ca^{2+} sensor array in dilutions of ionized calcium spanning several orders of magnitude. The graphene Ca^{2+} sensor array was immersed in each dilution for approximately 20-30 seconds. The experiment begins with increasing ionized calcium concentrations to reduce the potential of altering the solution concentrations due to cross contamination. Once the maximum concentration was reached, the sensor array was repeatedly exposed to lower concentrations to demonstrate reversibility. Exposure to decreasing concentrations poses greater risk of altering the solution concentration due to cross contamination. Spikes in

data represent transition times of the sensors from one solution to the next. The graphene Ca^{2+} transient response is depicted in **Figure 5.7** over several orders of magnitude change in ionized calcium concentration.

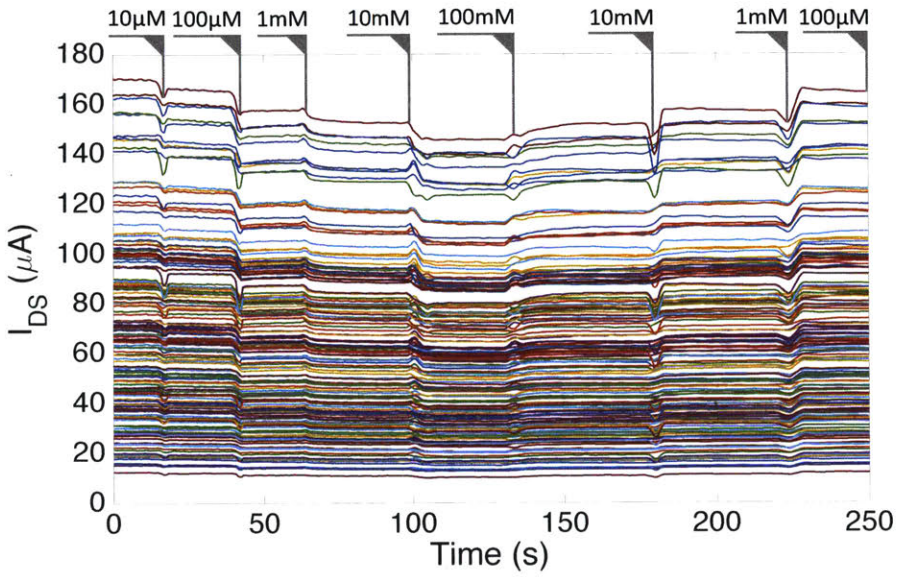

Figure 5.7: Graphene Ca^{2+} sensor transient responses to changing concentrations in ionized calcium. Sample size is 152 and the bias conditions are $V_{DS} = 100$ mV, $V_{GS} = 0$ V.

Transient response experiment also shows that graphene Ca^{2+} sensors exhibit excellent reversibility. This is a key trait because it enables sensors to be used to continually monitoring varying concentrations of ionized calcium. Average sensitivity and reversibility of the sensor current response is depicted in **Figure 5.8**. The result is consistent with (5.4).

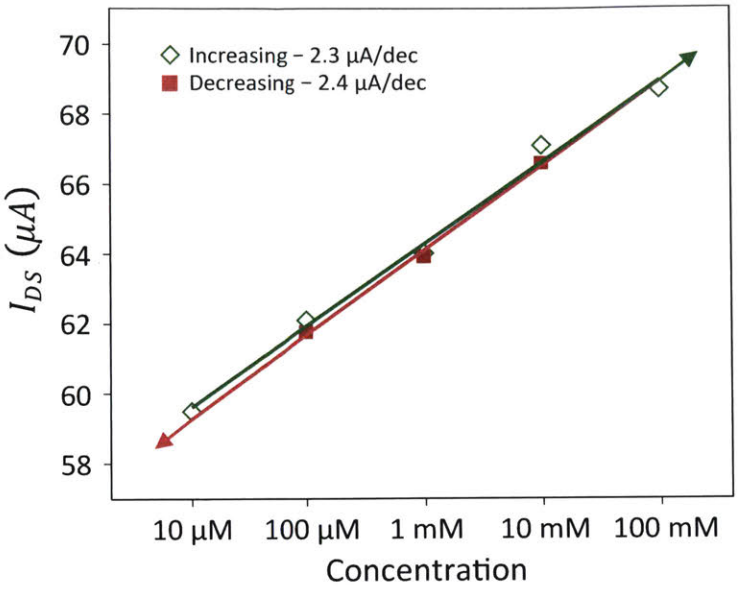

Figure 5.8: Mean sensitivity response showing excellent sensitivity and reversibility over several orders of magnitude in ionized calcium concentration.

5.7 Alternative Calibration & Measurement Method

The calibration of chemical sensors is typically performed on equally spaced analyte concentrations that span the entire range of interest. Calibration is critical for even the most mature chemical sensor technologies such as pH sensors because chemical sensors inherently drift with time [150]–[153]. Graphene EGFET chemical sensors are typically characterized and calibrated using multiple dilutions in a method similar to that depicted in **Figure 5.3-5.5** [154]–[156]. Concentrations are then measured by characterizing the entirety of the *I-V* characteristic and relating the shift to changes in concentration. Voltage sweeps required for *I-V* characterization, however, are very slow (e.g. 10 mV / 500 ms) in order to provide adequate time for ions to migrate and for the sensor to reach steady state.

A faster (more practical) method is investigated for determining analyte concentration directly from the sensor operating current I_{DS}. This eliminates the need to perform full *I-V* characterization for each measurement. The method is based on the fact that changes in concentration produce changes in sensor operating current I_{DS}. These changes in operating current I_{DS} can be mapped to a specific location of the *I-V* characteristic using a standard optimization technique such as least squares fitting. The specific location on the *I-V* characteristic can then be used to determine the relative shift in the *I-V* characteristic and hence the solution concentration. This requires only one *I-V* characteristic calibration be performed at some reference concentration. A depiction of the process is provided in **Figure 5.9**. Specifics regarding the least square fitting procedure are provided in the **Appendix A2**.

This method is particularly advantageous in that it eliminates the need for multiple calibration solutions. This is useful for sensing applications targeting portability and field use, which make carrying multiple concentrations or dilution preparation impractical. The calibration and measurement method effectively shifts complexity associated with solution preparation and calibration into the electrical domain. Added complexity in the electrical domain, however, is readily accommodated as electronic components such as microcontrollers are inexpensive and provide ample computational ability.

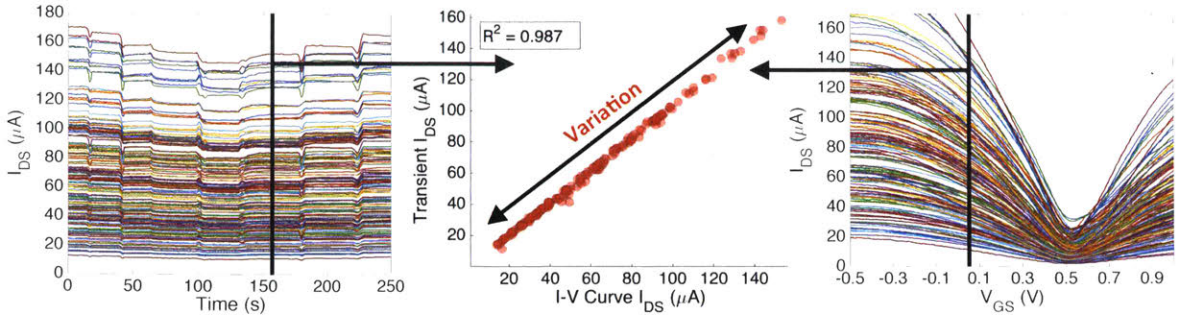

Figure 5.9: Distribution matching of transient data to *I-V* curve data to extract Ca^{2+} concentration. The regression plot shows that least squares minimization can be used to effectively map the distribution of transient data to *I-V* characteristic data.

The performance of the alternative measurement technique is investigated over several orders of magnitude of change in ionized calcium concentration. Ionized calcium concentrations are measured from transient response data using the least squares distribution matching technique outlined in **Figure 5.9**. Calculated concentrations are then compared to nominal concentrations capturing the combined accuracy of the graphene Ca^{2+} sensors and measurement technique. **Figure 5.10A** shows graphene Ca^{2+} sensors quantifying ionized calcium concentration exceptionally well over several orders of magnitude. This method requires only single *I-V* characteristic calibration as a reference.

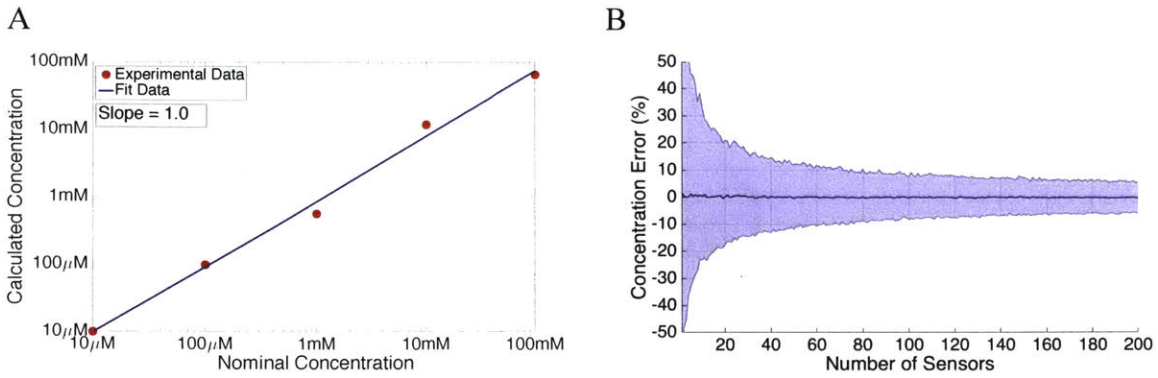

Figure 5.10: A) Calculated concentration versus true concentration using profile matching technique. B) Mean percent error and 95% confidence intervals as a function of sensor count for Ca^{2+} concentrations. The sample size is 152 and the bias conditions are V_{DS} = 100 mV, V_{GS} = 0 V. Profile matching was performed using the 10 μM *I-V* curve calibration data and a sensitivity of 30.1 mV/decade.

5.8 Benefits of Redundancy

This section quantifies the benefits of having redundancy in graphene Ca^{2+} sensors from an arrayed architecture. Benefits are quantified by extending the population size of 152 sensors to a synthetic population size of 50,000 transient responses and corresponding *I-V* characteristics. Synthetic transient responses and *I-V* characteristics are generated according to empirical cumulative distribution functions (ECDFs) derived from experimental data so as to mimic experimental data as closely as possible. Extending population size allows for more thorough statistical analysis including simulation beyond 152 sensors. It also remedies statistical issues arising when the randomly generated sample size approaches the population size.

For each sample size, the corresponding number of transient responses and *I-V* characteristics are randomly sampled from the overall population size. This captures the randomness associated with fabricating individual sensor arrays with *N* graphene Ca^{2+} sensors. Ionized calcium concentrations are then calculated to capture the randomness in

measurement accuracy of for a sensor array with N graphene Ca^{2+} sensors. This process is repeated at each sample size 1000 times to generate a distribution and capture the randomness associated with measurement accuracy as a function of sample size. These distributions allow the mean and 95% confidence intervals to be calculated for ionized calcium concentrations as a function of sample size. This quantifies the benefits of having redundancy in graphene Ca^{2+} sensors. The results are depicted in **Figure 5.10B** and show tightening of the confidence intervals as a function of sample size. Sensor redundancy is shown capable of tightening of 95% confidence intervals from ±50% to within ±10% of the ionized calcium concentration. Measurement accuracy is asymptotically related to sample size and produces diminished returns with increasing sample size. Further details regarding the data synthesis process may be found in the **Appendix A2.**

5.9 Summary

This work develops a compact sensor system capable of monitoring hundreds of graphene Ca^{2+} sensors simultaneously in a convenient and high-quality fashion. This technology is employed to thoroughly evaluate graphene electrolyte-gated field-effect transistors (EGFETs) functionalized for the detection of ionized calcium. Graphene EGFETs were functionalized for the detection of ionized calcium using a polyvinyl chloride (PVC) membrane coating embedded with a neutral calcium ionophore. The resulting graphene Ca^{2+} sensors are shown capable of accurately quantify ionized calcium concentration overall several orders of magnitude while exhibiting a virtually ideal Nernstian response of 30.1 mV/decade. Variation in sensitivity is shown normally

distributed with little variation (σ = 1.9 mV/decade), indicating a high degree of consistency and reproducibility for the observed response. Sensors are shown to exhibit excellent reversibility and response time. Sensors of this type are also known to exhibit excellent selectivity.

This work introduces an alternative calibration and measurement method using least squares distribution matching in order to extract relative shifts in *I-V* characteristics and quantify ionized calcium concentrations. This method is faster in that it eliminates the need for full *I-V* characterization at each measurement. The method is also beneficial in that it only requires one calibration solution making it particularly useful for portable and field-deployable sensor systems. This is a stark contrast to conventional calibration techniques, which require multiple solutions concentrations spanning the range of interest.

The ability to monitor a statistically significant sample size (N=152) also enables the benefits of sensor redundancy to be quantified. Sensor redundancy is shown capable of tightening of 95% confidence intervals from ±50% to within ±10% of the ionized calcium concentration. Redundancy can be effectively exploited to enhance the measurement accuracy of ionized calcium concentration. Measurement accuracy is asymptotically related to sample size and produces diminished returns with increasing sample size. These contributions represent milestones in the exploration of selective graphene EGFET-based chemical sensors. This work for graphene Ca^{2+} sensors is also readily extended to other analytes for the development of multi-analyte graphene EGFET-based sensor arrays.

Chapter 6: Graphene Sensors for Ammonia Detection

6.1 Introduction

This chapter adapts the previously developed graphene sensor system to evaluate $Co(tpfpp)ClO_4$ functionalization of graphene for ammonia detection. Graphene material properties have led to extensive interest in graphene-based gas sensing [1]–[3], [5], [54], [157], [158]. Some of these properties include high carrier mobility and sensitivity [56]–[58], [120], [121], chemical stability [60], [61], [66], and mechanical strength [67]. Additional properties such as mechanical flexibility [159], [160] and low optical absorption [71], [72] may also enable low-profile flexible gas sensors. These properties along with the emergence of large-scale uniform graphene synthesis methods make graphene a promising material for gas-phase chemical sensing applications [37], [38].

A number of conductivity-based methods have been investigated for ammonia detection over the years. Conductivity-based ammonia detection has been reported for metal-oxide based sensors [161]–[163], conductive polymer-based sensors [164]–[167], as well as conductive polymer sensors functionalized with metal-complexes [168]. Additionally, graphene-based chemiresistive sensors have been shown to provide suitable platforms for the detection of ammonia in the gas phase [169]–[172]. Seredych et al. [173], [174] demonstrated the adsorption of ammonia on pristine graphene oxide and determined the interactions to be the result of ammonia reacting with surface groups on the graphene oxide. Conductivity-based ammonia detection with graphene has been reported for pristine [158], [175], polyaniline functionalized [169], [176], [177], SnO_2 and CuO nanostructure decorated [171], Cu-based MOF/graphene hybridized [178], fluorinated [179], and NO_2 doped [170] graphene sensors.

Noncovalent functionalization of carbon nanotubes (CNTs) with cobalt *meso*-arylporphyrins has been shown to provide sensitive and selective detection of amines [180]. This thesis applies a similar modular functionalization scheme to an array of microfabricated chemiresistive graphene-based sensors. Porphyrins are particularly well-matched for graphene-based sensing because they provide excellent sensitivity while producing minimal perturbation of graphene's band structure and electrical properties. Metalloporphyrins noncovalent interactions with the graphene's π-bonds leave much of graphene's unique electrical properties intact [181]. Many metalloporphyrins exhibit strong dipoles when bound to analyte and relatively weak dipoles in their unbound states [182]. This is particularly true for cobalt porphyrin when bound to NH_3 [183]. These strong dipole interactions alter the carrier concentration in the underlying graphene and ultimately modulate sensor conductivity based on analyte concentration [182], [184]. Porphyrins also represent an attractive functionalization because they provide a high degree of selectivity [184], [185].

A chemiresistive graphene sensor array is designed as an insertable chip for use in conjunction with a custom readout system. The readout system is compact and includes universal serial bus (USB) connectivity for portability and ease of use. It also includes custom data acquisition software. The combination of these features enables high-quality data acquisition for hundreds of sensors in a rapid and convenient fashion. In previous works, sample sizes and analysis were extremely limited – ranging from individual devices to tens of devices at best [180], [181]. The ability to monitor large sample sizes (N=160) provides new insights into performance variation and reproducibility. Data from the fabricated sensor array was used to develop a detailed kinetic model describing sensor

response profiles to changing ammonia concentrations. Measurements of the adsorption kinetics of ammonia on graphene films are limited and have been previously determined only for graphene decorated with platinum nanoparticles [186].

The sensor system represents a convenient vehicle to demonstrate scaled-up repeatability and the kinetic analysis of a pixelated testbed. $Co(tpfpp)ClO_4$ treated graphene sensors are shown to produce a four-fold increase in ammonia sensitivity over pristine graphene sensors. Sensors were also found to exhibit excellent selectivity over interfering compounds such as water and common organic solvents. The ability to monitor a large sensor array with 160 pixels provides insights into performance variations and reproducibility – critical factors in the development of practical sensor systems. All sensors exhibit the same linearly related responses with variations in response exhibiting Gaussian distributions, a key finding for variation modeling and quality engineering purposes. The mean correlation coefficient between sensor responses was found to be 0.999 indicating highly consistent sensor responses and excellent reproducibility of $Co(tpfpp)ClO_4$ functionalization. A detailed kinetic model is developed to describe sensor response profiles. The model consists of two adsorption mechanisms—one reversible and one irreversible—and is shown capable of fitting experimental data with a mean percent error of 0.01%.

6.2 Sensor Array Fabrication

Graphene chemiresistive sensors consist of a functionalized graphene channel between two conductive source-drain contacts. Fabrication of an array of sensors begins with clean glass substrate on which a two-layer metal grid is microfabricated to provide access lines to individual sensors. Commercial-grade graphene is transferred over the array and etched in order to define the graphene channel regions for each pixel. A passivation layer is deposited on top of the sensor array in which windows are opened to expose the graphene channel region of each pixel.

The graphene sensor array is designed as an insertable chip. The array takes advantage of wire sharing to the extent possible and enables access to M x N sensors using only M + N wires, where M and N represent the number of rows and columns, respectively. Source-drain current signals from the graphene sensors are amplified and converted to voltages using custom-designed circuitry that is packaged into a small form factor printed circuit board (PCB). The custom-PCB is further interfaced with a microcontroller, which enables sensor readout using an analog-to-digital converter (ADC) and data transmission to a personal computer for data recording and analysis. An overview of the graphene sensor system and its key components is presented in **Figure 6.1A-G**. Detailed information regarding sensor array fabrication and readout system design is included in the **Appendix A3**.

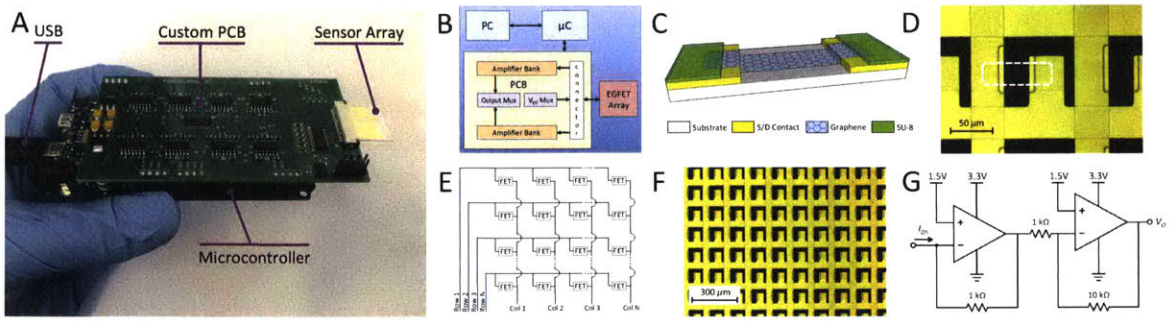

Figure 6.1: A) Complete measurement system and sensor array insert, B) system overview, C) graphene sensor diagram, D) microscope image of graphene sensor with channel region outlined in white (dashed), E) sensor array architecture, F) microscope image of graphene sensor array, G) transimpedance amplifier schematic.

6.3 Sensor Array Functionalization

5,10,15,20-tetrakis(pentafluorophenyl)porphyrinatocobalt(III) perchlorate—also referred to as cobalt porphyrin and $Co(tpfpp)ClO_4$—is depicted in **Figure 6.2** and was synthesized according to previously published procedures[180]. After synthesis, the porphyrin compound was dissolved in dichloromethane (DCM) at a concentration of 0.075 mg/ml. The sensor array was functionalized with one microliter of the porphyrin solution, which was dropcast on the array and allowed to air dry. Further details regarding sensor array functionalization are provided in the **Appendix A3.**

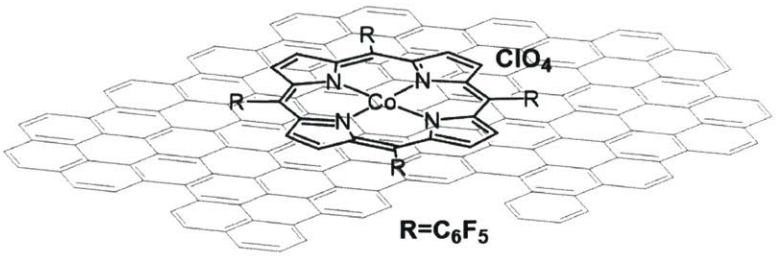

Figure 6.2: Chemical structure of the $Co(tpfpp)ClO_4$ selector unit on top of a graphene sheet.

6.4 Control Comparisons

Initial investigations quantify the sensor responses to changing concentrations of ammonia. Sensor array fabrication, functionalization, and detection methods are all detailed in the **Appendix A3**. **Figure 6.3A** shows the average change of conductance normalized to the initial conductance of the sensor. The response of all sensors—functionalized and unfunctionalized—in this study is semi-dosimetric. The sensor array comprised of pristine graphene shows moderate response towards 160 ppm ammonia (-2.27 ± 0.44% $\Delta G/G_0$). As an all-surface material, graphene's electrical properties are highly sensitive to surface molecular interactions, which alter graphene's carrier concentration and resulting conductivity. Ammonia possesses a dipole moment of 1.42 D. As a result, pristine graphene is expected to exhibit some innate sensitivity to ammonia concentration as well as other environmental factors [54], [144]. Our findings are consistent with previous results in which ammonia was found to reduce graphene conductivity through competition with the p-doping effect of physisorbed oxygen [157].

The ammonia response is found to increase four-fold upon graphene functionalization with Co porphyrin (-8.34 ± 0.19%). This is comparable to previously reported conductivity based sensors [158], [171], [178]–[180]. The robustness of the sensor when operated under ambient conditions was investigated. **Figure 6.3B** reveals that the responsiveness to 160 ppm ammonia decreases slightly from -8.34 ± 0.19% to -6.11 ± 0.63% when the carrier gas is changed from dry nitrogen to air with 41% relative humidity. All experimental results were obtained at a room temperature of 24°C. These results confirm sensor functionality in ambient conditions and quantify resilience in the presence of humidity. Homogeneity in responses is shown by ±σ shaded regions and error bars in **Figure 6.3A-C**. This attests to the overall reproducibility of the constructed sensors, which includes the microfabrication process and functionalization.

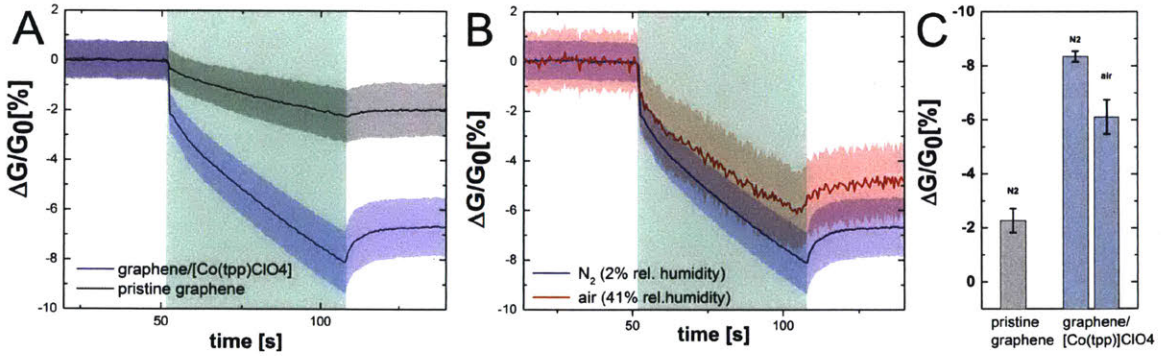

Figure 6.3: Percentile change in conductance of graphene sensor at an applied voltage of 100 mV. A) Mean change in conductance upon exposure to 160 ppm of NH_3 in nitrogen of the pristine graphene sensor and the Co(tpfpp)ClO_4 functionalized graphene sheet with shaded regions representing plus or minus one standard deviation from the mean. B) Mean change in conductance of the Co(tpfpp)ClO_4 functionalized graphene sheet upon exposure to 160 ppm of NH_3 in dry nitrogen and air with 41% relative humidity. Shaded regions represent plus or minus one standard deviation from the mean. Green highlighted regions represent time under ammonia exposure. C) Percentile change in conductance upon exposure to 160 ppm of NH_3 for 60 seconds.

6.5 Sensitivity

Sensor sensitivity was evaluated through investigation of the relationship between NH_3 concentration and the magnitude of the response. **Figure 6.4A** shows the mean responses plus or minus one standard deviation for exposures to 20 ppm, 40 ppm, 80 ppm, and 160 ppm NH_3 in nitrogen. The signal strength was found to increase with ammonia concentration (**Figure 6.4B**) allowing for quantitative measurement of NH_3 in the experimental window of concentration. The non-linearity of relationship between ammonia concentration and sensor response is postulated to result from interface reaction kinetics and, more specifically, the reduction in available functionalization binding sites with increased ammonia concentration. This trait is examined in further detail with the development of a kinetics-based sensor response model.

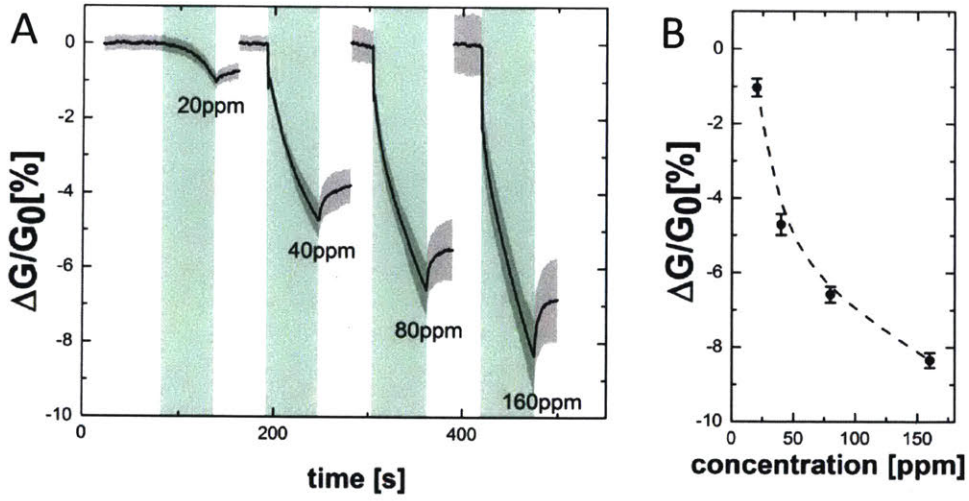

Figure 6.4: A) Mean percent change in conductance of functionalized graphene sensors in response to four different concentrations of NH_3. Shaded regions represent plus or minus one standard deviation from the mean. The green highlighted region represents the time under ammonia exposure. B) Mean sensor response as a function of NH_3 concentration for a fixed exposure time of 60 seconds.

6.6 Selectivity

Selectivity of the functionalized sensors was evaluated through exposure of the sensor array chip to water and a number of volatile organic compounds (VOCs). **Figure 6.5** depicts the mean sensor response to ammonia (160 ppm) versus the mean sensor response to hexane (160 ppm), ethanol (160 ppm), water (1,600 ppm), chloroform (160 ppm), and acetonitrile (320 ppm). Similar to our reported CNT-based sensing devices,[180] the graphene sensor exhibits negligible sensing responses for water and the examined VOCs (-0.19 to 0.06 %) when compared to ammonia (-8.23 ± 0.19 %). Thus, the sensitive and selection functionalization originally developed for CNTs effectively translates to graphene-based sensing devices.

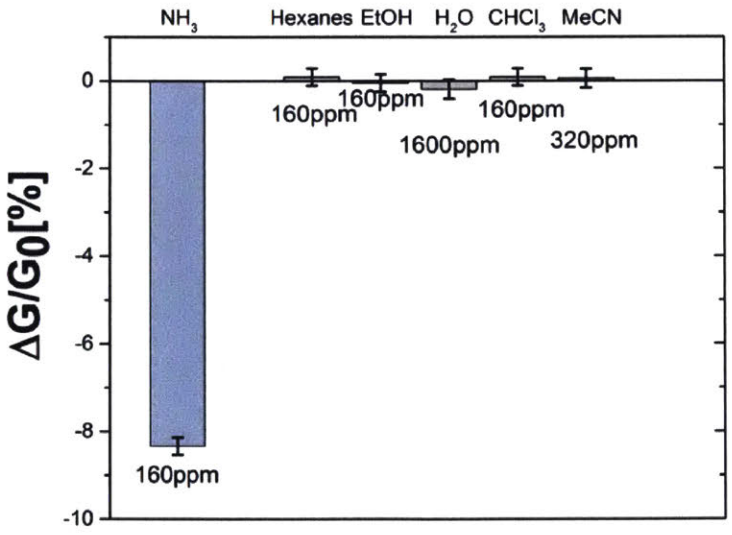

Figure 6.5: Selectivity comparison of the $Co(tpfpp)ClO_4$ functionalized graphene. Graphene sensors exhibit strong sensitivity to ammonia and suppressed responses to water and other VOCs.

6.7 Sensor Kinetics & Modeling

This section develops a quantitative model describing the observed behavior of the sensors in response to changing ammonia concentrations. The observed response curves indicate the existence of two different adsorption mechanisms: one reversible and one irreversible. The presence of an irreversible mechanism is supported by the sensor's failure to return to its initial baseline in the absence of ammonia. The existence of a reversible mechanism is supported by the partial recovery towards the baseline in the absence of ammonia. These two adsorption mechanisms are present in the data depicted in **Figure 6.6A**. The irreversible mechanism in the sensor response curves is attributed in part to the incomplete desorption of NH_3 from the Co porphyrin [180]. The reversible mechanism is attributed in part to NH_3 desorption from the Co porphyrin and to weaker reversible effects such as NH_3 physisorption onto the functionalized graphene surface.

The 2[nd]-order reversible reaction and kinetic equation are described by equations (6.1) and (6.2), respectively:

$$c_R + c_A \underset{\beta}{\overset{\alpha}{\rightleftharpoons}} c_{RA} \tag{6.1}$$

$$\frac{dc_{RA}(t)}{dt} = \alpha c_R(t) c_A(t) - \beta c_{RA}(t) \tag{6.2}$$

where α is the rate of the forward reaction, β is the rate of the reverse reaction, c_A is the analyte concentration, c_R is the concentration of reversible binding sites, and c_{RA} is the concentration of analyte bound to reversible binding sites. Similarly, the 2[nd]-order

irreversible reaction and kinetic equation are described by equations (6.3) and (6.4), respectively:

$$c_I + c_A \xrightarrow{\gamma} c_{IA} \tag{6.3}$$

$$\frac{dc_{IA}(t)}{dt} = \gamma c_I(t) c_A(t) \tag{6.4}$$

where γ is the rate of the forward reaction, c_A is the analyte concentration, c_I is the concentration of irreversible binding sites, and c_{IA} is the concentration of analyte bound to irreversible binding sites. Superimposing the two independent mechanisms and applying initial conditions $c_{RA}(t = 0) = 0$ and $c_{IA}(t = 0) = 0$ along with the fact that $c_A(t)$ is a constant, c_A, produces equation (6.5):

$$c_X(t) = c_{RA}(t) + c_{IA}(t) = \frac{\alpha c_A C_{RT}}{\alpha c_A + \beta}\left[1 - e^{-(\alpha c_A + \beta)t}\right] + C_{IT}\left[1 - e^{-\gamma c_A t}\right] \tag{6.5}$$

where $c_X(t)$ represents the total doping concentration on the sensor, C_{RT} represents the total number of reversible binding sites, and C_{IT} is the total number of irreversible binding sites. Graphene exhibits a cone-shaped band structure and linear *I-V* characteristic. The mean of the maximum ΔI_{DS} across the experiment is 6.7 μA whereas the average operating current I_{DS} is 44 μA. Linearity of the graphene *I-V* characteristic coupled with the small ΔI_{DS} response to changing doping allows the *I-V* characteristic to be accurately approximated as linear over the small range of interest. See **Appendix A3.**

Therefore, doping $c_X(t)$ is proportional to I_{DS}, and by extension $\Delta G/G_0$, leading to equation (6.6)

$$\Delta G/G_0 = H_0 + H_R e^{-(\alpha c_A + \beta)t} + H_I e^{-\gamma c_A t} \tag{6.6}$$

where H_R is a constant proportional to the number of reversible binding sites, H_I is a constant proportional to the number of irreversible binding sites, and H_0 is a constant accounting for the sensor baseline response. The derived model is fit to the experimental data as shown in **Figure 6.6A**. The full sensor response to the presence and absence of analyte is given by a piecewise model detailed in the **Append A3**. The derived piecewise model is shown capable of fitting experimental data exceptionally well resulting in mean percent error of only 0.01%.

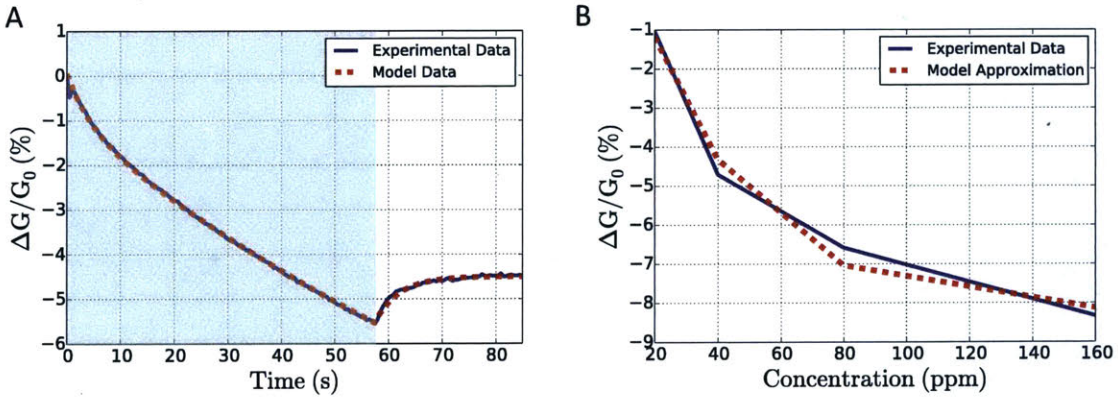

Figure 6.6: A) Mean graphene sensor response to 80 ppm NH_3 exposure and subsequent exposure to pure N_2. Green highlighted region represents time under ammonia exposure. B) Graphene sensor response for 60s NH_3 exposures as a function of increasing NH_3 concentration.

The irreversible reaction due to $Co(tpfpp)ClO_4$ functionalization produces the stronger signal, $H_I > H_R$, as is expected. The reversible reaction, however, reaches equilibrium more quickly indicating a faster time constant. Sensor response for a fixed exposure time of 60 seconds is found to decay with increasing analyte concentration c_A as shown in **Figure 6.6B**. This trend is consistent with the kinetic model given in (6.6).

6.8 Sensor Variation & Reproducibility

The ability to interrogate a large sample size (N=160) provides new insights into performance variation and reproducibility—two critical factors in the development of practical sensor systems. Correlation coefficients between sensor responses are investigated to assess the overall consistency in response across the sensor array. Correlation coefficients were calculated between every pairwise combination of sensors. The mean correlation coefficient was found to be 0.999. This near perfect linear relationship between sensor responses means variability in responses such as those depicted in **Figure 6.7A** are in fact near perfect scalar multiples of each other. This is an important finding because it allows variations in sensitivity to be readily "normalized out" in a non-computationally expensive fashion through multiplication of the sensor array responses by a constant matrix.

No sensor responses were found uncorrelated or inversely correlated—meaning there were no outliers in sensor response. In fact, the minimum correlation coefficient between any two sensors was approximately 0.991. This attests to the consistency of the sensor fabrication process and excellent reproducibility of the $Co(tpfpp)ClO_4$ functionalization chemistry. P-values corresponding to the correlation coefficients were

less than 0.0001. The probability distribution for correlation coefficients and corresponding heat map (inset) are provided in **Figure 6.7B**.

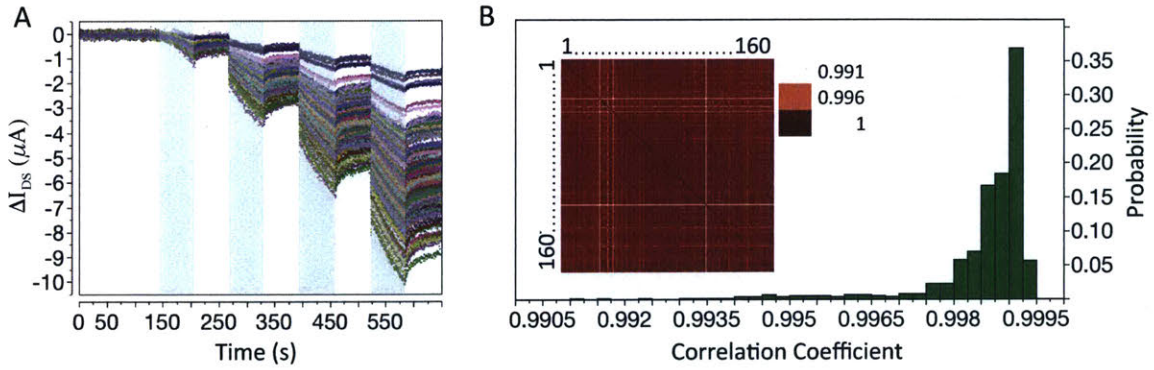

Figure 6.7: A) Sensor responses to 20, 40, 80, and 160 ppm of NH_3 with 60-second exposures to pure N_2 occurring at regular intervals. Green highlighted regions represent time under ammonia exposure. Each sensor response is represented by a different color. The legend is omitted due to the large sample size. B) Probability distribution of correlation coefficients across sample size of N=160 and corresponding heat map of correlation coefficients (inset) with red and blue indicating correlation coefficients of 1 and -1, respectively.

Further analysis shows that sensors with higher source-drain current I_{DS} also exhibit higher sensitivities ΔI_{DS}. This is shown **Figure 6.8A** by the four plots exhibiting negative regression slopes. The plots compare ΔI_{DS} (sensitivity) versus I_{DS} for different operating conditions (e.g. in the presence of NH_3 and pure N_2.) Regardless of the operating conditions, sensitivity ΔI_{DS} is linearly related to operating current I_{DS}. This finding is consistent with the fact that variation in sensitivity stems from variation in the sensor operating current. This is demonstrated geometrically using idealized graphene *I-V* curves shown in **Figure 6.8B**. Changes in analyte concentration are known to alter the doping of the graphene channel and effectively shift the *I-V* curve of the graphene sensor.

This is a well-established phenomenon for direct current graphene-based sensors and represents the fundamental operating principle for these devices irrespective of application [55], [69], [188], [88], [119], [121], [130], [144], [154], [157], [187]. This implies that variation in sensitivity ΔI_{DS} may be minimized by reducing the variation in the underlying sensor operating current I_{DS}. This may be achieved by reducing variation in graphene material properties through the development of more uniform graphene growth, transfer, and microfabrication techniques.

The two plots in **Figure 6.8A** with positive regression slopes are comparisons between I_{DS} and ΔI_{DS} for different operating conditions. Sensors exhibiting higher I_{DS} current under one condition (e.g. exposure to NH_3) were found to consistently exhibit higher I_{DS} currents under other conditions (e.g. exposure to pure N_2). In addition, sensors exhibiting the highest sensitivities ΔI_{DS} under one condition continue to exhibit highest sensitivities under other operating conditions. Thus sensor rank in terms of performance remains consistent despite changes in operating conditions. It is important to note the high degree of linearity in the regression slopes. This supports sensor operation that closely resembles the idealized depiction in **Figure 6.8B**. Any nonlinearity in the *I-V* curve would manifest itself as nonlinearity in the regression slopes.

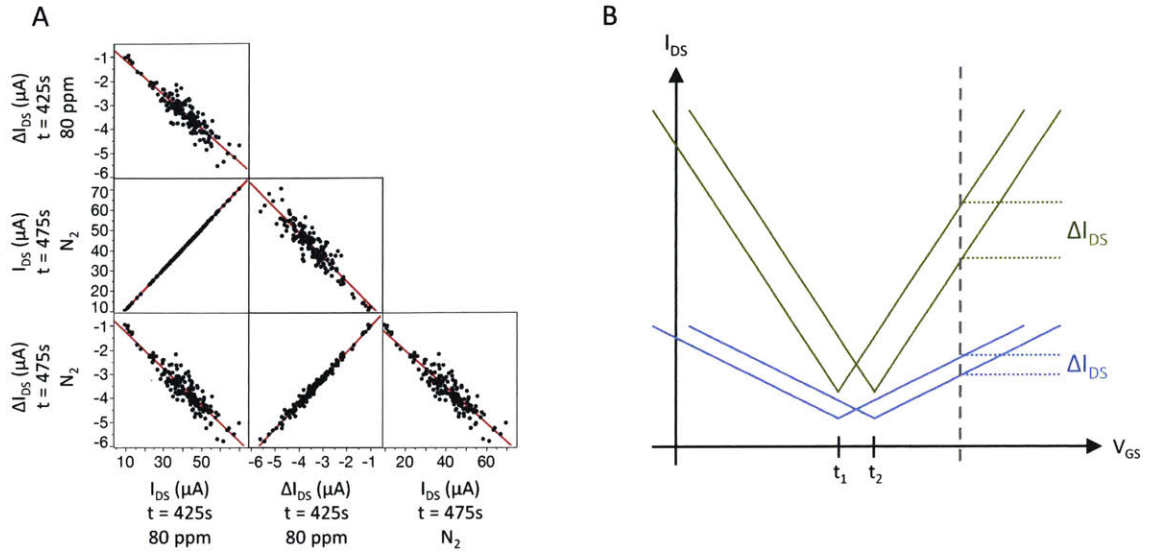

Figure 6.8: A) Scatterplot matrix showing relationships between sensor I_{DS} and ΔI_{DS} under different operating conditions (NH_3 vs. N_2) and B) idealized geometric explanation for the observed graphene sensor behavior.

Sensor response variations are examined for two cases of importance: sensor operation in presence of NH_3 and sensor operation in the absence of NH_3. More specifically, sensitivity data ΔI_{DS} is examined for 160 ppm NH_3 exposure (t = 550s) and for subsequent exposure to pure N_2 (t = 625s). **Figure 6.9** shows variations exhibit nearly ideal normal distributions under both operating conditions. This allows sensor performance variations to be accurately modeled using Gaussian distributions for quality engineering purposes. This is an important finding because the overall variation in sensitivity encapsulates a number of underlying variations including non-uniformities in the graphene material, the microfabrication process, and application of functionalization chemistry. Normal quantile plots show that sensitivity variations mimic nearly ideal

normal distributions with experimental data falling within the 95% confidence limits (gray dashed) and having a 50th percentile (green dashed) close to the sample mean.

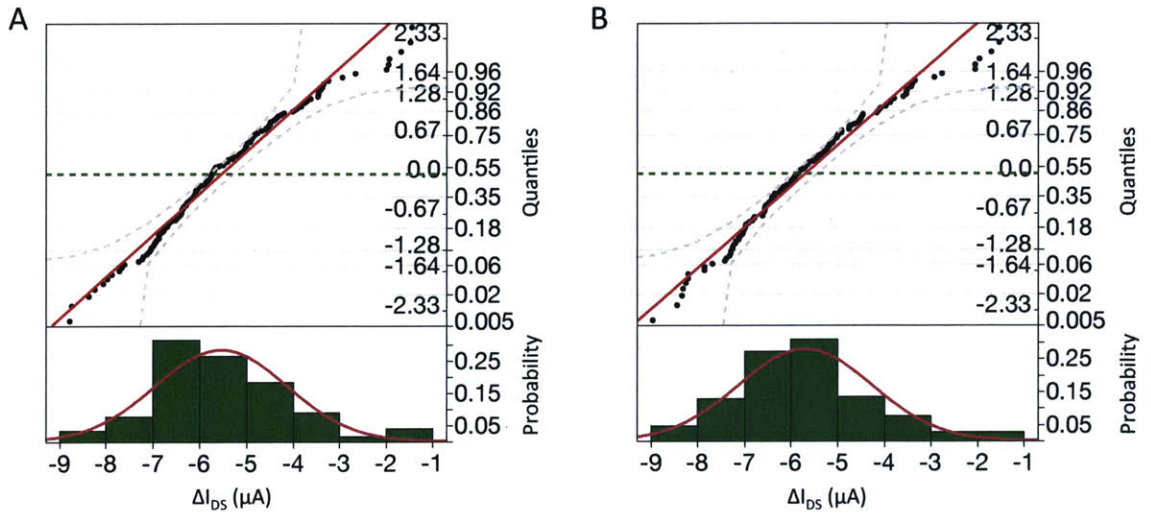

Figure 6.9: Sensor response distributions and normal quantile plots for A) sensor exposure to 160 ppm NH_3 and B) subsequent exposure to pure N_2.

6.9 Summary

This work develops a novel sensor system as a convenient vehicle for scaled-up repeatability and the kinetic analysis of a pixelated testbed. The compact sensor system is capable of monitoring hundreds of graphene sensors in a rapid and convenient fashion. Co(tpfpp)ClO_4 functionalization of graphene sensors was found to increase sensitivity to ammonia four-fold over pristine graphene sensors. Sensor conductance was found to decay with increasing ammonia concentration, which is consistent with a reduction in the number of available functionalization binding sites for higher concentration exposures. Sensors also possess excellent selectivity with responses to ammonia being orders of magnitude greater than the responses to interfering compounds such as water and common organic solvents.

A physical model based on absorption kinetics was developed and shown to accurately describe sensor response profiles. The model comprised two adsorption mechanisms—one reversible and one irreversible—and was shown capable of fitting experimental data with a mean percent error of 0.01%. The model is also consistent with the experimental observation of decayed sensor response in response to increasing ammonia concentration.

The ability to monitor hundreds of sensors provided new insights into performance variations and reproducibility. $Co(tpfpp)ClO_4$ functionalized graphene sensors were shown to exhibit a mean correlation coefficient of 0.999 indicating highly consistent sensor responses and excellent reproducibility of the cobalt porphyrin functionalization. A near perfect correlation coefficient indicates that all sensor response profiles are linearly related. This allows variation in sensor performance to be readily normalized in a non-computationally expensive fashion through multiplication of the sensor array responses by a constant matrix.

Variation in sensitivity was found highly correlated to variation in the baseline current of the sensor I_{DS}. This implies variation in sensitivity may be minimized by reducing variation in sensor operating current I_{DS}. This may be achieved by reducing variation in graphene material properties through the development of more uniform graphene growth, transfer, and microfabrication techniques. Variations in sensitivity were also shown to exhibit nearly ideal Gaussian distributions. This represents an important finding because variation in sensitivity encompasses variations in the graphene material, sensor microfabrication process, and functionalization. This has important implications for variation modeling, quality engineering, and the further advancement of this sensing

technology. The combination of these findings mark an important step in the development of new and practical graphene-based chemical sensors for ammonia detection.

Chapter 7: Conclusions

7.1 Thesis Contributions

This thesis builds new graphene chemical and biological sensing technologies from the ground up by developing device-level models, systems, and applications. This work begins by developing a DC current–voltage model for graphene EGFETs by combining models for dielectric-gated graphene FETs with models for the graphene-electrolyte double layer capacitance and graphene quantum capacitance. The developed model is highly accurate and produces as little 2% error in the DC current–voltage characteristic. The model can then be used to compute a number of device characteristics required for circuit design such as transconductance, output impedance, and intrinsic gain.

The model allows for heterogeneous top-gate capacitances, which enable the study of different passivation schemes and cases where the graphene channel is only partially modulated (e.g., partial coverage by an electrogenic cell). The developed model shows partial channel passivation acts to increase the overall series resistance. This was experimentally verified and graphene EGFETs with recessed passivation schemes and minimal leakage current were demonstrated. The model can be fit to *I-V* characteristics to extract device parameters such as minimum carrier concentration, mobility, contact resistance, effective double layer capacitance, and effective charged impurity concentration. This allows graphene EGFET parameters to be estimated with a single measurement as opposed to fabricating specialized devices for a number of different measurements (e.g., Hall, TLM, Mott–Schottky).

The DC model was employed to show that graphene EGFETs should be capable of intrinsic voltage gain for use in amplifier circuits. A basis for determining an optimal channel length given certain design constraints is established. The developed graphene EGFET model may now be employed for application-specific sensor optimization and as a tool to inform the design of large-scale graphene sensors systems.

This thesis also contributes a small-signal frequency-dependent (AC) model for graphene EGFETs. This was accomplished by incorporating the Randles circuit into the small-signal field-effect transistor model. The newly developed model was shown capable of fitting experimental data exceptionally well with model extracted parameters in excellent agreement with parameters that were independently derived from DC characterization. The small-signal model was found to contain a unique pole stemming from the introduction of a resistive element due to electrolyte gating. This causes a unique bottoming out of the magnitude response at high frequency. Graphene EGFETs were implemented in a common-source amplifier configuration and demonstrated capable of providing a gain of 3 V/V and functioning as effective as amplifiers for the first time. This concretely demonstrates the ability of graphene EGFETs to act as amplifiers in chemical and biological applications.

Large-scale sensor arrays and readout systems are developed as a flexible and adaptable framework to further advance the use of graphene-based sensors for chemical and biological applications. This work produces a graphene EGFET array with 256 devices and 100% yield to demonstrate a highly reliable microfabrication process. The array architecture in conjunction with a compact and self-contained measurement system enables characterization of hundreds of graphene EGFETs as a function of V_{DS} and V_{GS}.

These technological advancements represent a milestone in the development of graphene EGFET sensors by enabling the convenient and rapid acquisition of high quality data for a large number of devices. Large sample size statistical data on the electronic performance of graphene EGFETs is provided for the first time. This includes mean and standard deviations for drain-source current, transconductance, output conductance, and intrinsic gain.

This work also contributes a compact piecewise DC model for graphene EGFETs that is shown capable of fitting 87% of *I-V* characteristics with a mean percent error of 7% or less. The compact model enables the extraction of device parameters for a large number of graphene EGFETs for the first time. This also enables the extraction of parameter distributions for mobility, contact resistance, minimum carrier concentration, and Dirac point. This makes it possible to characterize the impact of different fabrication processes on device parameter distributions—an important step in the development of sensor technologies based on graphene EGFETs. The model in conjunction with experimental data is used to produce trends regarding the impacts of design parameters and process-dependent parameters on the intrinsic voltage gain. This work also contributes a framework for the application-specific optimization of large-scale sensor arrays under a number of design constraints and trade-offs.

This thesis then adapts the large-scale sensor system for the development of graphene Ca^{2+} sensors. Graphene EGFETs are functionalized using a polyvinyl chloride (PVC) coating embedded with a neutral calcium ionophore. Sensors possess selectivity, reversibility, fast response time, and exhibit a virtually ideal Nernstian response of 30.1 mV/decade with little variation (σ = 1.9 mV/decade). Sensors are shown capable of

accurately quantify ionized calcium concentration overall several orders of magnitude. This work develops an alternative calibration and measurement method using a least squares distribution matching technique in order to extract relative shifts in *I-V* characteristics and quantify ionized calcium concentrations. The method is faster in that it eliminates the need for full *I-V* characterization of each sensor at each measurement. The method is also beneficial in that it requires only one calibration step. This makes it particularly useful for portable and field-deployable sensor systems where carrying multiple dilutions or in-field dilution preparation is impractical. The ability to monitor a large sample size (N=152) enables the benefits of sensor redundancy to be explored. Sensor redundancy is shown capable of tightening of 95% confidence intervals from ±50% to within ±10% of the ionized calcium concentration. Thus, redundancy is shown to effectively enhance measurement accuracy and noise. These contributions represent milestones in the exploration of selective graphene EGFET chemical sensors. This work can be readily extended to other analytes for the development of multi-analyte graphene EGFET sensor systems.

Finally, the novel sensor system is employed as a convenient vehicle for scaled-up repeatability and the kinetic analysis of a pixelated testbed. Chemiresistive graphene sensors are functionalized for the detection of ammonia using a cobalt porphyrin. This produces a four-fold increase in sensitivity over pristine graphene. Sensors also possess excellent selectivity with responses to ammonia being orders of magnitude greater than the responses to interfering compounds such as water and common organic solvents. Sensor response was found to decay with increasing ammonia concentration, which is

consistent with a reduction in the number of available functionalization binding sites for higher concentration exposures.

A physical model based on absorption kinetics was developed to describe sensor response profiles. The model comprises two adsorption mechanisms—one reversible and one irreversible—and was shown capable of fitting experimental data with a mean percent error of 0.01%. The model is also consistent with the experimental observation of decayed sensor response in response to increasing ammonia concentration.

The ability to monitor hundreds of ammonia sensors provide new insights into performance variations and reproducibility. Cobalt porphyrin functionalized graphene sensors displayed a mean correlation coefficient of 0.999 indicating highly consistent sensor responses and excellent reproducibility of the cobalt porphyrin functionalization. Near perfect correlation coefficient indicates all sensor responses are linearly related. This allows variation in sensor performance to be readily normalized in a non-computationally expensive fashion. Variations in sensitivity were found highly correlated to variations in the baseline current of the sensor I_{DS}. This implies variation in sensitivity may be minimized by reducing variation in sensor operating current I_{DS}. Variations were also shown to exhibit nearly ideal Gaussian distributions, which is an important finding consideration sensitivity variation encompasses variations in the graphene material, sensor microfabrication process, and functionalization.

The sum of these contributions at the device, systems, and application represent milestones in the development of graphene sensors for chemical and biological applications. As such, this thesis is a valuable resource for the continued development of graphene sensors in these domains.

7.2 Future Work

This thesis provides much of the groundwork critical for the continued development of graphene chemical and biological sensors. It is especially important to note the development of the compact sensor system with the ability to simultaneously interrogate hundreds of graphene sensors. This system represents a versatile sensor development platform that is readily adaptable and thus enables accelerated exploration and development of graphene sensors across a wide variety of applications. A number of applications come to mind including leveraging the work on ionized calcium sensing to develop a sensor array for simultaneous multi-analyte detection. This would enable running very common diagnostic tests such as electrolytic blood panels—sensing ionized calcium, sodium, potassium, chloride, and phosphate—on a benchtop system using an inexpensive graphene EGFET-based sensor chip. One can also envision extending the chemistry developed for graphene chemiresistive ammonia sensors to the detection to other hazardous gases, with potential applications event to chemical warfare agents and defense.

There is one application, however, that is particularly fascinating, high impact, and extremely challenging from a technical standpoint for which graphene EGFETs are especially well suited. That is the application graphene EGFETs to electrophysiology for the temporospatial mapping of electrical activity in cell cultures. Recent years have seen a tremendous influx in research efforts in this area with the advent of the Brain Research through Advancing Innovative Neurotechnologies (BRAIN) Initiative [189]. From a scientific standpoint, understanding the workings of the brain represents what is arguably one of the greatest scientific endeavors of humankind. Although considerable progress

has been made toward this end, a comprehensive understanding has yet to be established. One fundamental limitation is our ignorance of the brain's microcircuitry, which largely stems from a lack of tools for mapping neural microcircuitry with adequate spatial and temporal resolution.

The current state-of-the-art in electrophysiology relies very heavily on electrode-based technologies for the interrogation and study of neural circuits [190]–[193]. These technologies possess serious limitations with respect to electrode count and electrode density—often times only providing tens of electrodes at best with very sparse spatial resolution. Cellular microcircuits, however, often consist of thousands, if not millions, of electrically active cells. Attempting to interrogate and study the vast complexity of cellular microcircuitry using such technologies has been likened to attempting to watch an HDTV program while only having access to a few scattered pixels.

Other technologies such as silicon complementary metal-oxide-semiconductor (CMOS) represent a mature and capable technology. Silicon-CMOS, however, is based on an innately opaque substrate material. This poses serious limitations in terms of compatibility with in-line cell imaging equipment and fluorescence microscopy equipment, which are cornerstones in biosciences research.

Graphene EGFETs offer the ability to potentially combine the benefits of MEAs and Si-CMOS while avoiding their pitfalls. Graphene EGFET sensor array provide the transparency of MEAs with the scalability and pixel-level amplification capabilities of Si-CMOS. Graphene EGFET sensor arrays can be manufactured in a completely transparent fashion such that they are visually identical to a simple glass slide. In this way researchers could perform cell culture as they normally would on glass slides or well

plates with added capability for temporospatially mapping electrical communication patterns present within cell cultures. This new technology would provide troves of new information regarding changes in cell health and communication patterns. This could be useful in advancing fundamental science, the study of neurodegenerative diseases, and for more efficient drug development and screening. Adaption of the graphene EGFET sensor system for electrophysiology applications is depicted in **Figure 7.2**. Note that the sensor array can be fabricated in a completely transparent fashion by substituting gold metal lines with a transparent conductive material such as indium tin oxide (ITO).

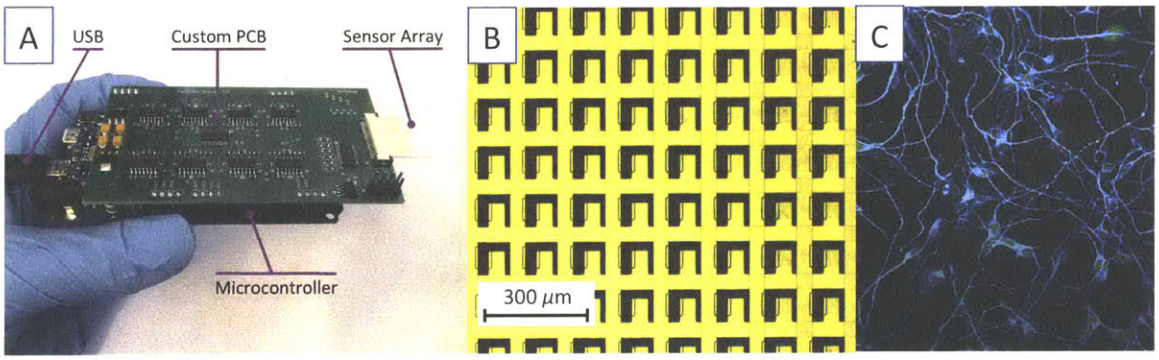

Figure 7.1: A) Complete measurement system and sensor array insert, B) microfabricated graphene EGFET sensor array, C) motor neuron cell culture used for modeling ALS or Lou Gehrig's disease in drug discovery efforts.

In terms of impact, drug development represents a particularly interesting and practical application. The ability to measure the effects of new drugs on cell communication patterns *in vitro* could be used to more effectively screen drug candidates earlier in the development pipeline. This provides a number of potential benefits. It populates later stages in the development pipeline with better candidates [194]. This could enhance Food and Drug Administration (FDA) approval odds, an especially serious concern in the development of central nervous system (CNS) drugs. In doing so, it also

helps to reduce the risk of late-stage drug failures during clinical trials, which can have disastrous implications.

It is important to note that bringing a single drug to market typically requires 12-15 years of research and clinical development efforts, and costs approximately 1-2 billion dollars [195]. In the case of central nervous system (CNS) disorders alone, there exist over 600 conditions and 420 drugs in the U.S. development pipeline. Food and Drug Administration (FDA) approval rates for CNS drugs stand at a meager 6.2%, which is less than half the 13.3% FDA approval rate for non-CNS drugs. Introduction of any innovative technology with the ability to more effectively study and screen drugs earlier in the development pipeline could potentially have a profound impact on the efficacy of bringing a new drug to market.

This thesis has made a number of contributions towards this end by developing accurate DC and AC device models for graphene EGFETs. This enables device performance to be optimized for specific applications such as electrophysiology. The AC modeling work also graphene EGFET pixels cannot only be used to sense small signals but can also function as effectively as amplifiers. In terms of future, work it is important to note that graphene EGFET amplification can be further enhanced by using more advanced circuits configurations such as cascode amplifiers. Cascode amplifiers provide squared intrinsic gain taking previously characterized gains from 3 V/V to 9 V/V, and if optimized perhaps even into the double digits. This provides considerable benefit considering that the current state-of-the-art in electrophysiology is electrode based and provides no pixel-level amplification. This enhanced amplification can also be achieved at little cost in terms of manufacturing complexity and layout area. The second transistor

has no sensing function and only serves to enhance amplification. Because of this, its area can be minimized with respect to the graphene EGFET sensor. **Figure 7.2** depicts graphene EGFETs in a cascode amplifier configuration for enhanced signal amplification.

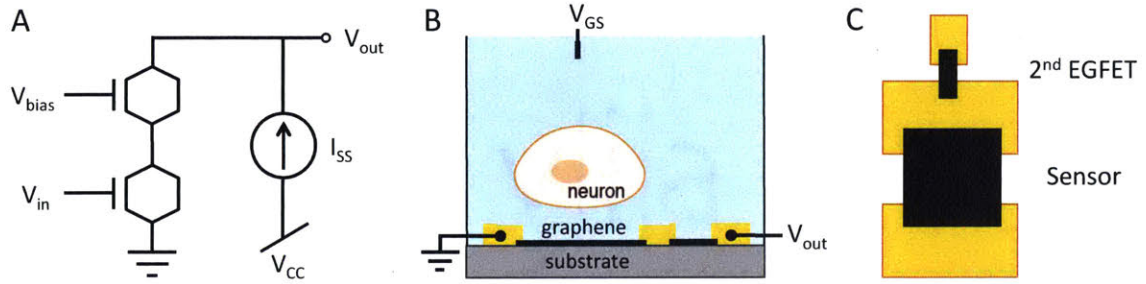

Figure 7.2: A) Graphene EGFET cascode amplifier schematic, B) idealized small-signal amplification capability for action potentials, C) cascode amplifier layout.

At the systems level, this thesis already lays the groundwork for scaling graphene EGFETs sensors into two-dimensional arrays suitable for temporospatial mapping applications. The previously developed array architecture requires only one transistor per pixel and therefore enables maximum pixel density. In the case of the enhanced cascode amplifier configuration, the sensor array requires two transistors per pixel. The second transistor, however, can be incorporated at little cost in terms of manufacturing complexity and area. For these reasons, this thesis has made considerable progress in enabling some very interesting and high impact applications and future research appears especially promising in the area of electrophysiology.

Appendix A1

A1.1 Measurement System Design

The complete measurement system contains a personal computer, microcontroller, custom printed circuit board, and graphene EGFET array chip. The primary functions of the personal computer are record and process the measured data and to program the microcontroller. The microcontroller powers the PCB and supplies the digital control signals necessary to manage row and column selection on the graphene EGFET array. The microcontroller is equipped with two 12-bit digital-to-analog (DAC) outputs that control the applied V_{DS} and V_{GS} biases. The custom PCB applies the V_{DS} and V_{GS} biases to the appropriate graphene EGFET within the array and provides the amplified source-drain current I_{DS} to the 12-bit analog-to-digital converter (ADC) on the microcontroller. The acquired data is then sent back to the personal computer via USB. The developed bench top measurement system is capable of characterizing I_{DS} as a function of V_{DS} and V_{GS} for 256 graphene EGFETs within a matter of minutes.

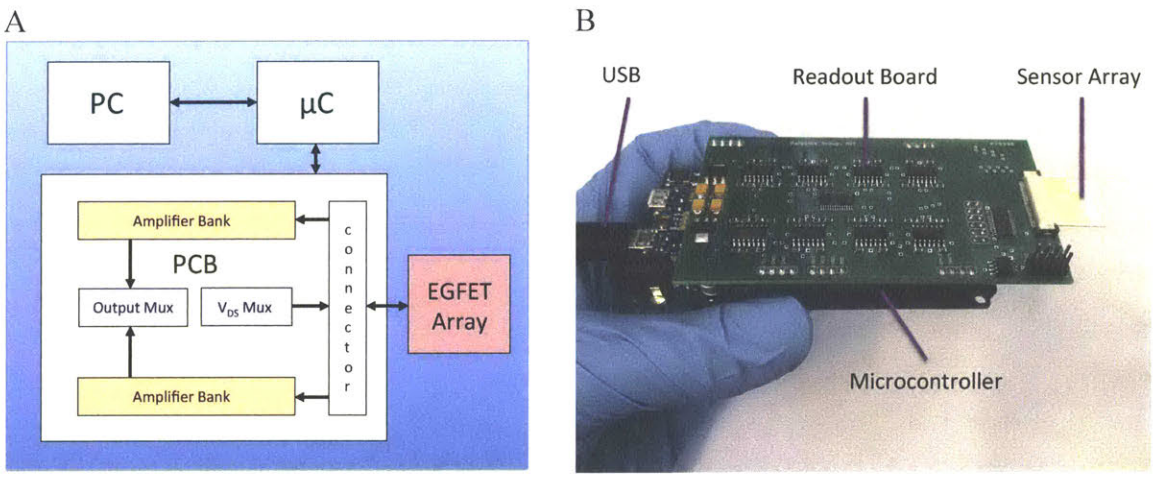

Figure A1.1: A) Overview of the chief components and communication directionality involved in the graphene EGFET array measurement system. B) Image of the actual measurement setup including the microcontroller, custom PCB, and graphene EGFET chip array insert.

The custom PCB performs several functions. It forwards buffered V_{DS} and V_{GS} signals to the graphene EGFET array. The PCB applies the V_{DS} bias to the appropriate row via a 16-channel low impedance analog multiplexer. The series resistance of each analog multiplexer channel is approximately 2.5 Ohms. The PCB then amplifies the resulting graphene EGFET I_{DS} currents across the entire row using a two-stage low-noise transimpedance amplifier. The gains of the first and second stages are -1000 V/I and -10 V/V, respectively. Another 16-channel analog multiplexer is used to perform column selection and forward the amplified I_{DS} signal to a 12-bit analog-to-digital converter (ADC) on the microcontroller. The PCB contains a total of 34 operational amplifiers: 32 to perform I_{DS} amplification and two for buffering V_{DS} and V_{GS} signals. The PCB and amplifier design are illustrated in **Figure A1.2**.

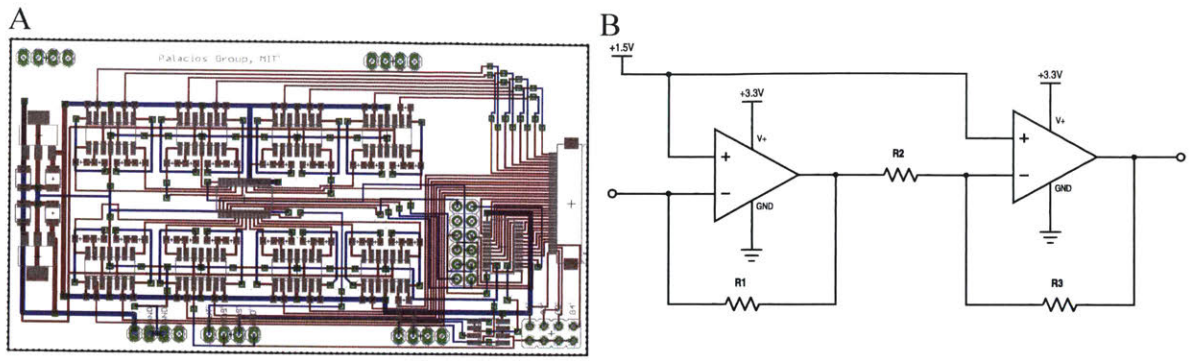

Figure A1.2: A) Custom PCB layout designed for the graphene EGFET measurement system. B) Transimpedance amplifier configuration employed to extract graphene EGFET I_{DS} currents.

The array chip design contains wire sharing to the extent possible while maintaining the ability to access individual devices. This allows access to M x N devices using only M + N wires. The design is based on the fact the currents sum in parallel, and therefore, the output currents from a single column may be tied together into a single output. As long as only one device per column is on at a given time, the entire output current for this column will stem from a single device. It is possible to ensure that only one device per column is on using multiplexing. Individual columns may then be replicated row-wise because the V_{DS} can be shared across columns simply by tying them together in parallel. This wire-sharing scheme along with an optical microscope image of the application to graphene EGFETs is illustrated in **Figure A1.3**.

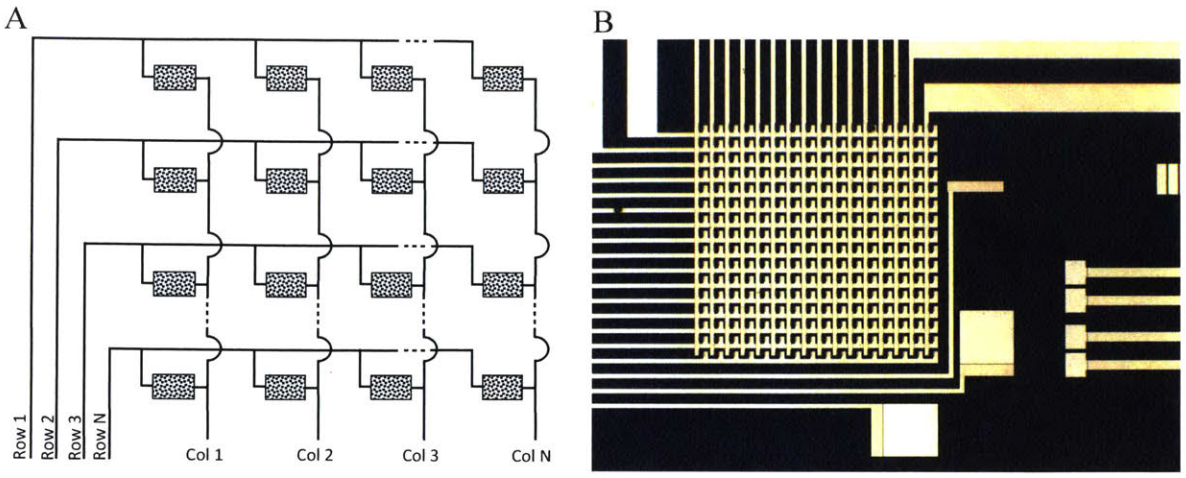

Figure A1.3: A) Array design enabling the measurement of M x N devices using M + N wires. B) Optical microscope image of a 16 x 16 graphene EGFET array implementation.

The measurement system code consists of several pieces. There is microcontroller code for *I-V* characterization and transient response measurement. The *I-V* characterization code and transient response code both begin as shown in **Figure A1.4** and describe the calibration procedure necessary to ensure the 12-bit DACs accurately output the desired V_{DS} and V_{GS} voltages with an accuracy of approximately 1 mV. All code is written for operation on an Arduino DUE and should be used with the Arduino Integrated Development Environment (IDE) version 1.6.5 or later. The Arduino IDE software is available online for free at https://www.arduino.cc/en/Main/Software.

```
// Verified that Gain is ~10,000 V/A
// Verified that current increases roughly linearly with VDS for metal test chip
// Important to disable mux before recording VDS values. ADC produces more accurate
// data when not loaded by the mux and FET array. Important to dummy sample ADCs
// before each FET array sweep. This allows the ADC sampling caps to reach stable
// values before actual ADC data is recorded. Otherwise, the first FET sampled
// (row=0,col=0) will be an outlier

// CALIBRATIION PROCEDURE
// WRITE 0 to DAC output and record voltage with respect to ground as VMIN
// WRITE 4095 to DAC output and record voltage with respect to ground as VMAX
// SLOPE = ( VMAX - VMIN ) / 4095
// Binary value to generate desired voltage with respect to
// VBIN = int { (1/SLOPE)*(desired_voltage+VMID) + VMIN/SLOPE }
// NOW DAC SHOULD OUTPUT PRECISELY THE DESIRED VOLTAGE

// CALIBRATION PROCEDURE (MAKING SURE ADC READS APPLIED DAC VALUES VERY ACCURATELY)
// MEASURE ARDUINO MC POWER SUPPLY VERY ACCURATELY
// ADC VOLTAGE MEASURED = (ARDUINO_SUPPLY_VOLTAGE/4095)*ADC_BITS
// MEASUREMENT SHOULD NOW BE ACCURATE TO WITHIN A 1mV OR SO

// IMPORTANT: WHEN USING GRAPHENE SAMPLES, COMPILE & UPLOAD BEFORE INSERTING GRAPHENE CHIP.
// DURING UPLOADING SPURIOUS VDS SIGNALS ARE GENERATED WHICH MAY DAMAGE/DESTROY GRAPHENE FETS

// IMPORTANT: Peripheral Identifiers on page 38 (PIOC, DACC, etc)
```

Figure A1.4: Microcontroller code comments describing calibration procedure.

In the case of *I-V* characterization, several parameters need to be specified by the user. A list of these parameters are shown in **Figure A1.5** and include voltage sweep ranges and sweep rates. All sweep rates are given in milliseconds. In addition, the user must manually measure and input the value of the mid-rail voltage as the amplifier circuitry operates with respect to the mid-rail and not ground. This is shown in the amplifier configuration illustrated in **Figure A1.2B.** *I-V* characterization code works by setting V_{DS} and V_{GS} and then rapidly scanning through all rows and columns of the sensor array using a nested for loop. The nested for loop controls the row and column selection via two analog multiplexers on the custom PCB. The V_{DS} and V_{GS} values are then changed according to the sweep parameters and the scanning of all rows and columns in the array is then repeated.

```
float VGS_SWEEP_RATE = 500;   // in milliseconds
float VDS_HOLD = 10000;       // in milliseconds
const int numReadings = 100;  // number of readings to average
float VMID = 1.499;           // mid rail supply voltage

float VGS_START = -0.5;       // starting voltage for VGS sweep
float VGS_STOP = 0.5;         // end voltage for VGS sweep
float VGS_INC = 10e-3;        // increment for VGS sweep

float VDS_START = 100e-3;     // starting voltage for VDS sweep
float VDS_STOP = 110e-3;      // end voltage for VDS sweep
float VDS_INC = 10e-3;        // increment for VDS sweep
```

Figure A1.5: Microcontroller input parameters for *I-V* characterization.

The microcontroller code for measuring sensor transient response does not require as many input parameters. In this case, the user only needs to specify constant voltage values for V_{DS}, V_{GS}, and the mid-rail supply voltage. The user is also asked to define the number of readings to take at each pixel, which will be averaged. Lastly, the user is asked to specify the refresh rate for the sensor array. This value, which is given in milliseconds, defines how frequently the array will be scanned. If the user wishes to scan the sensor array as fast as possible, the refresh rate can be set to zero. **Figure A1.6** depicts the header code where the input parameters should be defined.

```
float VDS = 100e-3;         // in volts
float VGS = 0.0;            // in volts
float VMID = 1.499;         // in volts

int numReadings = 100;      // number of averages

float refresh_delay = 100; // in milliseconds
```

Figure A1.6: Microcontroller input parameters for transient response measurement.

The Arduino microcontroller code is designed to transmit the sensor array data via USB to a personal computer for data acquisition and analysis. The custom data acquisition software is written in Python 2.7, a free and open source language available for download at https://www.python.org/downloads/. The Python software is used in conjunction with the Python serial module to manage the serial transmission of sensor

data from the microcontroller to the PC via USB. It is recommended that all Python modules be installed using the pip installer, instructions for which may be found at https://docs.python.org/3/installing/. A number of additional Python modules should be imported in order for the data acquisition code to work properly. These modules along with other input parameters are depicted in **Figure A1.7**.

The user must also accurately specify the USB address on which the serial communication will occur. In this case, the Arduino DUE has two different USB ports: a programming port and a native USB port. The programming port, as the name indicates, can be used for reading from and programming the microcontroller. The native USB port, on the other hand, cannot be used to program the microcontroller but only for data transmission from microcontroller to PC. The native USB port, however, enables faster transmission rates if necessary. It is also important that the user measure and specify the Arduino DUE 3.3V supply rail voltage. The microcontroller analog-to-digital (ADC) conversion occurs with respect to this voltage. Lastly, the user should specify the yield threshold, where the units are given in microamperes. Any device with a source-drain current I_{DS} below this value is treated as a failed device.

```
import sys
import matplotlib
matplotlib.use("TkAgg")
import timeit
import os
import matplotlib.pyplot as plt
import matplotlib.animation as animation
import numpy as np
import serial
import time as timer
import thread

s = serial.Serial(port='/dev/cu.usbmodem1411', baudrate=115200) # Arduino DUE Programming Port
#s = serial.Serial(port='/dev/tty.usbmodem1411', baudrate=115200)   # Arduino DUE Native Port

V_SUPPLY_ARDUINO = 3.2662               # in volts
BITS_TO_V = V_SUPPLY_ARDUINO/4095       # volts/bit
YIELD_THRESHOLD = 10                    # in uA
```

Figure A1.7: List of modules and user defined parameters necessary for the proper function of the Python data acquisition code.

A1.2 Spatial Trends in Variation

Figure A1.2 shows that extracted device parameters from the array show no strong spatial correlations. This indicates successful graphene transfer and a uniformly processed array. Excellent graphene transfer is also supported by the fact that we achieve 100% yield for an array of 256 devices.

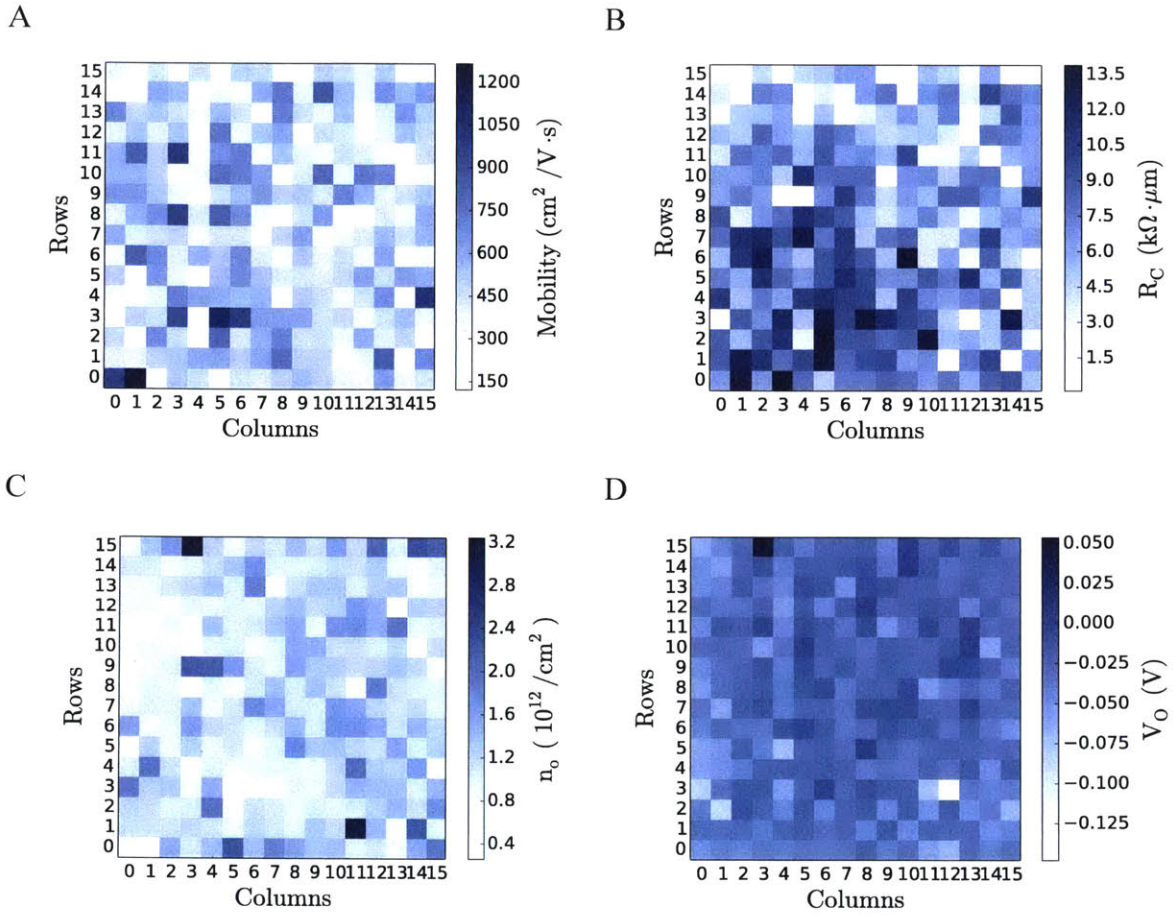

Figure A1.8: Graphene EGFET spatial trends in A) mobility, B) contact resistance, C) minimum carrier concentration, and D) minimum conduction point, Dirac point.

Appendix A2

A2.1 Dirac Point Estimation

Minimum conduction points, or Dirac points, were calculated by fitting the experimental *I-V* characteristic with a polynomial and finding the minimum of the polynomial fit. This ensures the most accurate possible Dirac point interpolation. *I-V* curves were fit using a 6th-order polynomial. Examples in **Figure A2.1** show that 6th-order polynomials fit the experimental data exceptionally well and that the Dirac points interpolated using this method are perfectly reasonable. Experimental data was discretized using 10 mV step size, which could lead to some additional error if the Dirac point was estimated simply by taking the minimum of the discretized dataset.

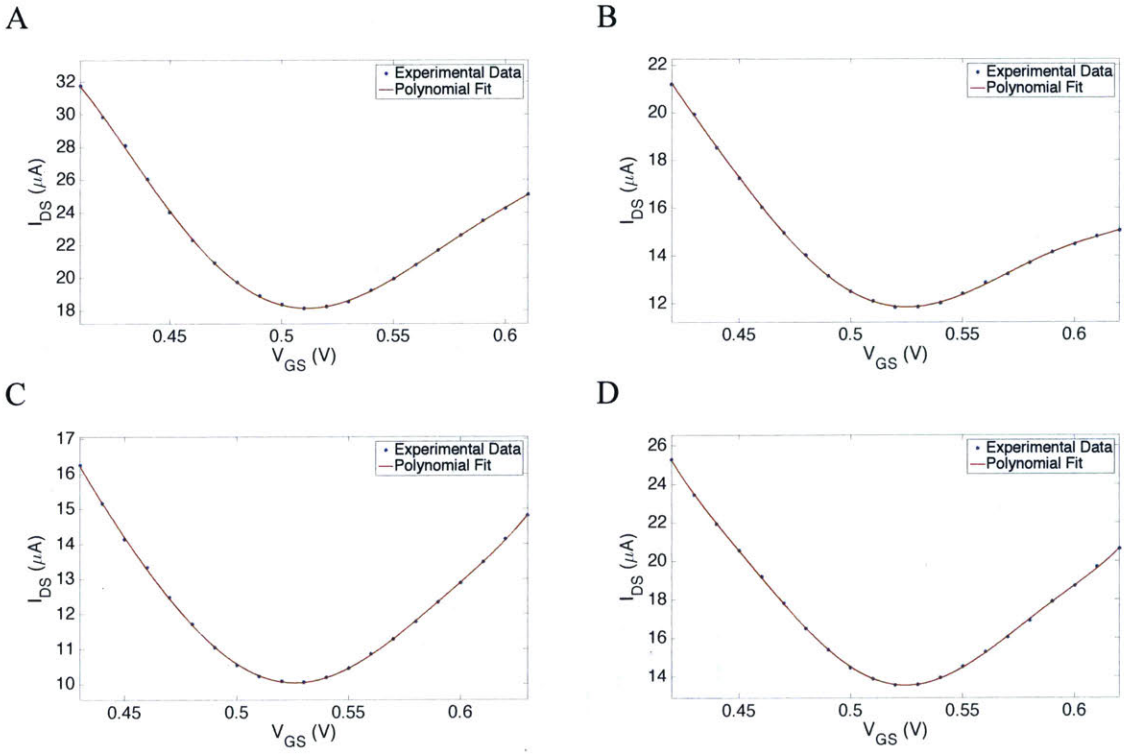

Figure A2.1: Four examples (A-D) showing how the Dirac points were estimated by fitting the discretized experimental *I-V* characteristic with a 6th-order polynomial and finding the minimum of the polynomial fit. This ensures the most accurate possible Dirac point interpolation.

A3.2 Distribution of Dirac Points

Normal quantile plots are given for the minimum conduction points (Dirac points) for each concentration to show that Dirac points are normally distributed.

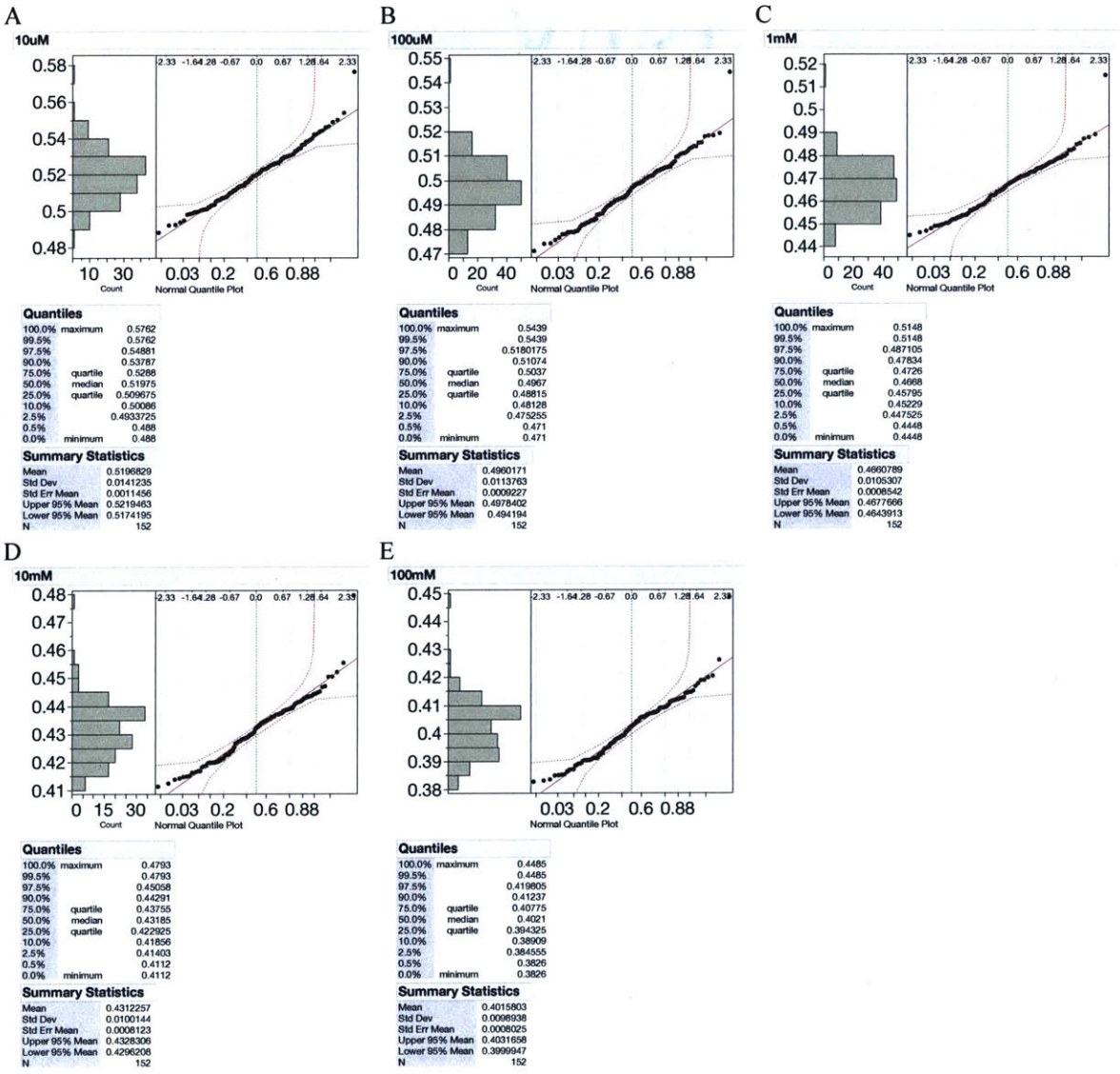

Figure A2.2: Normal quantile plots showing that Dirac points are normally distributed for concentration A) 10 μM, B) 100 μM, C) 1 mM, D) 10 mM, and E) 100 mM. Dirac point decreases linearly with increasing concentration. Standard Deviation in Dirac points decreases slightly with increasing concentration. This is consistent with the fact that *I-V* characteristic slopes are becoming a little steeper with increasing concentration. Sample size is 152 and the bias conditions are V_{DS} = 100 mV, V_{GS} = 0 V.

A2.3 Least Square Error Fit

Profile matching was used to map transient response to a corresponding shift in *I-V* characteristic data. Least squares used to find the optimal shift in *I-V* curve. *I-V* data is discretized in 10 mV increments. To more accurately estimate the optimal shift, the discretized least squares error data was fit near the minimum (± 100mV) using a 4th-order polynomial. The minimum of the continuous polynomial function was then used to estimate the optimal shift in *I-V* curve corresponding to the transient data. The polynomial fitting to the least square error function is depicted in **Figure A2.3**.

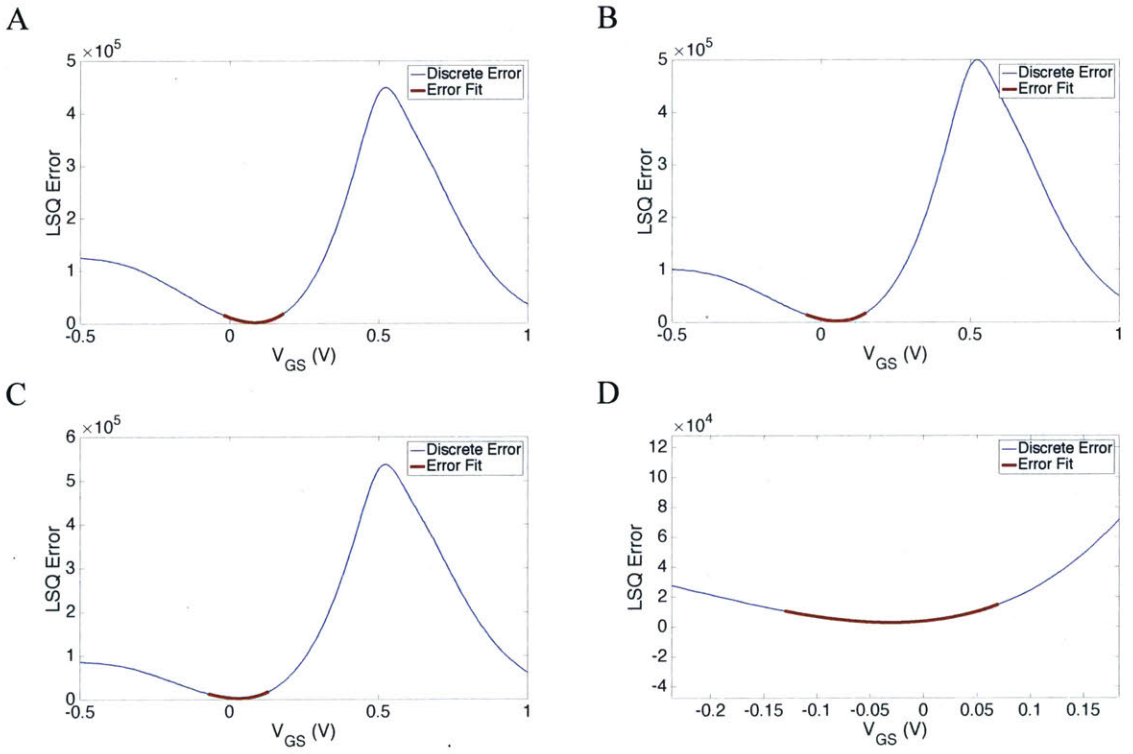

Figure A2.3: Least square error for profile matching at select concentrations A) 10 µM, B) 100 µM, C) 1 mM, and D) a zoomed in view of the 10 µM least squares error function showing excellent fit of the 4th-order polynomial.

A2.4 Synthetic Data Generation

The experimental sample size was 152. In order to simulate the confidence interval decreasing with increasing sample size, we generated 50,000 synthetic transient responses and *I-V* characteristics based on experimentally observed distributions for this data. Empirical cumulative distribution functions (ECDF) were computed for the transient data and *I-V* curve data. 50,000 random numbers were then generated from a uniform probability distribution. The uniformly distributed random numbers were then used with inverse transform sampling to randomly generate transient responses according to the ECDF for the transient response data. These random transient responses could then be mapped to corresponding *I-V* curve data by performing a weighted of *I-V* curve data according to the location of the transient data on the ECDF. The transient data could then be fit to *I-V* curve data using least squares to determine the necessary shift in *I-V* curve and hence concentration. An outline of the process is depicted in **Figure A2.4**. The distribution for current sensitivity is also provided as a reference in **Figure A2.5**.

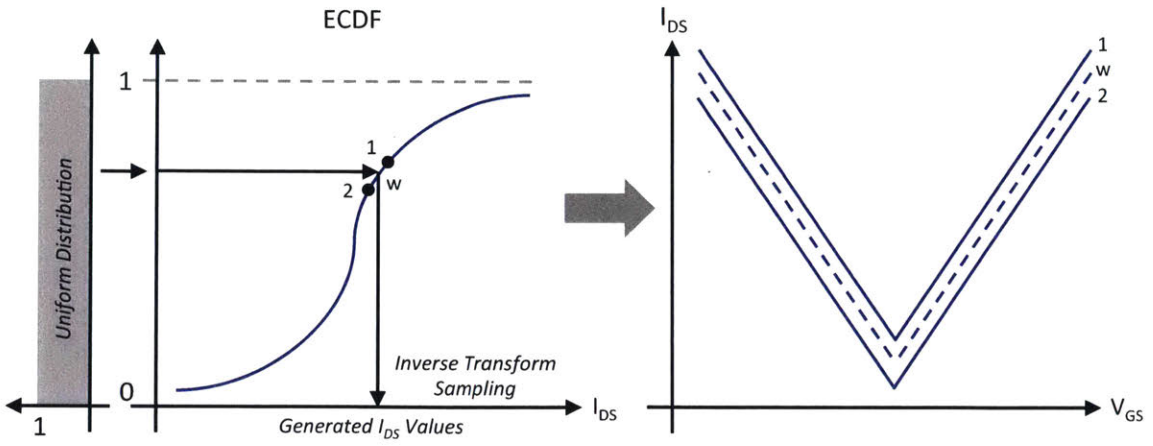

Figure A2.4: Overview of the process for generating synthetic transient data and *I-V* curve data that is distributed according to experimentally observed data.

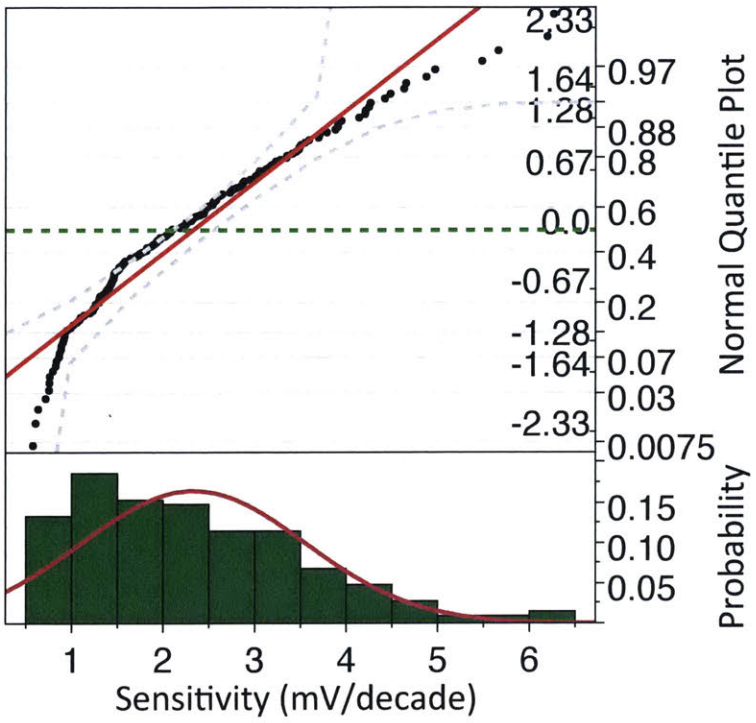

Figure A2.5: Probability distribution of sensor sensitivities in μA/decade. Distribution is a skewed Gaussian because sensitivities cannot be negative. Ideal Gaussian (red) with 95% confidence interval (dashed gray) and 50^{th}-percentile (dashed green).

Appendix A3

A3.1 Derivation of Sensor Response Model

A – analyte

R – reversible binding site

I – irreversible binding site

c_{RA} – concentration of analyte bound to reversible sites

c_R – concentration of free reversible binding sites

c_A – analyte concentration

C_{RT} – total reversible binding sites (free and bound)

α – forward reaction rate for reversible reaction

β – backward reaction rate for reversible reaction

c_{IA} – concentration of analyte bound to irreversible sites

c_I – concentration of free irreversible binding sites

C_{IT} – total irreversible binding sites (free and bound)

γ – forward reaction rate for irreversible reaction

2nd-order reversible reaction:

$$c_R + c_A \underset{\beta}{\overset{\alpha}{\rightleftharpoons}} c_{RA}$$

$$\frac{dc_{RA}(t)}{dt} = \alpha c_R(t) c_A(t) - \beta c_{RA}(t)$$

$$C_{RT} = c_R(t) + c_{RA}(t)$$

$$c_R(t) = C_{RT} - c_{RA}(t)$$

$$c_A(t) = c_A = \text{constant}$$

$$\frac{dc_{RA}(t)}{dt} = \alpha c_A[C_{RT} - c_{RA}(t)] - \beta c_{RA}(t)$$

$$\frac{dc_{RA}(t)}{dt} + (\alpha c_A + \beta)c_{RA}(t) = \alpha c_A C_{RT}$$

Homogeneous solution:

$$c_{RA}^H(t) = e^{-(\alpha c_A + \beta)t}$$

Particular Solution:

$$c_{IA}^P(t) = \frac{\alpha c_A C_{RT}}{\alpha c_A + \beta}$$

Complete Solution:

$$c_{RA}(t) = c_{RA}^H(t) + c_{IA}^P(t) = Ae^{-(\alpha c_A + \beta)t} + \frac{\alpha c_A C_{RT}}{\alpha c_A + \beta}$$

Apply initial conditions:

$$c_{RA}(t = 0) = 0$$

$$c_{RA}(t) = \frac{\alpha c_A C_{RT}}{\alpha c_A + \beta}\left[1 - e^{-(\alpha c_A + \beta)t}\right]$$

2[nd]-order irreversible reaction:

$$c_I + c_A \xrightarrow{\gamma} c_{IA}$$

$$\frac{dc_{IA}(t)}{dt} = \gamma c_I(t) c_A(t)$$

$$C_{IT} = c_I(t) + c_{IA}(t)$$

$$c_I(t) = C_{IT} - c_{IA}(t)$$

$$c_A(t) = c_A = \text{constant}$$

$$\frac{dc_{IA}(t)}{dt} - \gamma c_A[C_{IT} - c_{IA}(t)] = 0$$

$$\frac{dc_{IA}(t)}{dt} + \gamma c_A c_{IA}(t) = \gamma c_A C_{IT}$$

Homogeneous solution:

$$\frac{dc_{IA}(t)}{dt} + \gamma c_A c_{IA}(t) = 0$$

Assume solution of the form:

$$c_{IA}^H(t) = e^{kt}$$

$$ke^{kt} + \gamma c_A e^{kt} = 0$$

$$e^{kt}(k + \gamma c_A) = 0$$

$$k = -\gamma c_A$$

$$c_{IA}^H(t) = e^{-\gamma c_A t}$$

Particular Solution:

Assume solution of the form:

$$c_{IA}^P(t) = K$$

$$\gamma c_A K = \gamma c_A C_{IT}$$

$$K = C_{IT}$$

$$c_{IA}^P(t) = C_{IT}$$

Complete Solution:

$$c_{IA}(t) = c_{IA}^H(t) + c_{IA}^P(t) = Ae^{-\gamma c_A t} + C_{IT}$$

Applying initial condition:

$$c_{IA}(t = 0) = 0$$

$$A = -C_{IT}$$

$$c_{IA}(t) = C_{IT}[1 - e^{-\gamma c_A t}]$$

Combine two adsorption mechanisms: reversible and irreversible

$$\Delta G/G_0 \propto c_X(t) = c_{RA}(t) + c_{IA}(t) = \frac{\alpha c_A C_{RT}}{\alpha c_A + \beta}\left[1 - e^{-(\alpha c_A+\beta)t}\right] + C_{IT}[1 - e^{-\gamma c_A t}]$$

ΔI_{DS} is small in response to changing doping, therefore we can approximate the graphene IV characteristic as linear over this small range. Therefore, doping is proportional to I_{DS}. In other words, the I_{DS} response should be proportional to $c_X(t)$. In our case, we know it is inversely proportional since exponential decay is going downward, not upward. This leads to the following equation.

$$\frac{\Delta G}{G_0} = \widetilde{H_0} - H_R\left[1 - e^{-(\alpha c_A+\beta)t}\right] - H_I[1 - e^{-\gamma c_A t}]$$

$$\frac{\Delta G}{G_0} = H_0 + H_R e^{-(\alpha c_A+\beta)t} + H_I e^{-\gamma c_A t}$$

The complete sensor response curve is described by a piecewise model:

$$\Delta G/G_0 = \begin{cases} H_0 + H_R e^{-(\alpha c_A+\beta)t} + H_I e^{-\gamma c_A t} & t < T_r \\ H_0 + H_R e^{-(\alpha c_A+\beta)T_r} + H_I e^{-\gamma c_A T_r} + H_R e^{-(\alpha c_A+\beta)[t-T_r]} & t > T_r \end{cases}$$

where T_r represents the transition time where the sensors transition from analyte exposure to no analyte exposure.

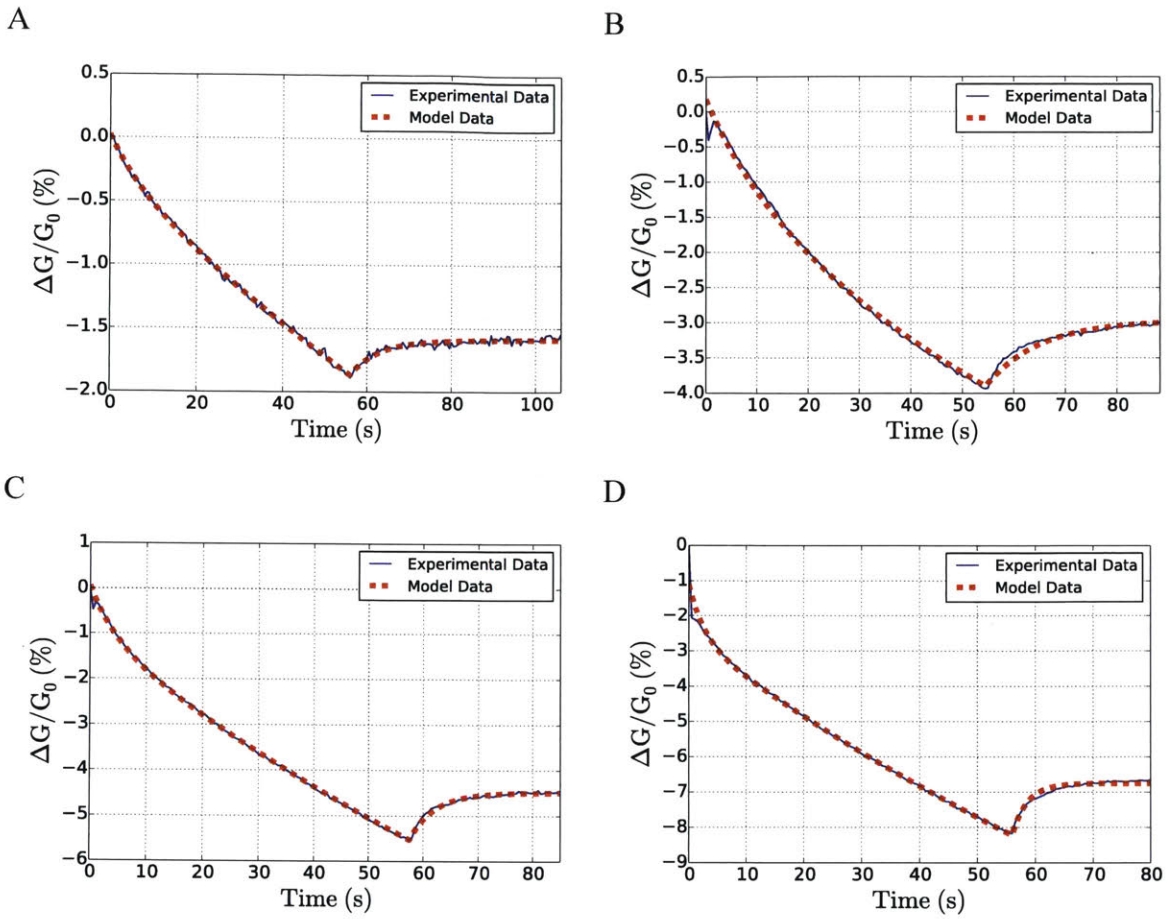

Figure A3.1: Mean sensor response curves and model fits for A) 160 ppm exposure of pristine graphene, B) 40 ppm exposure of functionalized graphene, C) 80 ppm exposure of functionalized graphene, D) 160 ppm exposure of functionalized graphene.

Table A3.1: Model Extracted Parameters

	160 ppm exposure pristine graphene	40 ppm exposure of functionalized graphene	80 ppm exposure of functionalized graphene	160 ppm exposure functionalized graphene
H_0	-5.75	-7.41	-13.23	-19.88
H_R	0.28	0.94	1.04	1.47
H_I	5.49	6.65	12.24	17.30
$\alpha c_A + \beta$	0.1466	0.0947 (underestimated)	0.2211	0.3776 (overestimated)
γc_A	0.0062	0.0118	0.0081	0.0071
Mean Percent Error	0.01193	0.03934	0.01214	0.04815

A3.2 Sensor Response Concentration Dependence

Sensor response decreases with increasing ammonia concentration as shown in **Figure A3.2**.

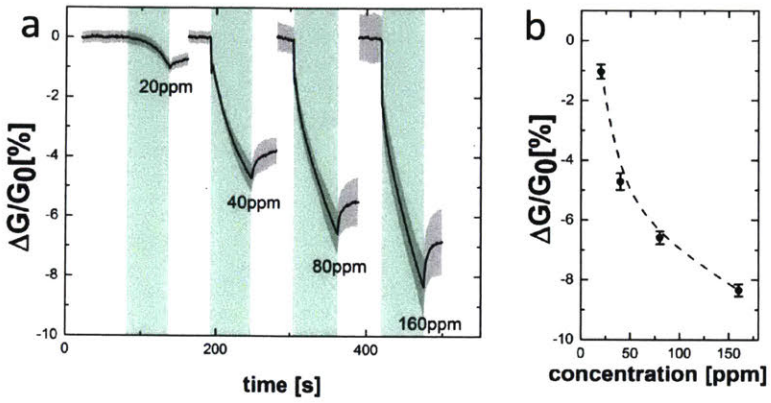

Figure A3.2: A) Mean percent change in conductance of functionalized graphene sensor in response to four different concentrations of NH3. Highlighted regions represent plus or minus one standard deviation from the mean. B) Mean sensor response as a function of NH3 concentration for a fixed exposure time of 60 seconds.

Measurements are always taken after a fixed time, T.

$$\frac{\Delta G}{G_0} = K_0 + K_R e^{-(\alpha c_A + \beta)T} + K_I e^{-\gamma c_A T}$$

$$\frac{\Delta G}{G_0} = K_0 + K_R e^{-\beta T} e^{-\alpha T c_A} + K_I e^{-\gamma T c_A}$$

The amount of response at a given time T should fall off with increasing exposure c_A.

$$\frac{\Delta G}{G_0} \approx K_0 + \widetilde{K}_R e^{-\alpha T c_A} + K_I e^{-\gamma T c_A}$$

Plugging in some extracted values, we know that the change due to the $\widetilde{K}_R e^{-\alpha T c_A}$ term can account for at most about 1.5% and that the change due to $K_I e^{-\gamma T c_A}$ term can be an order of magnitude greater. Therefore, we can roughly neglect the $\widetilde{K}_R e^{-\alpha T c_A}$ term and simply estimate the response using γ. Note that because decay due to the $\widetilde{K}_R e^{-\alpha T c_A}$ term is neglected the extracted γ value is larger than the true value. This model is capable of accurately fitting the experimental results shown in **Figure A3.3.**

$$\frac{\Delta G}{G_0} \approx \widetilde{K}_0 + K_I e^{-\gamma T c_A}$$

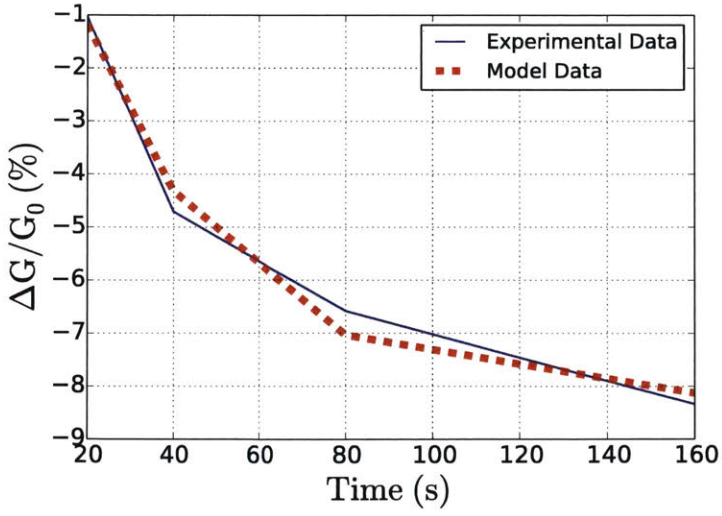

Figure A3.3: Graphene sensor response for 60s NH_3 exposures as a function of increasing NH_3 concentration.

A3.3 Graphene I-V Characteristic Linearity

Figure A3.4 shows that the graphene *I-V* characteristic is linear away from the Dirac point.

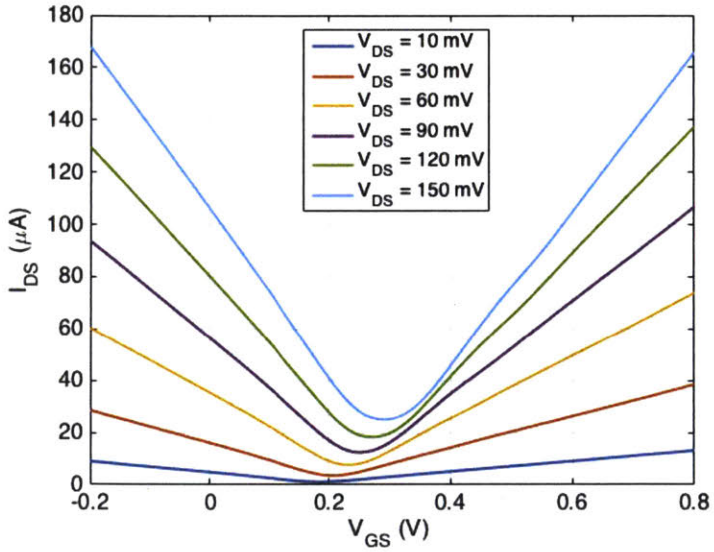

Figure A3.4: Graphene FET I_{DS} vs. V_{GS} for different applied V_{DS} values. Shows graphene *I-V* curve is well approximated as linear.

A3.4 Sensor System Fabrication Details

Graphene chemiresistors consist of a graphene channel between two conductive source-drain contacts – typically metals. A diagram of a graphene sensor along with a microscope image of an actual device are depicted in Figs. 1C and 1D, respectively. Graphene sensor fabrication begins with a piranha cleaned 4" glass wafer. The glass wafer is coated with 25 nm of Al_2O_3 using atomic layer deposition (ALD) to ensure excellent photoresist adhesion in the subsequent metal lift-off process used to form Ti/Au (10 nm / 150 nm) row wires of the sensor array and contact leads. An additional 25 nm

of Al_2O_3 is deposited as interlayer dielectric between row and column wires of the sensor array. BCl_3 plasma using a reactive ion etcher (RIE) is used to etch windows into the interlayer dielectric to allow contact in the appropriate locations between first and second metal layers. The columns of the sensor array are then formed by depositing a second layer of Ti/Au (10 nm / 150 nm) using electron beam evaporation and lift-off photolithography.

A commercial-grade graphene/PMMA film from Graphenea Inc. is transferred over the metal interconnects of a sensor array chip and nitrogen dried to remove any underlying water. The transferred graphene/PMMA film is baked for 15 minutes at 80°C and for two hours at 130°C. This allows for PMMA reflow, which helps to promote adhesion between the graphene and the underlying substrate. The sample is submersed in acetone for several hours to remove the PMMA film from the graphene surface. The sample is then annealed for three hours at 350°C in N_2 to further promote adhesion between the graphene and the substrate. The graphene film is etched in order to define the graphene channel regions using MMA/SPR700 resist stacks and oxygen plasma etching. The sample is immersed once again in acetone for several hours to remove the resist layers. The sample is then coated with approximately 2.4 μm of SU-8 2002 in which windows are photo-defined over the graphene channel regions to allow access of gaseous analytes to the graphene channel region. The sample is baked at 150°C for five minutes to help remove cracks and pinholes in the SU-8 and to enhance the chemical resistance of the SU-8 film.

The graphene sensor array is designed as an insertable chip taking advantage of wire sharing to extent possible while maintaining the ability to access individual devices.

The sensor array architecture allows N^2 sensors to be accessed using a mere 2N wires. The design is shown in Fig. 1E. It is based on the fact the currents sum in parallel, which allows output currents from a single column to be tied together into one output. Row multiplexing is then used to bias one device per column such that the entire output current for a given column stems from a single device. Individual columns are replicated row-wise. Actual fabrication of the arrayed sensor architecture is depicted in Fig. 1F. The appropriate readout circuitry was designed to amplify and convert the current outputs of individual graphene sensors into voltage signals (Fig. 1G) to be read out by an analog-to-digital (ADC) converter for subsequent transmission to a personal computer for data analysis and recording.

A3.5 Sensor Array Functionalization

The graphene sensor array was functionalized with 5,10,15,20-tetrakis(pentafluorophenyl)porphyrinatocobalt(III) perchlorate ($Co(tpfpp)ClO_4$). $Co(tpfpp)ClO_4$ was synthesized according to our previously published procedures[1]. After synthesis, the porphyrin compound was dissolved in dichloromethane (DCM) at a concentration of 0.075 mg/ml. 1 μL of porphyrin solution was dropcast on the sensor array region and allowed to dry in air. The sensor array was used without further washing or processing. Based on the concentration of the solution, the volume of the porphyrin solution, and the area of the sensor array, we estimate the surface coverage.

$$\text{amount of porphyrin on array} = 0.075\ \frac{\text{mg}}{\text{ml}} \times 1\ \mu\text{l}$$

$$= 7.5 \times 10^{-8}\ \text{g}$$

$$= 6.632 \times 10^{-11}\ \text{mol}$$

$$\text{sensor array area} = 140\ \mu\text{m} \times 140\ \mu\text{m} = 1.96\times10^{-8}\ \text{m}^2$$

$$\text{coverage of porphyrin on array} = \frac{6.632\times10^{-11}\ \text{mol}}{1.96\times10^{-8}\ \text{m}^2} = 3.384\times10^{-3}\ \frac{\text{mol}}{\text{m}^2}$$

$$= 2.038\times10^{21}\ \frac{\text{pophryin}}{\text{m}^2}$$

References

[1] A. K. Geim and K. S. Novoselov, "The Rise of Graphene," *Nat. Mater.*, vol. 6, no. 3, pp. 183–91, Mar. 2007.

[2] Y. Zhu, S. Murali, W. Cai, X. Li, J. W. Suk, J. R. Potts, and R. S. Ruoff, "Graphene and Graphene Oxide: Synthesis, Properties, and Applications," *Adv. Mater.*, vol. 22, no. 35, pp. 3906–24, Sep. 2010.

[3] A. H. C. Neto, F. Guinea, N. M. R. Peres, K. S. Novoselov, and A. K. Geim, "The Electronic Properties of Graphene," *Rev. Mod. Phys.*, vol. 81, no. 1, pp. 109–162, Jan. 2009.

[4] K. Tahy, T. Fang, P. Zhao, A. Konar, C. Lian, H. G. Xing, M. Kelly, and D. Jena, "Graphene Transistors," 2008.

[5] C. Soldano, A. Mahmood, and E. Dujardin, "Production, Properties and Potential of Graphene," *Carbon N. Y.*, vol. 48, no. 8, pp. 2127–2150, Jul. 2010.

[6] P. R. Wallace, "The Band Theory of Graphite," *Phys. Rev.*, vol. 71, no. 9, pp. 622–634, 1947.

[7] J. C. Slonczewski and P. R. Weiss, "Band Structure of Graphite," *Phys. Rev.*, vol. 109, no. 2, pp. 272–279, 1958.

[8] K. S. Novoselov, a K. Geim, S. V Morozov, D. Jiang, Y. Zhang, S. V Dubonos, I. V Grigorieva, and a a Firsov, "Electric Field Effect in Atomically Thin Carbon Films," *Science*, vol. 306, no. 5696, pp. 666–9, Oct. 2004.

[9] M. Scarselli, P. Castrucci, and M. De Crescenzi, "Electronic and Optoelectronic Nano-Devices Based on Carbon Nanotubes," *J. Phys. Condens. Matter*, vol. 24, no. 31, p. 313202, Aug. 2012.

[10] E. Gruber, R. A. Wilhelm, R. Pétuya, V. Smejkal, R. Kozubek, A. Hierzenberger, B. C. Bayer, I. Aldazabal, A. K. Kazansky, F. Libisch, A. V. Krasheninnikov, M. Schleberger, S. Facsko, A. G. Borisov, A. Arnau, and F. Aumayr, "Ultrafast electronic response of graphene to a strong and localized electric field," *Nat. Commun.*, vol. 7, pp. 1–7, 2016.

[11] K. Takeuchi, S. Yamamoto, Y. Hamamoto, Y. Shiozawa, K. Tashima, H. Fukidome, T. Koitaya, K. Mukai, S. Yoshimoto, M. Suemitsu, Y. Morikawa, J. Yoshinobu, and I. Matsuda, "Adsorption of CO2 on Graphene: A Combined TPD, XPS, and vdW-DF Study," *J. Phys. Chem. C*, vol. 121, no. 5, pp. 2807–2814, 2017.

[12] M. J. Schulz, V. N. Shanov, and Z. Yin, *Nanotube Superfiber Materials: Changing Engineering Design*. 2014.

[13] K. S. Novoselov, A. K. Geim, S. V Morozov, D. Jiang, M. I. Katsnelson, I. V Grigorieva, and S. V Dubonos, "Two-dimensional gas of massless Dirac fermions in graphene," *Nature*, vol. 438, no. November, pp. 197–200, 2005.

[14] P. Plochocka, C. Faugeras, M. Orlita, M. L. Sadowski, G. Martinez, M. Potemski, M. O. Goerbig, J. N. Fuchs, C. Berger, and W. A. De Heer, "High-energy limit of massless dirac fermions in multilayer graphene using magneto-optical transmission spectroscopy," *Phys. Rev. Lett.*, vol. 100, no. 8, pp. 1–4, 2008.

[15] G. N. Dash, S. R. Pattanaik, and S. Behera, "Graphene for Electron Devices: The Panorama of a Decade," *J. Electron Devices Soc.*, vol. 2, no. 5, pp. 77–104, 2014.

[16] D. S. L. Abergel, V. Apalkov, J. Berashevich, K. Ziegler, and T. Chakraborty, "Properties of Graphene: A Theoretical Perspective," *Adv. Phys.*, vol. 59, no. 4,

pp. 261–482, Jul. 2010.

[17] A. K. Geim, "Graphene: Status and Prospects," *Science (80-.).*, vol. 324, no. June, pp. 1530–1535, 2009.

[18] R. Wang, S. Wang, D. Zhang, Z. Li, Y. Fang, and X. Qiu, "Control of Carrier Type and Density in Exfoliated Graphene by Interface Engineering," *ACS Nano*, vol. 5, no. 1, pp. 408–12, Jan. 2011.

[19] P. Avouris, "Graphene: Electronic and Photonic Properties and Devices," *Nano Lett.*, vol. 10, no. 11, pp. 4285–4294, Sep. 2010.

[20] J. Martin, N. Akerman, G. Ulbricht, T. Lohmann, J. H. Smet, K. von Klitzing, and A. Yacoby, "Observation of Electron–Hole Puddles in Graphene using a Scanning Single-Electron Transistor," *Nat. Phys.*, vol. 4, no. 2, pp. 144–148, Nov. 2007.

[21] H. Hibino, S. Tanabe, S. Mizuno, and H. Kageshima, "Growth and Electronic Transport Properties of Epitaxial Graphene on SiC," *J. Phys. D. Appl. Phys.*, vol. 45, no. 15, p. 154008, Apr. 2012.

[22] S. Adam, E. H. Hwang, V. M. Galitski, and S. Das Sarma, "A Self-Consistent Theory for Graphene Transport," *Proc. Natl. Acad. Sci. U. S. A.*, vol. 104, no. 47, pp. 18392–7, Nov. 2007.

[23] H. Wang, H. Zhao, G. Hu, S. Li, H. Su, and J. Zhang, "Graphene Based Surface Plasmon Polariton Modulator Controlled by Ferroelectric Domains in Lithium Niobate," *Nat. Sci. Reports*, vol. 5, no. December, pp. 1–8, 2015.

[24] Y. Zhang, Y. W. Tan, H. L. Stormer, and P. Kim, "Experimental observation of the quantum Hall effect and Berry's phase in graphene," *Nature*, vol. 438, no. 7065, pp. 201–204, 2005.

[25] S. Ghosh, I. Calizo, D. Teweldebrhan, E. P. Pokatilov, D. L. Nika, A. A. Balandin, W. Bao, F. Miao, and C. N. Lau, "Extremely high thermal conductivity of graphene: Prospects for thermal management applications in nanoelectronic circuits," *Appl. Phys. Lett.*, vol. 92, no. 15, pp. 1–4, 2008.

[26] A. A. Balandin, S. Ghosh, W. Bao, I. Calizo, D. Teweldebrhan, F. Miao, and C. N. Lau, "Superior Thermal Conductivity of Single-Layer Graphene," *Nano Lett.*, vol. 8, no. 3, pp. 902–907, 2008.

[27] W. A. de Heer, C. Berger, M. Ruan, M. Sprinkle, X. Li, Y. Hu, B. Zhang, J. Hankinson, and E. Conrad, "Large area and structured epitaxial graphene produced by confinement controlled sublimation of silicon carbide," *Proc. Natl. Acad. Sci.*, vol. 108, no. 41, pp. 16900–16905, 2011.

[28] V. Borovikov and A. Zangwill, "Step-edge instability during epitaxial growth of graphene from SiC(0001)," *Phys. Rev. B*, vol. 80, no. 12, pp. 1–4, 2009.

[29] S. Hertel, D. Waldmann, J. Jobst, A. Albert, M. Albrecht, S. Reshanov, A. Schöner, M. Krieger, and H. B. Weber, "Tailoring the graphene/silicon carbide interface for monolithic wafer-scale electronics," *Nat. Commun.*, vol. 3, pp. 1–6, 2012.

[30] S. Park and R. S. Ruoff, "Chemical Methods for the Production of Graphenes," *Nat. Nanotechnol.*, vol. 4, no. 4, pp. 217–24, Apr. 2009.

[31] W. Yang, K. R. Ratinac, S. P. Ringer, P. Thordarson, J. J. Gooding, and F. Braet, "Carbon Nanomaterials in Biosensors: Should You Use Nanotubes or Graphene?," *Angew. Chem. Int. Ed. Engl.*, vol. 49, no. 12, pp. 2114–38, Mar. 2010.

[32] M. F. El-kady, V. Strong, S. Dubin, and R. B. Kaner, "Laser Scribing of High-

Performance and Flexible Graphene-Based Electrochemical Capacitors," *Science (80-.).*, vol. 335, no. 6074, pp. 1326–1330, 2012.

[33] S. Wang, P. K. Ang, Z. Wang, A. Ling, L. Tang, J. T. L. Thong, and K. P. Loh, "Solution-Processed Graphene Electronics," *Nano Lett.*, vol. 10, pp. 92–98, 2010.

[34] Y. Huang, X. Dong, Y. Shi, C. M. Li, L.-J. Li, and P. Chen, "Nanoelectronic Biosensors Based on CVD Grown Graphene," *Nanoscale*, vol. 2, no. 8, pp. 1485–8, Aug. 2010.

[35] H. Ago, Y. Ito, N. Mizuta, K. Yoshida, B. Hu, C. M. Orofeo, M. Tsuji, K. Ikeda, and S. Mizuno, "Epitaxial Chemical Vapor Deposition Growth of Single-Layer Graphene over Cobalt Film Crystallized on Sapphire," *ACS Nano*, vol. 4, no. 12, pp. 7407–14, Dec. 2010.

[36] P. W. Sutter, J.-I. Flege, and E. a Sutter, "Epitaxial Graphene on Ruthenium," *Nat. Mater.*, vol. 7, no. 5, pp. 406–11, May 2008.

[37] A. Reina, X. Jia, J. Ho, D. Nezich, H. Son, V. Bulovic, M. S. Dresselhaus, and J. Kong, "Large Area, Few-Layer Graphene Films on Arbitrary Substrates by Chemical Vapor Deposition," *Nano Lett.*, vol. 9, no. 1, pp. 30–35, 2009.

[38] X. Li, W. Cai, J. An, S. Kim, J. Nah, D. Yang, R. Piner, A. Velamakanni, I. Jung, E. Tutuc, S. K. Banerjee, L. Colombo, and R. S. Ruoff, "Large-Area Synthesis of High-Quality and Uniform Graphene Films on Copper Foils," *Science*, vol. 324, no. 5932, pp. 1312–4, Jun. 2009.

[39] S. Bhaviripudi, X. Jia, M. S. Dresselhaus, and J. Kong, "Role of Kinetic Factors in Chemical Vapor Deposition Synthesis of Uniform Large Area Graphene using Copper Catalyst," *Nano Lett.*, vol. 10, no. 10, pp. 4128–33, Oct. 2010.

[40] D. Schall, M. Otto, D. Neumaier, and H. Kurz, "Integrated Ring Oscillators based on high-performance Graphene Inverters," *Nat. Sci. Reports*, vol. 3, pp. 1–5, Jan. 2013.

[41] a. Pirkle, J. Chan, A. Venugopal, D. Hinojos, C. W. Magnuson, S. McDonnell, L. Colombo, E. M. Vogel, R. S. Ruoff, and R. M. Wallace, "The effect of chemical residues on the physical and electrical properties of chemical vapor deposited graphene transferred to SiO2," *Appl. Phys. Lett.*, vol. 99, no. 122108, pp. 1–3, 2011.

[42] J. W. Suk, A. Kitt, C. W. Magnuson, Y. Hao, S. Ahmed, J. An, A. K. Swan, B. B. Goldberg, and R. S. Ruoff, "Transfer of CVD-Grown Monolayer Graphene onto Arbitrary Substrates," *ACS Nano*, vol. 5, no. 9, pp. 6916–24, Sep. 2011.

[43] S. Viswanathan, T. N. Narayanan, K. Aran, K. D. Fink, J. Paredes, P. M. Ajayan, S. Filipek, P. Miszta, H. C. Tekin, F. Inci, U. Demirci, P. Li, K. I. Bolotin, D. Liepmann, and V. Renugopalakrishanan, "Graphene-protein field effect biosensors: Glucose sensing," *Mater. Today*, vol. 18, no. 9, pp. 513–522, 2015.

[44] G. E. Moore, "Cramming more components onto integrated circuits," *Electronics*, vol. 38, no. 8, pp. 1–4, 1965.

[45] J. Hass, R. Feng, T. Li, X. Li, Z. Zong, W. A. De Heer, P. N. First, E. H. Conrad, C. A. Jeffrey, and C. Berger, "Highly ordered graphene for two dimensional electronics," *Appl. Phys. Lett.*, vol. 89, p. 143106, 2006.

[46] G. Nanoelectronics, C. Berger, Z. Song, T. Li, X. Li, A. Y. Ogbazghi, R. Feng, Z. Dai, A. N. Marchenkov, E. H. Conrad, P. N. First, and W. A. De Heer, "Ultrathin Epitaxial Graphite: 2D Electron Gas Properties and a Route toward Graphene-

based Nanoelectronics," *J. Phys. Chem. B*, vol. 108, pp. 19912–19916, 2004.

[47] M. Sprinkle, P. Soukiassian, W. A. De Heer, C. Berger, and E. H. Conrad, "Epitaxial graphene: the material for graphene electronics," *Phys. Status Solidi*, vol. 94, no. 6, pp. 91–94, 2009.

[48] Y. Chen, D. G. . de Oteyza, Z. Pedramrazi, C. Chen, F. R. Fischer, and M. F. Crommie, "Tuning the Band Gap of Graphene Nanoribbons Synthesized from Molecular Precursors," *ACS Nano*, vol. 7, no. 7, pp. 6123–6128, 2013.

[49] B. O. Tayo, "Band gap engineering in finite elongated graphene nanoribbon heterojunctions: Tight-binding model," *AIP Adv.*, vol. 5, no. 8, p. 087121, 2015.

[50] S. Li, Z. Ren, J. Zheng, Y. Zhou, Y. Wan, and L. Hao, "Band gap engineering of graphene/h-BN hybrid superlattices nanoribbons," *J. Appl. Phys.*, vol. 113, p. 033703, 2013.

[51] W. Feng, P. Long, Y. Feng, and Y. Li, "Two-Dimensional Fluorinated Graphene: Synthesis, Structures, Properties and Applications," *Adv. Sci.*, vol. 3, pp. 1–22, 2016.

[52] Y. Zhang, T. Tang, C. Girit, Z. Hao, M. C. Martin, A. Zettl, M. F. Crommie, Y. R. Shen, and F. Wang, "Direct observation of a widely tunable bandgap in bilayer graphene," *Nature*, vol. 459, pp. 820–823, 2009.

[53] K. Kanayama and K. Nagashio, "Gap state analysis in electric-field-induced band gap for bilayer graphene," *Nat. Sci. Reports*, vol. 5, pp. 1–9, 2015.

[54] S. Rumyantsev, G. Liu, M. S. Shur, R. A. Potyrailo, and A. A. Balandin, "Selective Gas Sensing with a Single Pristine Graphene Transistor," *Nano Lett.*, vol. 12, pp. 2294–2298, 2012.

[55] F. Schedin, a K. Geim, S. V Morozov, E. W. Hill, P. Blake, M. I. Katsnelson, and K. S. Novoselov, "Detection of Individual Gas Molecules Adsorbed on Graphene," *Nat. Mater.*, vol. 6, no. 9, pp. 652–5, Sep. 2007.

[56] N. Petrone, C. R. Dean, I. Meric, A. M. van der Zande, P. Y. Huang, L. Wang, D. Muller, K. L. Shepard, and J. Hone, "Chemical Vapor Deposition-Derived Graphene with Electrical Performance of Exfoliated Graphene," *Nano Lett.*, vol. 12, no. 6, pp. 2751–6, Jun. 2012.

[57] L. H. Hess, M. V. Hauf, M. Seifert, F. Speck, T. Seyller, M. Stutzmann, I. D. Sharp, and J. A. Garrido, "High-Transconductance Graphene Solution-Gated Field Effect Transistors," *Appl. Phys. Lett.*, vol. 99, no. 3, p. 033503, 2011.

[58] M. Dankerl, M. V. Hauf, A. Lippert, L. H. Hess, S. Birner, I. D. Sharp, A. Mahmood, P. Mallet, J.-Y. Veuillen, M. Stutzmann, and J. a. Garrido, "Graphene Solution-Gated Field-Effect Transistor Array for Sensing Applications," *Adv. Funct. Mater.*, vol. 20, no. 18, pp. 3117–3124, Sep. 2010.

[59] S.-J. Han, K. a Jenkins, A. Valdes Garcia, A. D. Franklin, A. a Bol, and W. Haensch, "High-Frequency Graphene Voltage Amplifier," *Nano Lett.*, vol. 11, no. 9, pp. 3690–3, Sep. 2011.

[60] D. C. Elias, R. R. Nair, T. M. G. Mohiuddin, S. V Morozov, P. Blake, M. P. Halsall, A. C. Ferrari, D. W. Boukhvalov, M. I. Katsnelson, A. K. Geim, and K. S. Novoselov, "Control of Graphene's Properties by Reversible Hydrogenation: Evidence for Graphane," *Science*, vol. 323, no. 5914, pp. 610–3, Jan. 2009.

[61] Y. Shao, J. Wang, H. Wu, J. Liu, I. A. Aksay, and Y. Lin, "Graphene Based Electrochemical Sensors and Biosensors: A Review," *Electroanalysis*, vol. 22, no.

10, pp. 1027–1036, May 2010.

[62] D. A. C. Brownson, D. K. Kampouris, and C. E. Banks, "Graphene electrochemistry: fundamental concepts through to prominent applications," *Chem. Soc. Rev.*, vol. 41, no. 21, p. 6944, Nov. 2012.

[63] D. Chen, L. Tang, and J. Li, "Graphene-Based Materials in Electrochemistry," *Chem. Soc. Rev.*, vol. 39, no. 8, pp. 3157–80, Aug. 2010.

[64] H. Ji, X. Zhao, Z. Qiao, J. Jung, Y. Zhu, Y. Lu, L. L. Zhang, A. H. MacDonald, and R. S. Ruoff, "Capacitance of Carbon-Based Electrical Double-Layer Capacitors," *Nat. Commun.*, vol. 5, p. 3317, Jan. 2014.

[65] M. D. Stoller, C. W. Magnuson, Y. Zhu, S. Murali, J. W. Suk, R. Piner, and R. S. Ruoff, "Interfacial Capacitance of Single Layer Graphene," *Energy Environ. Sci.*, vol. 4, no. 11, p. 4685, 2011.

[66] M. Zhou, Y. Zhai, and S. Dong, "Electrochemical Sensing and Biosensing Platform Based on Chemically Reduced Graphene Oxide," *Anal. Chem.*, vol. 81, no. 14, pp. 5603–13, Jul. 2009.

[67] C. Lee, X. Wei, J. W. Kysar, and J. Hone, "Measurement of the Elastic Properties and Intrinsic Strength of Monolayer Graphene," *Science (80-.).*, vol. 321, no. July, pp. 385–388, 2008.

[68] B. M. Giacchetti, A. Hsu, H. Wang, V. Vinciguerra, and F. Pappalardo, "Graphene Chemical Sensors on Flexible Substrates," pp. 1–18.

[69] Y. H. Kwak, D. S. Choi, Y. N. Kim, H. Kim, D. H. Yoon, S.-S. Ahn, J.-W. Yang, W. S. Yang, and S. Seo, "Flexible Glucose Sensor using CVD-Grown Graphene-Based Field Effect Transistor," *Biosens. Bioelectron.*, vol. 37, no. 1, pp. 82–7,

2012.

[70] H. J. Yoon, Y. Zhang, S. S. Kim, M. M.-C. Cheng, and Z. Zhou, "A flexible biocompatible graphene sensor for real-time monitoring of PH and protein," *2011 6th IEEE Int. Conf. Nano/Micro Eng. Mol. Syst.*, pp. 1104–1107, Feb. 2011.

[71] K. S. Kim, Y. Zhao, H. Jang, S. Y. Lee, J. M. Kim, K. S. Kim, J.-H. Ahn, P. Kim, J.-Y. Choi, and B. H. Hong, "Large-Scale Pattern Growth of Graphene Films for Stretchable Transparent Electrodes," *Nature*, vol. 457, no. 7230, pp. 706–10, Feb. 2009.

[72] S. Bae, H. Kim, Y. Lee, X. Xu, J.-S. Park, Y. Zheng, J. Balakrishnan, T. Lei, H. R. Kim, Y. Il Song, Y.-J. Kim, K. S. Kim, B. Ozyilmaz, J.-H. Ahn, B. H. Hong, and S. Iijima, "Roll-to-roll production of 30-inch graphene films for transparent electrodes.," *Nat. Nanotechnol.*, vol. 5, no. 8, pp. 574–8, Aug. 2010.

[73] X. Wang, L. Zhi, and K. Müllen, "Transparent, conductive graphene electrodes for dye-sensitized solar cells," *Nano Lett.*, vol. 8, no. 13, pp. 323–327, Mar. 2008.

[74] A. Reina, H. Son, L. Jiao, B. Fan, M. S. Dresselhaus, Z. Liu, and J. Kong, "Transferring and Identification of Single- and Few-Layer Graphene on Arbitrary Substrates," *J. Phys. Chem. C*, vol. 112, no. 46, pp. 17741–17744, 2008.

[75] G. L. C. Paulus, K. Y. Lee, N. F. Reuel, Q. H. Wang, and R. Brittany, "A Graphene-Based Physiometer Array for the Analysis of Single Biological Cells," in *American Institute of Chemical Engineers*, 2013.

[76] Y. Wang, Y. Li, L. Tang, J. Lu, and J. Li, "Application of Graphene-Modified Electrode for Selective Detection of Dopamine," *Electrochem. commun.*, vol. 11, no. 4, pp. 889–892, Apr. 2009.

[77] S. Hou, M. L. Kasner, S. Su, K. Patel, and R. Cuellari, "Highly Sensitive and Selective Dopamine Biosensor Fabricated with Silanized Graphene," *J. Phys. Chem. C*, vol. 114, no. 35, pp. 14915–14921, Sep. 2010.

[78] T. Qian, C. Yu, X. Zhou, S. Wu, and J. Shen, "Au Nanoparticles Decorated Polypyrrole/Reduced Graphene Oxide Hybrid Sheets for Ultrasensitive Dopamine Detection," *Sensors Actuators B Chem.*, vol. 193, pp. 759–763, Mar. 2014.

[79] L. Tan, K.-G. Zhou, Y.-H. Zhang, H.-X. Wang, X.-D. Wang, Y.-F. Guo, and H.-L. Zhang, "Nanomolar Detection of Dopamine in the Presence of Ascorbic Acid at β-Cyclodextrin/Graphene Nanocomposite Platform," *Electrochem. commun.*, vol. 12, no. 4, pp. 557–560, Apr. 2010.

[80] L. Wu, L. Feng, J. Ren, and X. Qu, "Electrochemical Detection of Dopamine using Porphyrin-Functionalized Graphene," *Biosens. Bioelectron.*, vol. 34, no. 1, pp. 57–62, Apr. 2012.

[81] M. Mallesha, R. Manjunatha, C. Nethravathi, G. S. Suresh, M. Rajamathi, J. S. Melo, and T. V. Venkatesha, "Functionalized-graphene modified graphite electrode for the selective determination of dopamine in presence of uric acid and ascorbic acid," *Bioelectrochemistry*, vol. 81, no. 2, pp. 104–8, Jun. 2011.

[82] Y. Mao, Y. Bao, S. Gan, F. Li, and L. Niu, "Electrochemical Sensor for Dopamine Based on a Novel Graphene-Molecular Imprinted Polymers Composite Recognition Element," *Biosens. Bioelectron.*, vol. 28, no. 1, pp. 291–7, Oct. 2011.

[83] A. Martín, J. Hernández-Ferrer, L. Vázquez, M.-T. Martínez, and A. Escarpa, "Controlled Chemistry of Tailored Graphene Nanoribbons for Electrochemistry: A Rational Approach to Optimizing Molecule Detection," *RSC Adv.*, vol. 4, no. 1, p.

132, 2014.

[84] F. Li, J. Chai, H. Yang, D. Han, and L. Niu, "Synthesis of Pt/Ionic Liquid/Graphene Nanocomposite and its Simultaneous Determination of Ascorbic Acid and Dopamine," *Talanta*, vol. 81, no. 3, pp. 1063–8, May 2010.

[85] C.-L. Sun, H.-H. Lee, J.-M. Yang, and C.-C. Wu, "The Simultaneous Electrochemical Detection of Ascorbic Acid, Dopamine, and Uric Acid using Graphene/Size-Selected Pt Nanocomposites," *Biosens. Bioelectron.*, vol. 26, no. 8, pp. 3450–5, Apr. 2011.

[86] J. Du, R. Yue, F. Ren, Z. Yao, F. Jiang, P. Yang, and Y. Du, "Novel Graphene Flowers Modified Carbon Fibers for Simultaneous Determination of Ascorbic Acid, Dopamine and Uric Acid," *Biosens. Bioelectron.*, vol. 53, pp. 220–4, Mar. 2014.

[87] J.-U. Park, S. Nam, M.-S. Lee, and C. M. Lieber, "Synthesis of Monolithic Graphene-Graphite Integrated Electronics," *Nat. Mater.*, vol. 11, no. 2, pp. 120–5, Feb. 2012.

[88] M. Zhang, C. Liao, Y. Yao, Z. Liu, F. Gong, and F. Yan, "High-Performance Dopamine Sensors Based on Whole-Graphene Solution-Gated Transistors," *Adv. Funct. Mater.*, vol. 24, no. 7, pp. 978–985, Feb. 2014.

[89] G. Zhou, J. Chang, S. Cui, H. Pu, Z. Wen, and J. Chen, "Real-Time, Selective Detection of Pb2+ in Water Using a Reduced Graphene Oxide/Gold Nanoparticle Field-Effect Transistor Device," *ACS Appl. Mater. Interfaces*, vol. 6, pp. 19235–19241, 2014.

[90] D.-J. Kim, I. Y. Sohn, J.-H. Jung, O. J. Yoon, N.-E. Lee, and J.-S. Park, "Reduced

graphene oxide field-effect transistor for label-free femtomolar protein detection," *Biosens. Bioelectron.*, vol. 41, pp. 621–6, Mar. 2013.

[91] H. Helmholtz, "Studien uber electrische grenzschichten," *Ann. Der Phys. und Chemie*, vol. 243, pp. 337–382, 1879.

[92] G. Guoy, "Constitution of the electric charge at the surace of an electrolyte," *J. Phys. Theor. Appl.*, vol. 9, pp. 457–468, 1910.

[93] D. L. Chapman, "A contribution to the theory of electrocapillarity," *Dublin Philos. Mag. J. Sci.*, vol. 6, pp. 475–481, 1913.

[94] J. Masliyah and S. Bhattacharjee, *Electrokinetic and Colloid Transport Phenomena*. 2006.

[95] O. Stern, "The theory of the electrolytic double layer," *Elektrochem. Angew. Phys. Chem.*, vol. 30, pp. 508–516, 1924.

[96] H. Wang and L. Pilon, "Accurate Simulations of Electric Double Layer Capacitance of Ultramicroelectrodes," *J. Phys. Chem. C*, vol. 115, no. 33, pp. 16711–16719, Aug. 2011.

[97] M. Kilic, M. Bazant, and A. Ajdari, "Steric Effects in the Dynamics of Electrolytes at Large Applied Voltages. I. Double-layer Charging," *Phys. Rev. E*, vol. 75, no. 2, p. 021502, Feb. 2007.

[98] R. L. Mccreery, "Advanced Carbon Electrode Materials for Molecular Electrochemistry," *Chem. Rev.*, vol. 108, pp. 2646–2687, 2008.

[99] J. R. Miller, R. a. Outlaw, and B. C. Holloway, "Graphene Electric Double Layer Capacitor with Ultra-High-Power Performance," *Electrochim. Acta*, vol. 56, pp. 10443–10449, Dec. 2011.

[100] M. D. Stoller, S. Park, Y. Zhu, J. An, and R. S. Ruoff, "Graphene-Based Ultracapacitors," *Nano Lett.*, vol. 8, no. 10, pp. 3498–502, Oct. 2008.

[101] M. H. Ervin, B. S. Miller, B. Hanrahan, B. Mailly, and T. Palacios, "A comparison of single-wall carbon nanotube electrochemical capacitor electrode fabrication methods," *Electrochim. Acta*, vol. 65, pp. 37–43, Mar. 2012.

[102] I. Meric, M. Y. Han, A. F. Young, B. Ozyilmaz, P. Kim, and K. L. Shepard, "Current Saturation in Zero-Bandgap, Top-Gated Graphene Field-Effect Transistors," *Nat. Nanotechnol.*, vol. 3, no. 11, pp. 654–9, Nov. 2008.

[103] I. J. Umoh, S. Member, T. J. Kazmierski, S. Member, and B. M. Al-hashimi, "A Dual-Gate Graphene FET Model for Circuit Simulation — SPICE Implementation," *IEEE Tranactions Nanotechnol.*, vol. 12, no. 3, pp. 427–435, 2013.

[104] M. Magallo, C. Maneux, H. Happy, T. Zimmer, and S. Member, "Scalable Electrical Compact Modeling for Graphene FET Transistors," *IEEE Tranactions Nanotechnol.*, vol. 12, no. 4, pp. 539–546, 2013.

[105] V. Ryzhii, M. Ryzhii, A. Satou, T. Otsuji, and N. Kirova, "Device Model for Graphene Bilayer Field-Effect Transistor," *J. Appl. Phys.*, vol. 105, no. 10, p. 104510, 2009.

[106] H. Wang, S. Member, A. Hsu, J. Kong, D. A. Antoniadis, and T. Palacios, "Compact Virtual-Source Current–Voltage Model for Top- and Back-Gated Graphene Field-Effect Transistors," *IEEE Trans. Electron Devices*, vol. 58, no. 5, pp. 1523–1533, 2011.

[107] D. Jiménez, "Explicit Drain Current, Charge and Capacitance Model of Graphene

Field-Effect Transistors," *IEEE Trans. Electron Devices*, vol. 58, no. 12, pp. 4377–4383, 2011.

[108] J. Ristein, W. Zhang, F. Speck, M. Ostler, L. Ley, and T. Seyller, "Characteristics of Solution Gated Field Effect Transistors on the Basis of Epitaxial Graphene on Silicon Carbide," *J. Phys. D. Appl. Phys.*, vol. 43, no. 34, p. 345303, Sep. 2010.

[109] J. Xia, F. Chen, J. Li, and N. Tao, "Measurement of the Quantum Capacitance of Graphene," *Nat. Nanotechnol.*, vol. 4, no. 8, pp. 505–9, Aug. 2009.

[110] C. Mackin, L. H. Hess, A. Hsu, Y. Song, J. Kong, J. A. Garrido, and T. Palacios, "A Current–Voltage Model for Graphene Electrolyte-Gated Field-Effect Transistors," *IEEE Trans. Electron Devices*, vol. 61, no. 12, pp. 3971–3977, 2014.

[111] N. Schwierz, D. Horinek, and R. R. Netz, "Reversed Anionic Hofmeister Series: The Interplay of Surface Charge and Surface Polarity," *Langmuir ACS J. surfaces colloids*, vol. 26, no. 10, pp. 7370–9, May 2010.

[112] S. Birner, "Modeling of Semiconductor Nanostructures and Semiconductor – Electrolyte Interfaces," Technical University Munich, 2011.

[113] W. Cheney and D. Kincaid, *Numerical Mathematics and Computing (6th Edition)*. 2008.

[114] U. Asher and C. Greif, *First Course in Numerical Methods*. 2011.

[115] R. Hamming, *Numerical Methods for Scientists and Engineers (2nd Edition)*. 2013.

[116] S. Pal and S. Bhunia, *Engineering Mathematics*. 2015.

[117] S. P. Venkateshan and S. Prasanna, *Computational Methods in Engineering*. 2014.

[118] R. Burden and J. D. Faires, *Numerical Analysis (9th Edition)*. 2011.

[119] B. Mailly-Giacchetti, A. Hsu, H. Wang, V. Vinciguerra, F. Pappalardo, L. Occhipinti, E. Guidetti, S. Coffa, J. Kong, and T. Palacios, "pH Sensing Properties of Graphene Solution-Gated Field-Effect Transistors," *J. Appl. Phys.*, vol. 114, no. 8, p. 084505, 2013.

[120] L. H. Hess, M. Seifert, and J. a. Garrido, "Graphene Transistors for Bioelectronics," *Proc. IEEE*, vol. 101, no. 7, pp. 1780–1792, 2013.

[121] L. H. Hess, M. Jansen, V. Maybeck, M. V Hauf, M. Seifert, M. Stutzmann, I. D. Sharp, A. Offenhäusser, and J. a Garrido, "Graphene Transistor Arrays for Recording Action Potentials from Electrogenic Cells," *Adv. Mater.*, vol. 23, no. 43, pp. 5045–9, Nov. 2011.

[122] D. Kuzum, H. Takano, E. Shim, J. C. Reed, H. Juul, A. G. Richardson, J. de Vries, H. Bink, M. a. Dichter, T. H. Lucas, D. a. Coulter, E. Cubukcu, and B. Litt, "Transparent and flexible low noise graphene electrodes for simultaneous electrophysiology and neuroimaging," *Nat. Commun.*, vol. 5, no. May, p. 5259, 2014.

[123] D. Park, A. A. Schendel, S. Mikael, S. K. Brodnick, T. J. Richner, J. P. Ness, M. R. Hayat, F. Atry, S. T. Frye, R. Pashaie, S. Thongpang, Z. Ma, and J. C. Williams, "Graphene-based carbon-layered electrode array technology for neural imaging and optogenetic applications," *Nat. Commun.*, vol. 5, no. October, pp. 1–11, 2014.

[124] C. Distante, M. Leo, P. Siciliano, and K. C. Persaud, "On the study of feature extraction methods for an electronic nose," *Sensors Actuators, B Chem.*, vol. 87, no. 2, pp. 274–288, 2002.

[125] H. Smyth and D. Cozzolino, "Instrumental methods (Spectroscopy, Electronic Nose, and Tongue) as tools to predict taste and aroma in beverages: Advantages and limitations," *Chem. Rev.*, vol. 113, no. 3, pp. 1429–1440, 2013.

[126] A. Manickam, C. A. Johnson, S. Kavusi, and A. Hassibi, "Interface design for CMOS-integrated Electrochemical Impedance Spectroscopy (EIS) biosensors," *Sensors*, vol. 12, no. 11, pp. 14467–14488, 2012.

[127] C. E. Shannon, "Communication in the Presence of Noise," in *Proceedings of the IRE*, 1949, vol. 37, no. 1, pp. 10–21.

[128] D. R. Franceschetti and J. R. Macdonald, "Small-Signal AC Response Theory for Electrochromic Thin Films," *J. Electrochem. Soc.*, vol. 129, no. 8, pp. 1754–1756, 1982.

[129] R. P. Janek, W. R. Fawcett, and A. Ulman, "Impedance Spectroscopy of Self-Assembled Monolayers on Au(111): Sodium Ferrocyanide Charge Transfer at Modified Electrodes," *Langmuir*, vol. 14, no. 11, pp. 3011–3018, 1998.

[130] C. Mackin and T. Palacios, "Large-scale sensor systems based on graphene electrolyte-gated field-effect transistors," *Analyst*, vol. 141, no. 9, pp. 2704–2711, 2016.

[131] K. W. Clark, X. G. Zhang, I. V. Vlassiouk, G. He, R. M. Feenstra, and A. P. Li, "Spatially Resolved Mapping of Electrical Conductivity across Individual Domain (Grain) Boundaries in Graphene," *ACS Nano*, vol. 7, no. 9, pp. 7956–7966, 2013.

[132] C. Neumann, S. Reichardt, P. Venezuela, M. Drögeler, L. Banszerus, M. Schmitz, K. Watanabe, T. Taniguchi, F. Mauri, B. Beschoten, S. V. Rotkin, and C. Stampfer, "Raman spectroscopy as probe of nanometre-scale strain variations in

graphene," *Nat. Commun.*, vol. 6, no. May, p. 8429, 2015.

[133] J. D. Buron, F. Pizzocchero, P. U. Jepsen, D. H. Petersen, J. M. Caridad, B. S. Jessen, T. J. Booth, and P. Bøggild, "Graphene mobility mapping," *Sci. Rep.*, vol. 5, p. 12305, 2015.

[134] E. Uesugi, H. Goto, R. Eguchi, A. Fujiwara, and Y. Kubozono, "Electric double-layer capacitance between an ionic liquid and few-layer graphene.," *Sci. Rep.*, vol. 3, p. 1595, Jan. 2013.

[135] P. Bergveld, "Thirty years of ISFETOLOGY: What happened in the past 30 years and what may happen in the next 30 year," *Sensors Actuators B Chem.*, vol. 88, no. 1, pp. 1–20, 2003.

[136] M. Pumera, A. Ambrosi, A. Bonanni, E. L. K. Chng, and H. L. Poh, "Graphene for Electrochemical Sensing and Biosensing," *Trends Anal. Chem.*, vol. 29, no. 9, pp. 954–965, Oct. 2010.

[137] Y. Song, X. Li, C. Mackin, X. Zhang, W. Fang, T. Palacios, H. Zhu, and J. Kong, "Role of Interfacial Oxide in High-Efficiency Graphene–Silicon Schottky Barrier Solar Cells," *Nano Lett.*, vol. 15, no. 3, pp. 2104–2110, 2015.

[138] S.-W. Hwang, H. Tao, D.-H. Kim, H. Cheng, J.-K. Song, E. Rill, M. a Brenckle, B. Panilaitis, S. M. Won, Y.-S. Kim, Y. M. Song, K. J. Yu, A. Ameen, R. Li, Y. Su, M. Yang, D. L. Kaplan, M. R. Zakin, M. J. Slepian, Y. Huang, F. G. Omenetto, and J. a Rogers, "A Physically Transient Form of Silicon Electronics," *Science*, vol. 337, no. 6102, pp. 1640–4, Sep. 2012.

[139] J. M. Rothberg, W. Hinz, T. M. Rearick, J. Schultz, W. Mileski, M. Davey, J. H. Leamon, K. Johnson, M. J. Milgrew, M. Edwards, J. Hoon, J. F. Simons, D.

Marran, J. W. Myers, J. F. Davidson, A. Branting, J. R. Nobile, B. P. Puc, D. Light, T. a Clark, M. Huber, J. T. Branciforte, I. B. Stoner, S. E. Cawley, M. Lyons, Y. Fu, N. Homer, M. Sedova, X. Miao, B. Reed, J. Sabina, E. Feierstein, M. Schorn, M. Alanjary, E. Dimalanta, D. Dressman, R. Kasinskas, T. Sokolsky, J. a Fidanza, E. Namsaraev, K. J. McKernan, A. Williams, G. T. Roth, and J. Bustillo, "An Integrated Semiconductor Device Enabling Non-Optical Genome Sequencing," *Nature*, vol. 475, no. 7356, pp. 348–52, Jul. 2011.

[140] P. Buehlmann and L. D. Chen, *Ion-Selective Electrodes With Ionophore-Doped Sensing Membranes*, no. March. 2011.

[141] C.-H. Yeh, Y.-W. Lain, Y.-C. Chiu, C.-H. Liao, D. Ricardo Moyano, S. S. H. Hsu, and P.-W. Chiu, "Gigahertz Flexible Graphene Transistors for Microwave Integrated Circuits," *ACS Nano*, vol. 8, no. 8, pp. 7663–7670, 2014.

[142] W. Gao, S. Emaminejad, H. Yin, Y. Nyein, S. Challa, K. Chen, A. Peck, H. M. Fahad, H. Ota, H. Shiraki, D. Kiriya, D. Lien, G. A. Brooks, R. W. Davis, and A. Javey, "Fully integrated wearable sensor arrays for multiplexed in situ perspiration analysis," *Nature*, vol. 529, no. 7587, pp. 509–514, 2016.

[143] V. Georgakilas, M. Otyepka, A. B. Bourlinos, V. Chandra, N. Kim, K. C. Kemp, P. Hobza, R. Zboril, and K. S. Kim, "Functionalization of Graphene: Covalent and Non-Covalent Approaches, Derivatives and Applications," *Chem. Rev.*, vol. 112, no. 11, pp. 6156–214, Nov. 2012.

[144] Y. Dan, Y. Lu, N. J. Kybert, Z. Luo, and a T. C. Johnson, "Intrinsic Response of Graphene Vapor Sensors," *Nano Lett.*, vol. 9, no. 4, pp. 1472–5, Apr. 2009.

[145] E. Bakker, "Determination of Unbiased Selectivity Coefficients of Neutral Carrier-

Based Cation-Selective Electrodes," *Anal. Chem.*, vol. 69, no. 6, pp. 1061–1069, 1997.

[146] I. Bedlechowicz-Śliwakowska, P. Lingenfelter, T. Sokalski, A. Lewenstam, and M. Maj-Zurawska, "Ion-selective electrode for measuring low Ca2+ concentrations in the presence of high K+, Na+ and Mg2+ background," *Anal. Bioanal. Chem.*, vol. 385, no. 8, pp. 1477–1482, 2006.

[147] D. W. Barry, K. C. Hansen, R. E. Van Pelt, M. Witten, P. Wolfe, MS, and W. M. Kohrt, "Acute Calcium Ingestion Attenuates Exercise-induced Disruption of Calcium Homeostasis," *Med. Sci. Sport. Exerc.*, vol. 43, no. 4, pp. 617–623, 2011.

[148] I. R. Gunn and J. R. Wallace, "Urine calcium and serum ionized calcium, total calcium and parathyroid hormone concentrations in the diagnosis of primary hyperparathyroidism and familial benign hypercalcaemia," *Ann. Clin. Biochem.*, vol. 29, pp. 52–58, 1992.

[149] E. Bakker, P. Buehlmann, and E. Pretsch, "Carrier-Based Ion-Selective Electrodes and Bulk Optodes. 1. General Characteristics," *Chem. Rev.*, vol. 97, no. 8, pp. 3083–3132, 1997.

[150] S. Jamasb, S. D. Collins, and R. L. Smith, "A Physically-based Model for Drift in Al203-gate pH ISFETs," *International Conference on Solid-State Sensors and Actuators*, 1997. .

[151] S. Shah and J. B. Christen, "Pulse Width Modulation Circuit for ISFET Drift Reset," in *Sensors*, 2013, pp. 1–4.

[152] S. Jamasb, S. Collins, and R. L. Smith, "A physical model for drift in pH ISFETs," *Sensors Actuators B. Chem.*, vol. 49, pp. 146–155, 1998.

[153] C. Toumazou, L. M. Shepherd, S. C. Reed, G. I. Chen, A. Patel, D. M. Garner, C. A. Wang, C. Ou, K. Amin-desai, P. Athanasiou, H. Bai, I. M. Q. Brizido, B. Caldwell, D. Coomber-alford, P. Georgiou, K. S. Jordan, J. C. Joyce, M. La Mura, D. Morley, S. Sathyavruthan, S. Temelso, R. E. Thomas, and L. Zhang, "Simultaneous DNA Amplification and Detection using a pH-sensing Semiconductor System," *Nat. Methods*, vol. 10, no. 7, pp. 641–646, 2013.

[154] Y. Ohno, K. Maehashi, Y. Yamashiro, and K. Matsumoto, "Electrolyte-Gated Graphene Field-Effect Transistors for Detecting pH and Protein Adsorption," *Nano Lett.*, vol. 9, no. 9, pp. 3318–3322, 2009.

[155] Z. Cheng, Q. Li, Z. Li, Q. Zhou, and Y. Fang, "Suspended Graphene Sensors with Improved Signal and Reduced Noise," *Nano Lett.*, vol. 10, no. 5, pp. 1864–8, May 2010.

[156] K. Maehashi, Y. Sofue, S. Okamoto, Y. Ohno, and K. Inoue, "Selective ion sensors based on ionophore-modified graphene field-effect transistors," in *The 14th International Meeting on Chemical Sensors*, 2012, pp. 305–308.

[157] M. Gautam and A. H. Jayatissa, "Gas sensing properties of graphene synthesized by chemical vapor deposition," *Mater. Sci. Eng. C*, vol. 31, no. 7, pp. 1405–1411, Oct. 2011.

[158] A. G. Bannov, J. Prášek, O. Jašek, and L. Zajíčková, "Investigation of pristine graphite oxide as room-temperature chemiresistive ammonia gas sensing material," *Sensors (Switzerland)*, vol. 17, no. 2, 2017.

[159] U. Stöberl, U. Wurstbauer, W. Wegscheider, D. Weiss, and J. Eroms, "Morphology and Flexibility of Graphene and Few-Layer Graphene on Various

Substrates," *Appl. Phys. Lett.*, vol. 93, no. 5, p. 051906, 2008.

[160] Y. Xu, Y. Wang, J. Liang, Y. Huang, Y. Ma, X. Wan, and Y. Chen, "A Hybrid Material of Graphene and Poly (3,4-ethyldioxythiophene) with High Conductivity, Flexibility, and Transparency," *Nano Res.*, vol. 2, no. 4, pp. 343–348, Apr. 2009.

[161] G. Wang, Y. Ji, X. Huang, X. Yang, P. I. Gouma, and M. Dudley, "Fabrication and characterization of polycrystalline WO3nanofibers and their application for ammonia sensing," *J. Phys. Chem. B*, vol. 110, no. 47, pp. 23777–23782, 2006.

[162] B. T. Marquis and J. F. Vetelino, "A semiconducting metal oxide sensor array for the detection of NOx and NH3," *Sensors Actuators, B Chem.*, vol. 77, no. 1–2, pp. 100–110, 2001.

[163] A. A. Tomchenko, G. P. Harmer, B. T. Marquis, and J. W. Allen, "Semiconducting metal oxide sensor array for the selective detection of combustion gases," *Sensors Actuators, B Chem.*, vol. 93, no. 1–3, pp. 126–134, 2003.

[164] L. K. Fiddes, J. Chang, and N. Yan, "Electrochemical detection of biogenic amines during food spoilage using an integrated sensing RFID tag," *Sensors Actuators, B Chem.*, vol. 202, pp. 1298–1304, 2014.

[165] N. R. Tanguy, M. Thompson, and N. Yan, "A review on advances in application of polyaniline for ammonia detection," *Sensors Actuators, B Chem.*, vol. 257, pp. 1044–1064, 2018.

[166] M. Hirata and L. Sun, "Characteristics of an organic semiconductor polyaniline film as a sensor for NH3 gas," *Sensors Actuators A. Phys.*, vol. 40, no. 2, pp. 159–163, 1994.

[167] A. L. Kukla, Y. M. Shirshov, and S. A. Piletsky, "Ammonia sensors based on sensitive polyaniline films," *Sensors Actuators, B Chem.*, vol. 37, no. 3, pp. 135–140, 1996.

[168] S. Radhakrishnan and S. D. Deshpande, "Conducting Polymers Functionalized with Phthalocyanine as Nitrogen Dioxide Sensors," *Sensors*, vol. 2, pp. 185–194, 2002.

[169] Z. Wu, X. Chen, S. Zhu, Z. Zhou, Y. Yao, W. Quan, and B. Liu, "Enhanced sensitivity of ammonia sensor using graphene/polyaniline nanocomposite," *Sensors Actuators B Chem.*, vol. 178, pp. 485–493, Mar. 2013.

[170] S. M. Mortazavi Zanjani, M. M. Sadeghi, M. Holt, S. F. Chowdhury, L. Tao, and D. Akinwande, "Enhanced sensitivity of graphene ammonia gas sensors using molecular doping," *Appl. Phys. Lett.*, vol. 108, no. 3, p. 033106, Jan. 2016.

[171] D. Zhang, J. Liu, C. Jiang, A. Liu, and B. Xia, "Quantitative detection of formaldehyde and ammonia gas via metal oxide-modified graphene-based sensor array combining with neural network model," *Sensors Actuators, B Chem.*, vol. 240, pp. 55–65, 2017.

[172] R. Ghosh, A. Midya, S. Santra, S. K. Ray, and P. K. Guha, "Chemically Reduced Graphene Oxide for Ammonia Detection at Room Temperature," *ACS Appl. Mater. Interfaces*, vol. 5, no. 15, pp. 7599–7603, Aug. 2013.

[173] M. Seredych, A. V. Tamashausky, and T. J. Bandosz, "Graphite Oxides Obtained from Porous Graphite: The Role of Surface Chemistry and Texture in Ammonia Retention at Ambient Conditions," *Adv. Funct. Mater.*, vol. 20, no. 10, pp. 1670–1679, May 2010.

[174] M. Seredych and T. J. Bandosz, "Combined role of water and surface chemistry in reactive adsorption of ammonia on graphite oxides," *Langmuir*, vol. 26, no. 8, pp. 5491–5498, 2010.

[175] Y. Wang, L. Zhang, N. Hu, Y. Wang, Y. Zhang, Z. Zhou, Y. Liu, and S. Shen, "Ammonia gas sensors based on chemically reduced graphene oxide sheets self-assembled on Au electrodes," *Nanoscale Res. Lett. 2014*, vol. 9, no. 251, pp. 1–12, 2014.

[176] X. Li, X. Chen, Y. Yao, N. Li, and X. Chen, "High-stability quartz crystal microbalance ammonia sensor utilizing graphene oxide isolation layer," *Sensors Actuators, B Chem.*, vol. 196, pp. 183–188, 2014.

[177] R. S. Andre, F. M. Shimizu, C. M. Miyazaki, A. Riul, D. Manzani, S. J. L. Ribeiro, O. N. Oliveira, L. H. C. Mattoso, and D. S. Correa, "Hybrid layer-by-layer (LbL) films of polyaniline, graphene oxide and zinc oxide to detect ammonia," *Sensors Actuators, B Chem.*, vol. 238, pp. 795–801, 2017.

[178] N. A. Travlou, K. Singh, E. Rodríguez-Castellón, and T. J. Bandosz, "Cu–BTC MOF–graphene-based hybrid materials as low concentration ammonia sensors," *J. Mater. Chem. A*, vol. 3, no. 21, pp. 11417–11429, 2015.

[179] M. V. Katkov, V. I. Sysoev, A. V. Gusel'nikov, I. P. Asanov, L. G. Bulusheva, and A. V. Okotrub, "A backside fluorine-functionalized graphene layer for ammonia detection," *Phys. Chem. Chem. Phys.*, vol. 17, no. 1, pp. 444–450, 2015.

[180] S. F. Liu, A. R. Petty, G. T. Sazama, and T. M. Swager, "Single-Walled Carbon Nanotube / Metalloporphyrin Composites for the Chemiresistive Detection of Amines and Meat Spoilage," *Angew. Chem. Int. Ed. Engl.*, vol. 54, no. 22, pp.

6554–6557, 2015.

[181] I. Iezhokin, D. Den Boer, P. Offermans, M. Ridene, J. A. A. W. Elemans, G. P. Adriaans, and C. F. J. Flipse, "Porphyrin molecules boost the sensitivity of epitaxial graphene for NH3 detection," *J. Phys. Condens. Matter*, vol. 29, no. 6, p. 065001, 2017.

[182] C. Di Natale, K. Buchholt, E. Martinelli, R. Paolesse, G. Pomarico, A. D. Amico, I. Lundström, and A. L. Lloyd, "Chemical Investigation of quartz microbalance and ChemFET transduction of molecular recognition events in a metalloporphyrin film," *Sensors Actuators B Chem.*, vol. 135, no. 2, pp. 560–567, 2009.

[183] Z. Cao, Q. Chen, Y. Lu, H. Liu, and Y. Hu, "Density Functional Theory Study on the InteractionBetween Metalloporphyrins and NH3," *Int. J. Quantum Chem.*, vol. 113, no. 8, pp. 1137–1146, 2013.

[184] A. Chaudhary, R. Patra, and S. P. Rath, "Binding of Catechols to Iron (III)–Octaethylporphyrin : An Experimental and DFT Investigation," *Eur. J. Inorg. Chem.*, vol. 2010, no. 33, pp. 5211–5221, 2010.

[185] W. Auwärter, D. Écija, F. Klappenberger, and J. V Barth, "Porphyrins at interfaces," *Nat. Chem.*, vol. 7, no. 2, pp. 105–120, 2015.

[186] M. Gautam and A. H. Jayatissa, "Adsorption kinetics of ammonia sensing by graphene films decorated with platinum nanoparticles," *J. Appl. Phys.*, vol. 111, no. 9, p. 094317, 2012.

[187] N. Lei, P. Li, W. Xue, and J. Xu, "Simple Graphene Chemiresistors as pH Sensors: Fabrication and Characterization," *Meas. Sci. Technol.*, vol. 22, no. 10, p. 107002, Oct. 2011.

[188] P. K. Ang, W. Chen, A. T. S. Wee, and K. P. Loh, "Solution-Gated Epitaxial Graphene as pH Sensor," *J. Am. Chem. Soc.*, vol. 130, no. 44, pp. 14392–3, Nov. 2008.

[189] A. P. Alivisatos, M. Chun, G. M. Church, R. J. Greenspan, M. L. Roukes, and R. Yuste, "The Brain Activity Map Project and the Challenge of Functional Connectomics," *Neuron*, vol. 74, no. 6, pp. 970–974, 2012.

[190] M. E. Spira and A. Hai, "Multi-electrode array technologies for neuroscience and cardiology," *Nat. Nanotechnol.*, vol. 8, no. 2, pp. 83–94, 2013.

[191] G. W. Grose, E. Rieske, G. W. Kreutzberg, and A. Meyer, "A new fixed-array multi-electrode system designed for long-term monitoring of extracellular single unit neuronal activity in vitro," *Neurosci. Lett.*, vol. 6, no. 2–3, pp. 101–105, 1977.

[192] M. P. Maher, J. Pine, J. Wright, and Y. Tai, "The neurochip: a new multielectrode device for stimulating and recording from cultured neurons," *J. Neurosci. Methods*, vol. 87, no. 1, pp. 45–56, 1999.

[193] G. W. Gross, W. Y. Wen, and J. W. Lln, "Transparent indium-tin oxide electrode patterns for extracellular, multisite recording in neuronal cultures," *J. Neurosci. Methods*, vol. 15, no. 3, pp. 243–252, 1985.

[194] J. H. Doroshow, "Re-Engineering Early Phase Cancer Drug Development: Decreasing the Time from Novel Target to Novel Therapeutic," in *16th Annual Drug Discovery Symposium*, 2016, pp. 1–44.

[195] J. Loo, *Industry Surveys: Pharmaceuticals*. McGraw Hill Financial, 2016.